MULTI-SCALE COMPUTATIONAL TECHNIQUES FOR DESIGN OF POLYCRYSTALLINE MATERIALS

A Dissertation

Presented to the Faculty of the Graduate School

of Cornell University

in Partial Fulfillment of the Requirements for the Degree of

Doctor of Philosophy

by

Veeraraghavan Sundararaghavan

August 2007

MULTI-SCALE COMPUTATIONAL TECHNIQUES FOR DESIGN OF POLYCRYSTALLINE MATERIALS

Veeraraghavan Sundararaghavan, Ph.D.

Cornell University 2007

Microstructures play an important role in controlling distribution of properties in engineering materials. It is possible to develop components with tailored distribution of properties such as strength and stiffness by controlling microstructure evolution during the manufacturing process. When forming metallic components by imposing large deformations, mechanisms such as slip and lattice rotation drive formation of texture in the underlying polycrystalline microstructure. Such microstructural changes affect the final distribution of material properties in the component. By carefully designing the imposed deformation, one could potentially tailor the microstructure and obtain desired property distributions. This thesis focuses on development of novel computational strategies for designing deformation processes to realize materials with desired properties. The techniques presented are an interplay of several new tools developed recently, such as reduced order modeling, graphical cross-plots, statistical learning, microstructure homogenization and multi-scale sensitivity analysis. The primary outcomes of this thesis are listed below:

- Development of reduced-order representations and graphical methodologies for representing process-property-texture relationships.
- Development of adaptive reduced-order optimization techniques for identification of processing paths that lead to desirable microstructure-sensitive properties.

- Development of homogenization techniques for predicting microstructure evolution in large deformation processes.
- Development of multi-scale sensitivity analysis of poly-crystalline material deformation for optimizing microstructure-sensitive properties during industrial forming processes.

The framework for design of polycrystalline microstructures leads to increased product yield in industrial forming processes and simultaneously allows control distribution of properties such as stiffness and strength in forged products. Multi-scale design problems leading to billions of unknowns have been solved using parallel computing techniques. The computational framework can be readily used for selecting optimal processing paths for achieving desired properties. The methodology developed is a fundamental effort at providing detailed deformation process design solutions needed for controlling properties of performance-critical hardware components in automotive, structural and aerospace applications.

BIOGRAPHICAL SKETCH

The author was born in Chennai, formerly Madras, India in September 1981. After completing his high school education from Dayanand Anglo Vedic (D.A.V.) Senior Secondary School in Chennai, the author was admitted into the Dual degree program in Mechanical Engineering at the Indian Institute of Technology Madras in 1998, from where he received his degrees of Bachelor of Technology and Master of Technology in 2003. In August 2003, the author entered the doctoral program at the Sibley School of Mechanical and Aerospace Engineering, Cornell University and was awarded a Masters degree in May 2006. After completing PhD, the author will be joining the faculty of Department of Aerospace engineering at University of Michigan, Ann Arbor.

This thesis is dedicated to my parents P. Sundararaghavan and S. Radha for their constant support and encouragement towards academic pursuits during my school and college years.

ACKNOWLEDGEMENTS

I would like to thank my advisor, Professor Nicholas Zabaras, for his constant support, motivation and guidance over the last four years. I would also like to thank Professors Subrata Mukherjee, Shefford Baker and Thorsten Joachims for serving on my special committee and for their encouragement during the course of this work.

The financial support for this project was provided by Mechanical Behavior of Materials program of the Army Research Office (ARO) (grant W911NF-04-1-0283) and the Computational Mathematics Program of the Air Force Office of Scientific Research (grant DE-FC07-ID0214396). I would like to thank the Sibley School of Mechanical and Aerospace Engineering for having supported me through a teaching assistantship for part of my study at Cornell. I would like to acknowledge the support from Cornell Theory center and MPDC cluster computing system that helped in significantly accelerating my computational work.

Most of the computer codes associated with this project including the optimization simulator were written using the object oriented programming environment of `Diffpack` and the academic license that allowed for these developments is appreciated. The parallel simulators were developed based on a combination of locally developed parallel solvers and an open source scientific computation package `PETSc`. I would like to acknowledge the effort of its developers. I also acknowledge the support I received from current and past MPDC members with whom I closely worked during the course of this project.

TABLE OF CONTENTS

LIST OF TABLES

LIST OF FIGURES

Chapter 1

Introduction

Realization of optimal material properties is important for hardware components in aerospace, naval and automotive applications where there is a continuous need to reduce material utilization for reduced process cost, fuel consumption and higher mobility. Critical components involve performance indices [1] that are related to the microstructures obtained during processing. Computational materials-by-design approaches aim to integrate processing, structure and properties through multi-scale material models [2]. In the area of composites, such techniques have enabled design of structures with interesting extremal properties such as negative thermal expansion [3] and negative Poisson's ratio [4]. In contrast to composites, techniques that allow tailoring of properties of polycrystalline metals involve tailoring of preferred orientation of crystals manifested as the crystallographic texture. The thermo-mechanical description of metallic materials, as considered in this thesis, is based on two different length-scales. The macro-scale is associated with the component being modeled (10^{-3} to 10^{1} m) and the meso-scale is characterized by the underlying polycrystalline microstructure (10^{-6} to 10^{-3} m). During forming processes, mechanisms such as crystallographic slip and lattice rotation drive formation of texture and variability in property distributions in such materials. A useful method for designing materials is through control of deformation processes leading to the formation of textures that yield desired property distributions. Several applications exist where certain textures are desirable to improve properties. Materials with tailored properties are useful in a spectrum of applications including high-performance engines, protective structures and structural materials. For example, a Goss texture is desirable in transformer cores to reduce power losses

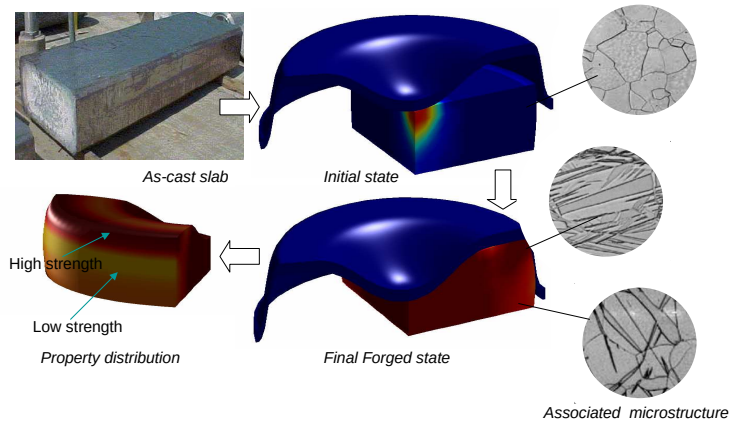

Figure 1.1: The overall aim of this work is to optimize the microstructure and hence, properties, during deformation processing of polycrystalline materials. Optimization of properties would allow for engines, armor and structural components with improved performance.

during magnetization [5]. In deformation processes such as deep drawing, a high value of texture-dependent R parameter [6] and low planar anisotropy is necessary to prevent earing and to increase drawability of the sheet. This thesis addresses property and yield optimization problems in deformation processes (see Fig. 1.1) using a rigorous computational framework.

Deformation processing of metals is associated with two major requirements: (1) the production of usable shapes while maximizing yield; and (2) the optimization of mechanical properties through microstructure control. Available models [7, 8, 9, 10, 11, 12, 13, 14, 15, 16] that only satisfy the first requirement do not incorporate microstructure-induced anisotropy and hence, are incomplete. Models for optimization of properties rely on costly metallurgical experiments for generating correlations between processes and properties and associated processing maps [17, 18, 19]. Because of the large variety of microstructures (and associated properties) possible, construction of property-microstructure correlations purely

through experiments is an intractable task. Polycrystalline microstructures differ in several characteristics that can be characterized by stereological (grain sizes, shapes, grain boundary networks) or orientational (crystallographic texture) attributes. Correlations exist between stereological characteristics and properties such as grain boundary segregation [20], inter-granular corrosion [21], stress corrosion cracking [22], and creep [23]. Physical properties of interest to this work such as elastic stiffness, thermal conductivity, and initial yield-strength depend on crystallographic texture and higher order correlations of crystal orientations [24]. Crystallographic texture is mathematically represented using the orientation distribution function (ODF) which describes local densities of crystals over the orientation space. ODFs are defined based on parameterizations for the crystal lattice rotation, such as Euler-angles [25] and classes of angle-axis representations, most popular being the Rodrigues parametrization [26]. Conversion of continuous orientation space to a finite degrees of freedom for material property optimization requires discretization techniques. Most of the discretization schemes developed concentrate on global basis representations using spectral methods [25, 27, 28, 29]. An alternate approach presented in [30, 31] is used in this work that represents the ODF using a finite element discretized Rodrigues space with polynomial shape functions defined locally over each element. In contrast to the global basis functions used in the spectral representation, finite element shape functions provide local support and are especially useful for capturing sharp textures. To compute evolution of texture during deformation processes, a texture evolution equation is solved over the fundamental region using the finite element method [30].

Once microstructure evolution is correctly modelled, it becomes possible to track the variation in properties at the macroscopic scale using homogenization relationships. For linearly elastic heterogeneous solids, exact averaging theorems

and several homogenization models have been developed in [32], starting with the pioneering work of [33, 34]. There are also several contributions to the development of a similar treatment for homogenization of finitely deformed heterogeneous solids (e.g. see [35, 36, 37, 38]). These approaches allow calculation of the effective response of a polycrystalline microstructure through averaging relations. Simulation of texture evolution in polycrystals has also been well studied in the past (e.g. for a review see [27]). Many of the related works apply the Taylor-type micro-macro transition which assumes a purely kinematic constraint that all grains are subjected to the same deformation. This assumption satisfies compatibility but fails to account for equilibrium across grain boundaries. The effect of stereology and formation of disoriented regions within crystals due to non-uniform deformation are not taken into account. Although recent developments in bounding theories enable prediction of non-linears response of polycrystalline microstructures [39, 40, 41, 42, 43, 44, 45], they still do not incorporate effects such as misorientation evolution and grain boundary accommodation. In order to model these effects, several researchers have modelled discretized grain structures [46, 47, 48, 49, 50] where microstructural constituents are idealized grains with a fixed topology, or realistic polyhedral grains in two or three dimensions [51, 52]. In many of these cases, velocity-based finite element formulations [49, 51, 50] or displacement-based finite element formulations are used, frequently implemented into commercial finite element codes [48].

Alternative methods of linking length-scales have also been derived using the theory of homogenization[35]. In such models, the Taylor assumption arises naturally as a linking assumption [53] and new linking assumptions that satisfy the basic averaging theorems of [36] are identified. This thesis advances such homogenization techniques for interrogation of complex 2D and 3D microstructures

using single-crystal constitutive models based on continuum slip theory [54]. The polycrystal representative volume element is modelled with a displacement-based fully-implicit updated Lagrangian finite element formulation in thermo-mechanical loading conditions using multi-scale boundary conditions arising from the theory of large strain homogenization. Once the response at a material point is calculated, it becomes possible to model manufacturing processes such as cold forming in a multi-scale framework. This allows modelling of the effect of variation in process variables such as die and preform shapes on the final property distribution in the component. The macro-scale process modeling framework developed in [12, 55] is extended in this work to model texture development in polycrystalline materials during deformation. Evolution of the micro-scale during forming is modelled using continuum representation of texture [56] and incorporates crystal elasto-viscoplasticity through the constitutive equations in Ref. [57].

Based on the microstructure homogenization approach, it is possible to accurately model the effect of deformation on the microstructure and hence, the final properties of a metallic material. The emphasis of this thesis is on the design aspect of the problem, where our aim is to develop means to identify deformation process variables that lead to desired properties in the final product. The following means of addressing the problem are discussed: (1) selection of optimal microstructural features (2) design of process sequences and (3) design of process parameters (e.g. forging rates, die shapes). The following tasks are addressed in this work:

- Development of a graphical representation scheme that allows visualization of property-process-texture relationships and identification of optimal microstructures.
- Development of adaptive model reduction strategies for identification of op-

timal processing paths.

- Development of sensitivity analysis of microstructure homogenization for designing microstructure-sensitive properties.
- Integration of process design tools with sensitivity analysis of texture evolution for designing process parameters such as die and preform shapes in industrial forming processes.

A brief summary of the thesis discussing the salient features of the above developments and advantage over existing methodologies are presented here.

Graphical representation of texture-process-property relationships: Considering the high dimensionality of the space of microstructural features, it becomes essential to develop efficient means to represent such features for the purpose of graphical representation of process-property-structure relationships. Representation techniques such as Fourier series [25, 27, 28, 58] or localized finite element shape functions [30, 31, 56] have allowed efficient representation of crystallographic textures for optimization. However, the dimensionality of the space of all possible textures is still considerably high, prompting development of more compact representation schemes. Recently, model reduction methods [59, 60, 61, 62] has emerged that allow generation of basis functions using which dynamics of texture evolution can be modelled with a small set of coefficients without compromising accuracy.

Optimization techniques based on linear analysis for addressing this problem were first developed in [58]. While the work in [64] involved optimization in the spectral representation space for obtaining optimal processing paths, the present work establishes the mathematical tools required to perform optimization using the finite element representation. The complete set of feasible textures is simply a plane in the space of nodal values (termed 'material plane') while the similar

space in the space of spectral coefficients is a more complicated geometrical entity (termed 'material hull' in [28, 29]). Texture evolution paths can be visualized in a low dimensional space of basis coefficients for different processes in a representation called the 'process plane'. Optimization techniques presented in chapter 2 allow selection of textures in the 'process plane' that are as close as possible to optimal textures in the 'material plane'. Additionally, this allows selection of processing paths for obtaining desired stiffness and strength properties using graphical techniques.

Process sequence selection: Once the appropriate processing paths for realizing a particular property are obtained, we could perform a local optimization procedure to identify the optimal strain rates involved to realize desired properties. For this purpose, an adaptive reduced order optimization approach is proposed. ODFs from direct simulations of texture evolution are utilized from a database to help improve the efficiency of optimization. Class hierarchies of ODFs are created based on features in the form of pole density functions over prominent fiber families [30, 66] in the fundamental region. Several processing paths are associated with each class of textures, enabling identification of multiple processing sequences that can lead to the desired properties. Once the processing sequences and associated parameters are identified through classification, fine-tuning of the parameters is performed through a reduced-order gradient-based optimization approach. As demonstrated in [60], reduced order representation of the ODF results in reduction in degrees of freedom in the representation of texture and appreciable computational gains in the control of texture. However, one needs to select an ODF basis that also represents the new physical mechanisms encountered in the intermediate stages of the control problem. Such a basis is selected from the existing ODFs in the database using the adaptive basis approach [67] as reported in chapter 3.

Process parameter design: Primary industrial goal for metallic materials continues to be to lower processing costs in order to allow affordable component designs [68]. Forging of cast slabs to produce structural components is associated with material wastage which affects the product cost. Using accurate multi-scale models incorporating anisotropic behavior of microstructures, it is possible to design processes to tailor properties as well as to optimize material usage. Theoretical developments for addressing the problem at the microstructural scale without including processing effects are first addressed in Chapter 4 and 5. In chapter 6, a coupled macro-micro framework for multi-scale process design is proposed. In such an approach, sensitivities of microstructure field variables such as slip and twin resistances due to perturbations in macro-scale parameters such as forging rates, die and perform shapes are exactly defined using multi-scale sensitivity analysis. An averaging principle is developed to compute sensitivity of stress and various material properties at the macroscopic level from microstructural sensitivity fields. These sensitivities are used within a gradient-based optimization framework for computational design of metal forming processes. Chapter 5 and 6 are devoted to address the mathematical developments needed to obtain sensitivities of microstructural fields to deformation process variables and perform multi-scale optimization.

Finally, in Chapter 7, conclusions of this work and suggestions for future research are summarized.

Chapter 2

Microstructure representation and exploration of property-process-structure spaces

[1] This chapter discusses techniques for exploring texture-property-process relationships in various deformation processes as derived from a reduced-order model of texture evolution. The orientation distribution function (ODF) in polycrystals is represented over the Rodrigues space in a discrete form using finite element interpolation techniques. Linear programming algorithms are developed for retrieving ODFs with extremal or optimal properties from the complete ODF space. The relationship of optimal textures with processing is addressed by representing texture evolution in a space of reduced basis coefficients called the process plane. This involves generation of orthogonal basis functions for representing spatial variations of the ODF in a given process using proper orthogonal decomposition. These basis functions are found to work in interpolatory and extrapolatory processing modes and allow representation of texturing for deviations in the process variables. Optimization problems are posed in the reduced space for retrieving textures with desired properties.

A graphical technique is discussed that allows identification of optimal processing paths for reaching desired textures in association with process plane databases. In Section 2.1, representation of FCC texture in Rodrigues space is defined followed

[1] Reproduced from V. Sundararaghavan and N. Zabaras, "Linear analysis of texture-property relationships using process-based representations of Rodrigues space", Acta Materialia, Vol. 55, Issue 5, pp. 1573-1587, 2007.

by the reduced-order technique for computing texture evolution. In Section 2.2, we introduce linear programming techniques for obtaining extremal ODFs or desired property distributions from the material plane (i.e. from the space of all possible ODFs without considerations to processing). Section 2.3 introduces similar design problems in the process plane (i.e. in the space of reduced-order coefficients of a process basis). Section 2.4 provides an approach for selection of processing paths that realize desired properties. Discussion of limitations and potential extensions are finally discussed in Section 2.5.

2.1 Modeling of FCC texture

Orientation distribution function (ODF) [25, 27], the probability density function for orientations, is employed for the quantification of crystallographic texture. Texture evolution methodologies use parameterizations for the crystal lattice rotation which together with the crystal symmetry define the problem domain. Angle-axis representations define an alternative way of representing texture compared to the use of Euler angles [25, 69]. We employ the axis-angle parametrization of the orientation space proposed by Rodrigues [30].

2.1.1 Representation in Rodrigues space

Axis-angle parametrization is based on the unique association of an orientation with a rotation axis, and an angle of rotation about the axis. The Rodrigues' parametrization is created by scaling the axis of rotation $\mathbf{n}$ as $\mathbf{r} = \mathbf{n}tan(\frac{\theta}{2})$, where θ is the rotation angle. A proper rotation $\mathbf{R}$ relates the lattice orientation to a

reference orientation. Given the Rodrigues parametrization $\mathbf{r}$, the rotation $\mathbf{R}$ can be obtained as,

$$\mathbf{R} = \frac{1}{1 + \mathbf{r}.\mathbf{r}}(\mathbf{I}(1 - \mathbf{r}.\mathbf{r}) + 2(\mathbf{r} \otimes \mathbf{r} + \mathbf{I} \times \mathbf{r})) \tag{2.1}$$

The fundamental region represents a region of the orientation space such that each crystal orientation is represented uniquely within the space. Fundamental region for the cubic symmetry group results in a truncated cube. The planes that form the faces of the cube are introduced by symmetry rotations about the $\langle 100 \rangle$ family of axes and the corners are truncated by planes introduced by rotations about the $\langle 111 \rangle$ axes. The ODF (represented by $\mathcal{A}$) describes the local density of crystals over this fundamental region of orientation space. The volume fraction of crystals within a part ($\Re^*$) of the fundamental region is given by $v_f(\Re^*) = \int_{\Re^*} \mathcal{A} dv$. The ODF is normalized to unity over the fundamental region. Here $dv = \sqrt{det\boldsymbol{g}}\ dr_1 dr_2 dr_3$. Since the orientation space is non-Euclidean, the volume element is scaled by the term $\sqrt{det\boldsymbol{g}} = cos^4(\theta/2)$ where $\boldsymbol{g}$ is the metric for the space. If the orientation-dependent property for a single crystal $\chi(\boldsymbol{r}, t)$ is known, any polycrystal property can be expressed as an expectation value or average given by:

$$< \chi >= \int_{\mathcal{R}} \chi(\boldsymbol{r}, t)\mathcal{A}(\boldsymbol{r}, t) dv \tag{2.2}$$

The evolution of ODF is governed by the ODF conservation equation. The conventional Eulerian rate form of the conservation equation is given by [30]:

$$\frac{\partial \mathcal{A}(\mathbf{r}, t)}{\partial t} + \bigtriangledown \mathcal{A}(\mathbf{r}, t) \cdot \mathbf{v}(\mathbf{r}, t) + \mathcal{A}(\mathbf{r}, t) \bigtriangledown \cdot \mathbf{v}(\mathbf{r}, t) \ = \ 0 \tag{2.3}$$

where $\mathbf{v}(\mathbf{r}, t)$ is the Eulerian reorientation velocity. To compute the ODF evolution, the fundamental region is meshed using tetrahedral elements and the evolution equation is solved using a stabilized finite element method [30]. The reorientation

velocity in the above equation is evaluated through crystal constitutive relations. In the examples used in the ensuing sections, texturing in FCC materials with twelve $\{111\} < 110 >$ slip systems is modeled using a rate-dependent viscoplastic Taylor model with material parameters taken from [60].

2.1.2 Reduced-order model of the ODF

The discussion here follows the work in [60, 61] where model reduction of crystal plasticity was first introduced using the technique of proper orthogonal decomposition (POD). Model reduction involves generation of basis functions optimal for representing ODFs obtained from a process path. Using such basis functions, any ODF $\mathcal{A}(\boldsymbol{r}, t)$ from the time-history of ODF evolution in a given process can be approximated as follows:

$$\mathcal{A}(\boldsymbol{r}, t) = \sum_{m=1}^{b} a_m(t)\phi_m(\boldsymbol{r}) \tag{2.4}$$

In the above equation ϕ_m represents 'b' basis functions (independent of time) and $a_m(t)$ denotes the corresponding time-dependent coefficients. Once such basis functions ϕ_m are computed, time-dependent coefficients can be used to reconstruct the textures arising from the process path. Readers are referred to [60] where texture evolution is computed by using the Eq. (2.4) to convert the partial differential equation (Eq. (2.3)) to an ordinary differential equation. Texture evolution can also be computed across a set of extrapolatory regimes of the process (i.e. conditions deviating from those used to generate the basis functions) using the same set of basis functions.

The 'method of snapshots' is an efficient technique of obtaining basis functions from an ensemble of ODF data $\{\mathcal{A}(\boldsymbol{r}, t)\}_{i=1}^{\mathcal{N}}$ consisting of ODFs at various times

during texture evolution over a deformation path. Here, the basis functions ϕ take the form [60]:

$$\phi_m = \sum_{i=1}^{\mathcal{N}} u_i^m \mathcal{A}^i \tag{2.5}$$

where $\mathcal{A}^i$ represent textures from the ensemble, and u_i^m is determined by solving the following linear eigenvalue problem:

$$\boldsymbol{C}\boldsymbol{U} = \boldsymbol{\Lambda}\boldsymbol{U} \tag{2.6}$$

where $\boldsymbol{C}$ is the spatial correlation matrix defined as

$$\boldsymbol{C}_{ij} = \frac{1}{\mathcal{N}} \int_{\mathcal{R}} \mathcal{A}^i(\boldsymbol{r}) \mathcal{A}^j(\boldsymbol{r}) dv \tag{2.7}$$

$\boldsymbol{\Lambda}$ and $\boldsymbol{U}$ comprise of the eigenvalues and the eigenvectors of the system, respectively. To determine a suitable basis size b, one must ensure that the eigen-modes selected capture as much 'system energy' as possible. This is possible by selecting the basis functions that correspond to the largest eigenvalues in $\boldsymbol{\Lambda}$. Once the modes have been evaluated, the optimal basis is generated from Eq. (2.5). The coefficients $\boldsymbol{a}$ corresponding to any ODF in a deformation path can be retrieved from:

$$a_m = \int_{\mathcal{R}} \mathcal{A}(\boldsymbol{r}) \phi_m dv \tag{2.8}$$

The ODFs in the deformation path follow a curve in the space of reduced coefficients $\boldsymbol{a}$. The success of the technique for representing texture evolution was shown in [60] where just three basis functions were found to be sufficient for capturing most features of the evolving ODF in any given process. Basis functions are obtained for different processing modes using a 3403 element discretization of the fundamental region. Basis used in the examples consist of modes generated from an ensemble of data obtained for tension, shear and rolling processes up to time of 0.1 s when deformed with a strain rate of 1 s^{-1} using a time step of $\Delta t = 0.01$ s.

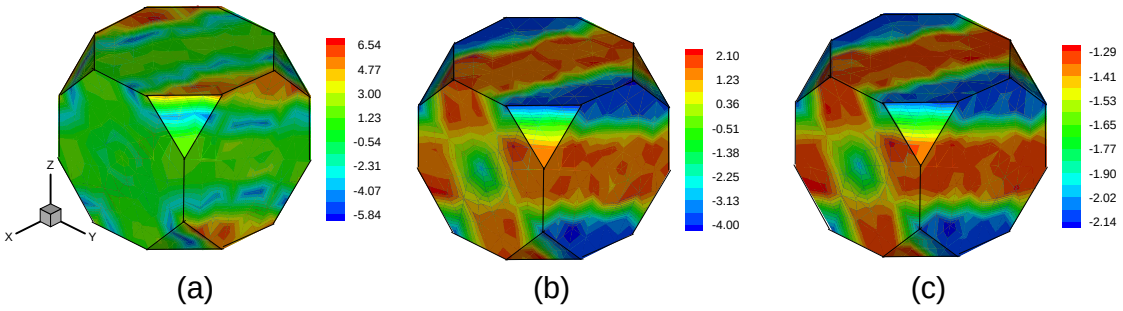

Figure 2.1: First three eigen-basis functions for the texture evolution in a tension process from a initial random texture with a strain rate of 1 s^{-1}.

Fig. 2.1 shows the three major basis functions of the tension process. The basis depends upon the initial texture $\mathcal{A}(\boldsymbol{r}, t = 0)$ that is used in the solution of ODF evolution (Eq. 2.3). However, the strength of POD analysis used here lies in the fact that the reduced basis works in extrapolatory modes to represent texturing under various deviations in the initial texture. As a result, ODFs resulting from processing to a different strain or processing a starting texture that deviates from the one used to build the basis are well approximated using the same set of basis functions. Different basis functions are generated to simulate different process sequences [62]. The reduced modes used to represent the deformation path are different, for example, when modeling tension process on a rolled specimen compared to a process of tension acting on an annealed specimen with random texture.

2.2 Property representation and optimization in Rodrigues space

Finite element discretization of the orientation space and associated integration schemes using Gauss quadrature allows matrix representation of several properties

of the ODF. ODF is assumed to be discretized into N independent nodes with N_{elem} finite elements and N_{int} integration points per element. The constraint that the ODF is normalized to unity over the fundamental region can then be written as:

$$\int_{\mathcal{R}} \mathcal{A} dv = \sum_{n=1}^{N_{elem}} \sum_{m=1}^{N_{int}} A(\boldsymbol{r}_m) w_m |J_n| \frac{1}{(1 + \boldsymbol{r}_m \cdot \boldsymbol{r}_m)^2} = 1, \tag{2.9}$$

where $A(\boldsymbol{r}_m)$ is the value of the ODF at the m-th integration point with global coordinate $\boldsymbol{r}_m$ of the n-th element, $|J_n|$ is the jacobian determinant of the n-th element and w_m is the integration weight associated with the m-th integration point. This is equivalent to the linear constraint: $\boldsymbol{q}^{int^T} \boldsymbol{A}^{int} = 1$, where $q_i^{int} = w_i |J_i| \frac{1}{(1+r_i \cdot r_i)^2}$ and $A_i^{int} = A(\boldsymbol{r}_i)$, where each i corresponds to a combination (n, m), $i = 1, \ldots, N_{int} \times N_{elem}$. If the orientation-dependent property for a single crystal $\chi(\boldsymbol{r})$ is known, any polycrystal property can be expressed in a linear form as follows:

$$< \chi >= \int_{\mathcal{R}} \chi(\boldsymbol{r}) \mathcal{A}(\boldsymbol{r}) dv = \sum_{n=1}^{nel} \sum_{m=1}^{nint} \chi(\boldsymbol{r}_m) A(\boldsymbol{r}_m) w_m |J_n| \frac{1}{(1 + \boldsymbol{r}_m \cdot \boldsymbol{r}_m)^2} \tag{2.10}$$

This is again equivalent to an equation linear in the ODF: $< \chi >= \boldsymbol{p}^{int^T} \boldsymbol{A}^{int}$, where $p_i^{int} = \chi(\boldsymbol{r}_i) w_i |J_i| \frac{1}{(1+r_i \cdot r_i)^2}$ and $A_i^{int} = A(\boldsymbol{r}_i)$, $i = 1, \ldots, N_{int} \times N_{elem}$.

An additional constraint in the representation of the material set is the symmetry of the ODF. Orientations on each pair of planes in the fundamental region are equivalent under the symmetries. In the cubic fundamental region, orientations on the faces are identified with orientations on the diametrically opposed faces following rotations through $\pi/4$ about the corresponding $< 100 >$ axes. Similarly, symmetric orientations on the various $\{111\}$ faces are obtained following rotations through $\pi/3$ about the $< 111 >$ axes. The space of ODF values at integration

points of the FE mesh does not represent this symmetry. Symmetry conditions are enforced by considering the set of independent nodal points instead of the integration points. Independent nodal points are the reduced set of nodes obtained by accounting for symmetry conditions at the boundaries of the ODF. Let $\boldsymbol{H}$ be the matrix converting the independent nodal values $\boldsymbol{A}^{node}$ to the integration point values $\boldsymbol{A}^{int}$ through the shape functions, then, $\boldsymbol{A}^{int} = \boldsymbol{H}\boldsymbol{A}^{node}$. The independent nodal values $\boldsymbol{A}^{node}$ are sufficient to describe the ODF due to the symmetry of the fundamental region. Vector containing the values of the ODF at independent nodal points $\boldsymbol{A}^{node}$ is hereafter referred to as $\boldsymbol{A}$. The ODF constraint can then be written in terms of the modified $\boldsymbol{q}^T = \boldsymbol{q}^{int^T}\boldsymbol{H}$ as $\boldsymbol{q}^T\boldsymbol{A} = 1, \boldsymbol{A} \geq 0$. Properties are specified using the modified $\boldsymbol{p}^T \equiv \boldsymbol{p}^{int^T}\boldsymbol{H}$ as $< \chi >= \boldsymbol{p}^T\boldsymbol{A}$. Another constraint is based on the positivity of the ODF which constrains the nodal values of the ODF to be positive ($\boldsymbol{A} \geq 0$). Space of all possible ODFs thus includes three constraints: normalization, positiveness and symmetry. The constraint $\boldsymbol{q}^T\boldsymbol{A} = 1, \boldsymbol{A} \geq 0$ means that the complete set of all possible ODFs is a hyperplane in the space of independent nodal values, which we call the 'material plane'. Optimization to obtain ODFs with extremal properties from this representation is described in the next section.

Formation of property ($\boldsymbol{p}$) and constraint ($\boldsymbol{q}$) matrices: For calculating more than one property, $\boldsymbol{p}$ is written in a matrix form. The form of $\boldsymbol{p}$ and $\boldsymbol{q}$ for the design problems addressed here is provided below. A variety of higher order integration techniques can be used to accurately estimate properties from the finite element disretization of the orientation space. For simplicity, the discussion in this chapter uses reduced integration, which for a tetrahedral element used to discretize the fundamental region, translates to one integration point per element. Using reduced integration at local coordinate of each element $(0.25, 0.25, 0.25)$ and

an integration weight of $w = \frac{1}{6}$ at each integration point, the simplified property matrix $\boldsymbol{p}^{int}$ corresponding to polycrystal average properties $[< \chi_1 >, \ldots, < \chi_{n_p} >]$ and the normalization constraint vector ($\boldsymbol{q}^{int}$) are given as:

$$\boldsymbol{p}^{int} = \begin{bmatrix} \frac{1}{6}\chi_1(\boldsymbol{r}_1)|J_1|\frac{1}{(1+r_1\cdot r_1)^2} & \ldots & \frac{1}{6}\chi_{n_p}(\boldsymbol{r}_1)|J_1|\frac{1}{(1+r_1\cdot r_1)^2} \\ \frac{1}{6}\chi_1(\boldsymbol{r}_2)|J_2|\frac{1}{(1+r_2\cdot r_2)^2} & \ldots & \frac{1}{6}\chi_{n_p}(\boldsymbol{r}_2)|J_2|\frac{1}{(1+r_2\cdot r_2)^2} \\ \ldots & & \\ \frac{1}{6}\chi_1(\boldsymbol{r}_{N_{el}})|J_{N_{el}}|\frac{1}{(1+r_{N_{el}}\cdot r_{N_{el}})^2} & \ldots & \frac{1}{6}\chi_{n_p}(\boldsymbol{r}_{N_{el}})|J_{N_{el}}|\frac{1}{(1+r_{N_{el}}\cdot r_{N_{el}})^2} \end{bmatrix}$$

$$\boldsymbol{q}^{int} = \begin{bmatrix} \frac{1}{6}|J_1|\frac{1}{(1+r_1\cdot r_1)^2} \\ \frac{1}{6}|J_2|\frac{1}{(1+r_2\cdot r_2)^2} \\ \ldots \\ \frac{1}{6}|J_{N_{el}}|\frac{1}{(1+r_{N_{el}}\cdot r_{N_{el}})^2} \end{bmatrix}$$

The $\boldsymbol{H}$ matrix can be defined from the equation $A_e^{int} = 0.25\sum_{i=1}^{4} A_e^i$ where A_e^{int} is the integration point ODF value at element e and $A_e^i, i = 1, \ldots, 4$ refers to the ODF values at the four nodes of the tetrahedral element e. The $\boldsymbol{p}$ matrix is formed as $\boldsymbol{p} = \boldsymbol{H}^T\boldsymbol{p}^{int}$ so that any property $\boldsymbol{d}$ can be represented as the scalar product $\boldsymbol{p}^T\boldsymbol{A}$ with the ODF values ($\boldsymbol{A}$) at the independent nodal points.

2.2.1 Calculation of properties

For the examples in this section, the property matrix $\boldsymbol{p}$ corresponding to polycrystal average properties $[< \chi_1 >, \ldots, < \chi_{n_p} >]$ is generated for calculating the diagonal components of the stiffness matrix and the Taylor factor representing the material strength. The methodologies used for the calculation of these properties are briefly explained here.

1. Polycrystal stiffness calculation: Values of elastic parameters for FCC copper crystal are taken as $c_{11} = 168.0GPa, c_{12} = 121.4GPa, c_{44} = 75.4GPa$. The polycrystal stiffness, $\bar{\boldsymbol{C}}$, is computed through a weighted average (over $\mathcal{A}$) of the stiffness of individual crystals expressed in the sample reference frame. The average values result in upper bound for the diagonal values of the stiffness matrix.

2. Yield strength calculation: The relationship between the macroscopic effective yield strength Y, and average slip system hardness τ, can be expressed using the Taylor factor M as follows:

$$Y = \sigma_{ij} \frac{d\epsilon_{ij}}{d\eta} = M\tau \tag{2.11}$$

Bishop and Hill analysis is used to determine the stress states (σ_{ij}) for a given deformation in the above equation. Let us apply a deformation to the polycrystal given by the following strain:

$$d\epsilon = d\eta \begin{bmatrix} 1 & 0 & 0 \\ 0 & -0.5 & 0 \\ 0 & 0 & -0.5 \end{bmatrix} \tag{2.12}$$

where the principal directions correspond to the rolling direction (RD), transverse direction (TD) and the normal direction (ND). η can be considered as the absolute amount of the deformation. For a FCC crystal there are 56 stress states which could activate five or more slip systems simultaneously. For a given shape change (here Eq. (2.12)), the crystal stress state which produces the maximum work is active and the Taylor Factor is calculated corresponding to that stress state, from which one can compute the yield stress. More details about this method can be found in Chapter 4 of [6]. To compute the yield stress for different angles to the rolling direction the procedure is the same as above but with applied deformation state (Eq. (2.12)) rotated by the appropriate angle to the rolling direction. The polycrystal Taylor factor $< M >$ can then be determined by averaging using

Eq. (2.2). The random texture value thus computed compares well with the actual value $Y/\tau = 3.067$ for a random polycrystal [6]. Note that the linear relationship provided here computes the strength corresponding to yielding under the particular deformation mode given by Eq. (2.12) and is not related to either the bounds on yield strength or the uniaxial tensile yield strength. Interested readers are referred to [70] for the methodology used to compute upper bound of uniaxial yield strength, in which case, the deformation is varied so that a uniaxial stress state results in the polycrystal.

2.2.2 Linear programming for property optimization

Linear programming (LP) allows us to address problems involving linear objective function and linear constraints using techniques such as the simplex and the interior point algorithms. General problems that can be solved using linear programming involve a set of equality constraints and a set of inequality constraints as given below [71]:

$$\min_{\boldsymbol{x}} \boldsymbol{f}^T\boldsymbol{x} \text{ such that } \boldsymbol{M}\boldsymbol{x} \ \leq \ \boldsymbol{m},\ \boldsymbol{P}\boldsymbol{x} = \boldsymbol{d},\ lb \leq \boldsymbol{x} \leq ub \tag{2.13}$$

Methods for identifying ODFs with extremal or desirable properties and obtaining property closures from the complete ODF space (the 'material plane') are discussed next. Later sections deal with problems of similar character using a reduced-order representation where we emphasize on process selection strategies for obtaining optimal properties.

Identification of textures with extremal properties Geometrically, linear constraints define a convex polyhedron, which is called the feasible region.

Such problems have some interesting properties including the fact that all local optima are automatically global optima and the optimal solution can only occur at a boundary point of the feasible region. This allows extraction of ODFs with global extrema properties, also called 'extremal ODFs'. The problem of generating extremal ODFs uses $\boldsymbol{x} = \boldsymbol{A}$ as the variable to be identified such that property $\boldsymbol{p}^T\boldsymbol{A}$ is maximized with the constraints that $\boldsymbol{q}^T\boldsymbol{A} = 1$ and $\boldsymbol{A} > 0$. An example is shown in Fig. 2.2 where extremal ODFs that maximize a few strength and stiffness properties in FCC Cu are provided. As is evident from the plots, extremal ODFs correspond to microstructures with a unique set of orientations (and symmetric equivalents). Extremal ODFs correspond to Dirac delta functions at these orientations. Extremal textures that lead to maximal strength properties are dominated by specific fibers in the orientation space. For example, Fig. 2.2(a) shows that the ODF for maximum Taylor factor along the rolling ($x-$) direction is dominated by the x-axis $< 110 >$ fiber. Uniaxial compression along x-axis is a natural way to obtain strong texturing along this fiber to increase the yield strength along the rolling direction. Extremal ODFs are calculated using a mesh with 12096 tetrahedral elements over the orientation space. Note that in examples (a) and (b) in Fig. 2.2, objectives are defined so as to optimize the Taylor factor calculated along the rolling direction and the transverse direction.

Range of properties obtainable from the material plane

Property closures represent complete range of properties obtainable from the space of ODFs. These are approximated by the space between upper and lower bounds of the given property. Upper bound closure of diagonal stiffness values in FCC Cu represent the range of properties obtainable by the upper bound homogenization relation in Section 2.2. The hull in Fig. 2.3(a), for example, maps the full

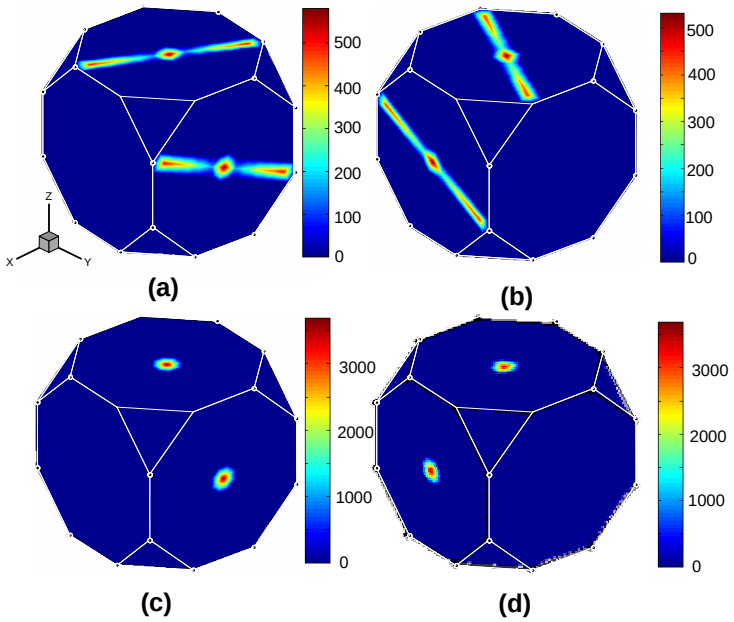

Figure 2.2: Extremal ODFs for different properties: (a) ODF for maximum Taylor factor along RD (= 3.668), (b) ODF for maximum Taylor factor along TD (= 3.668), (c) ODF for maximum C_{44} (= 74.923 GPa) and (d) ODF for maximum C_{55} (= 74.923 GPa.

range of upper bound values of a combination of diagonal stiffness values. In Section 2.2.2 where we consider extreme points for a single property, the extremal textures were found to correspond to single crystals. The closure in this case can indeed be calculated in a straightforward manner by searching over all single crystals. Computation of multi-property closures entails maximization of one property while enforcing constraints on other properties. Extreme points in such closures, however, are found to result in polycrystalline textures [58]. Linear programming as discussed previously provides a convenient way of automating the search for extremal textures in the material plane for calculating multi-property closures. Let v_1, v_2 be the set of properties for which the closure is required. The closure for property v_1 is first found by obtaining the extremal values (v_{1max}, v_{1min}) as explained in Section 2.2.2. Then, property v_1 is discretized into m values $v_1^i, i = 1, .., m$

between v_{1max} and v_{1min}. The property closure of the combined set of properties (v_1, v_2) is found by executing a similar extremum LP problem at each point v_1^i with the additional constraint that $\boldsymbol{p}_1^T \boldsymbol{A} = v_1^i$. In general, the closure for a combined set of n properties $(v_1, v_2, ..., v_n)$ is a n-dimensional volume found by executing an LP problem extremizing v_n at a set of discrete points $(v_1^i, v_2^j, .., v_{n-1}^l)$ in the closure area of $(v_1, v_2, .., v_{n-1})$. The corresponding LP problem for minimizing v_n is written below:

$$\begin{aligned} \min_{\boldsymbol{A}} v_n = \boldsymbol{p}_n^T \boldsymbol{A} \text{ satisfying the constraints} \\ \boldsymbol{q}^T \boldsymbol{A} = 1 \\ \boldsymbol{A} > 0 \\ \boldsymbol{p}_1^T \boldsymbol{A} = v_1^i \\ \boldsymbol{p}_2^T \boldsymbol{A} = v_2^j \\ ... \\ \boldsymbol{p}_{n-1}^T \boldsymbol{A} = v_{n-1}^l \end{aligned} \tag{2.14}$$

To maximize v_n another similar problem is executed where the objective is changed as $\min_{\boldsymbol{A}} v_n = -\boldsymbol{p}_n^T \boldsymbol{A}$.

The full range of Taylor factors is also shown in Fig. 2.3(b). The closure represents the range of properties obtainable when using the homogenization methodology given in Section 2.2.

Identification of ODFs with desired distribution of properties

Problems involving identifications of ODFs with desired combination of several different properties can be performed using the following methodology. The problem

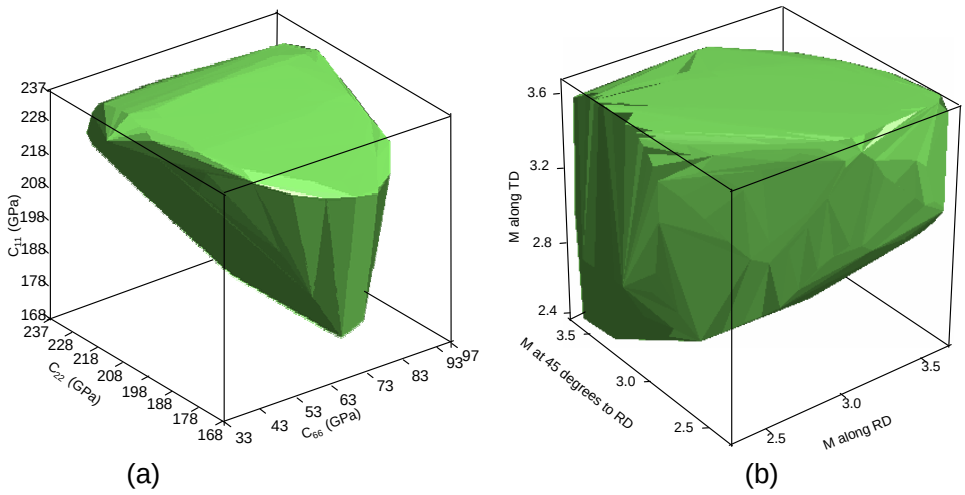

Figure 2.3: Space of properties obtainable using the linear homogenization relations in Section 2.2 (a) The range of combinations of three upper bound stiffness constants $[C_{11}, C_{22}, C_{66}]$. The computed space corresponds to the upper bound property closure for these stiffness constants. (b) The property hull for strength showing all possible combinations of the Taylor factor computed along three directions (RD, 45 degrees to RD and TD).

is posed as identification of ODF that minimizes the absolute value of error from a desired set of properties, $\min_{\boldsymbol{A}} e_0$ such that $\boldsymbol{p}^T\boldsymbol{A} + \boldsymbol{e} = \boldsymbol{d}$, where $\boldsymbol{d}$ is the desired property set and $\boldsymbol{q}^T\boldsymbol{A} = 1$. Positivity of the ODF dictates the constraint $\boldsymbol{A} \geq 0$. We specify a bound $e_0 \geq 0$ in the value of the error from a desired property set which is the quantity that is minimized. This additional constraint is defined as $|e_i| \leq e_0$, for $i = 1, \ldots, n_p$, where n_p denotes the number of properties to be optimized. This is equivalent to pairs of linear inequalities of the form, $-e_i - e_0 \leq 0$ and $e_i - e_0 \leq 0$. This LP problem uses $\boldsymbol{x} = [e_1, \ldots, e_{n_p}, \boldsymbol{A}, e_0]$ as the variable to be identified. The error e_i is allowed to be of either sign. The constraints are posed by augmenting the $\boldsymbol{p}$ and $\boldsymbol{q}$ matrices (provided in Appendix A) to form the complete linear system of equality constraints.

Although the algorithm highlighted here presents means to identify optimal

ODFs on the 'material plane', it does not ensure that such ODFs can be realized through processing. We discuss the reduced basis technique in the next section that allows affiliation of deformation process paths and ODFs with optimal properties.

2.3 Reduced representation of the ODF for property optimization in deformation processes

The search for optimal ODFs in the 'material plane' did not incorporate any physical aspects of texture evolution. However, the reduced basis technique explained in Section 2.1.2 allowed representation of texture evolution in a given process using b basis functions ϕ as $A = \sum_{m=1}^{b} a_m \boldsymbol{\phi}_m \geq 0$. Any ODF from this processing path was represented completely in the space of coefficients $\boldsymbol{a} = [a_1, \ldots, a_b]^T$. Such a representation allows visualization of textures from any given process in the space of reduced coefficients which we call the 'process plane'. Similar to the constraints in the 'material plane', this space also invokes the positiveness, normalization and symmetry constraints. The normalization constraint in this reduced space is given as $\int_{\mathcal{R}} \sum_{m=1}^{b} a_m \boldsymbol{\phi}_m dv = 1$. Based on this, the equation of the reduced material plane is given as $\sum_{m=1}^{b} a_m \varphi_m = 1$ where $\int_{\mathcal{R}} \boldsymbol{\phi}_m dv = \varphi_m$ with the positiveness constraint $\sum_{m=1}^{b} a_m \boldsymbol{\phi}_m \geq 0$. Here, $\boldsymbol{\phi}_m$ corresponds to the ODF values at the independent nodal locations of the basis. The additional constraint on symmetry that was applied previously for the material plane is not required in the space of reduced-order coefficients since the individual basis functions themselves are periodic and thus, symmetry constraints are enforced on any linear combination of this basis.

Planar representation of the universe of ODFs obtained from a tension process

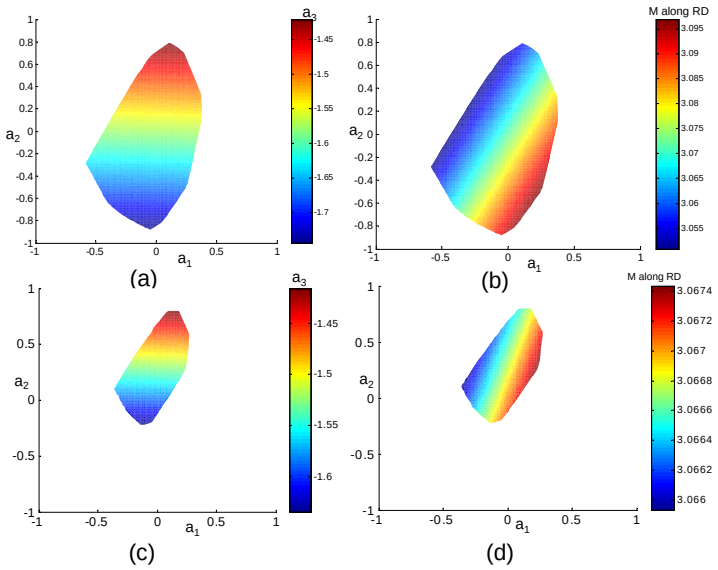

Figure 2.4: (a) Process planes for a tension process with a random initial texture. (b) Process plane for tension colored by property (Taylor factor along RD). Figures (c) and (d) show similar process plane representations for shear in the $x - y$ plane.

acting on a sample with a random starting texture is shown in Fig. 2.4(a). Since the constraints are themselves linear, the process plane in Fig. 2.4(a) is seen as a simple and convex polygon compactly represented close to the origin of the space of reduced coefficients. The process plane is described in a three-dimensional space of reduced-order coefficients $[a_1, a_2, a_3]$. The plane can be conveniently visualized in two-dimensions of $[a_1, a_2]$ by coloring the points on the plane based on the third dimension a_3. Each point on the process plane in Fig. 2.4(a) corresponds to an ODF realization. Properties corresponding to these ODFs can be visualized on this plane using color contours on the process plane. Fig. 2.4(b) shows color contours of the Taylor factor along the rolling direction on the process plane. The third dimension (a_3) is not shown in the property plot since, using Fig. 2.4(a) the z-coordinate of any point can be retrieved. Figs. 2.4(c) and 2.4(d) show similar process plane representations for the process of $x - y$ shear.

2.3.1 Processing paths on the process plane

The primary success of proper orthogonal decomposition (POD) is the ability of the reduced basis functions to represent textures arising from various perturbations in conditions used in generating the basis. Robust performance of the basis functions under interpolations and extrapolations of process conditions has especially found applications in other areas such as fluid flow simulation and control problems [72]. Quantification of the extrapolatory limits of performance of the reduced modes requires extensive experimentation. Indeed, there have been many such studies in different fields (e.g. [73]) devoted to identifying the level of extrapolation that can be accommodated by POD modes within desired robustness limits. One such study is presented here where we quantify the error in representation of an ODF on the process plane as $100 \times \frac{\|\mathcal{A}-\mathcal{A}^{rec})\|_2}{\|\mathcal{A}\|_2}$, where $\mathcal{A}$ is the actual ODF resulting from the process (from full-order simulation) and $\mathcal{A}^{rec}$ is the ODF reconstructed from the coefficients of the reduced-order basis along the path identified in the process plane.

Fig. 2.5(a) shows a process plane constructed using basis functions generated from an ensemble of textures where an initial random texture is deformed to 0.1 strain under x-axis tension. The ensemble consisted of 10 sets of texture snapshots (obtained at times $\mathcal{T} = \{0.01, 0.02, .., 0.1\}$ secs) from crystal plasticity simulation of the process at a strain rate of $1sec^{-1}$. The 'process plane' represents all possible ODFs that can be generated using the set of basis functions obtained from this ensemble and represents ODFs from the x-axis tension process for various deviations in strains and initial textures from those used for constructing the ensemble. The ensemble of ODFs used to construct the basis functions are represented as points along the path $R - R'$ on the process plane. Two different points are chosen on the

process plane with ODFs deviating by 10% from the random ODF. These ODFs were subjected to x-axis tension up to 0.1 strain. The different resulting points obtained at times $\mathcal{T}$ in these process paths are depicted on the process plane as curves A-A' and B-B'. The actual ODFs obtained from a crystal plasticity simulation of the process follow a path on the high-dimensional 'material plane' and cannot be easily visualized. It was verified numerically that the points shown on these process paths on the x-axis tension 'process plane' reconstruct the actual ODFs within an error of 2%.

Another example for extrapolatory performance is depicted in a x-axis tension process plane shown in Fig. 2.5(b). The ensemble from which the basis functions for this process plane was generated also corresponds to snapshots for x-axis tension up to 0.1 strain, but the difference from the earlier example being that the initial texture in this case is obtained from y-axis rolling of a random texture to 0.1 strain. Textures in the ensemble used to generate the basis functions at times $\mathcal{T}$ are represented as points on the curve $A - A'$ in the process plane in Fig. 2.5(b). We now consider two other process paths where the initial texture for the tension process is changed by varying the strain involved in the rolling process to 0.17 and 0.07. The points in these two process paths computed at times $\mathcal{T}$ are represented with the curves $B - B'$ and $C - C'$, respectively in the figure. These extrapolatory process paths are within 2% error of the actual ODF paths in the process plane.

The lines $m - m'$ and $n - n'$ at the left and right in Fig. 2.5(b) delineate the region within which the error in reconstruction of textures in the processing path is less than 10% when compared to textures from a full-order simulation. These curves are generated by comparing actual textures generated from crystal plasticity simulations with textures represented on the process plane when initial textures

corresponding to different strains in the y-axis rolling process are deformed in x-axis tension. The curves bound the extrapolation in the initial texture that can be tolerated and follow the process path of these initial textures. This points to the fact that process paths of optimal textures falling within such a region can be predicted with reasonable accuracy. However, process paths traversing points at the far left and right corners of the process plane possess larger errors in reconstruction and thus, the process resulting in these textures cannot be established with confidence. Process selection strategies described later in this work do not incorporate knowledge of inaccessible regions of the process plane. There are situations where an optimal ODF computed could lie in regions (e.g. edges of the process plane) that are inaccessible. An ad hoc way of addressing the problem is to disregard solutions that are close to the edges of the process plane.

In addition to variations in the initial texture, the same basis also works for extrapolations of strains used in constructing the basis. For example, Fig. 2.5(b) shows the texturing paths (points on these paths computed again at times $\mathcal{T}$) a-a', b-b' and c-c' for x-axis compression to strain of 0.1 with the same initial textures as discussed before, captured within an error of 2%. In principle, it is also possible to construct basis functions using a combined ensemble of textures from different processes in a process sequence. Such basis functions would be able to represent the actual textures (or process path) from all processes in the sequence within a single process plane. The only difficulty with such an approach is that more than three basis functions are required to capture the textures and consequently, the process planes are not amenable to plotting and visualization.

Naive methodologies for selection of process sequences depend on a large database of computed processing paths requiring a large number of crystal plasticity simula-

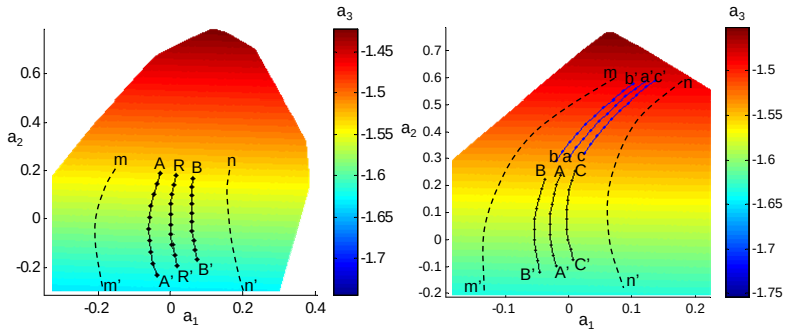

Figure 2.5: (a) Process plane for x-axis tension (ensemble obtained by processing an initial random texture to 0.1 strain). Point R corresponds to a random texture, points A and B represent initial textures that deviate from the random texture by 10%. Texture path R-R', A-A' and B-B' are process paths when these initial textures are subjected to x-axis tension up to 0.1 strain. (b) Process plane for x-axis tension process (ensemble obtained by processing the texture obtained by y-axis rolling of a random texture to 0.1 strain to an additional 0.1 strain under x-axis tension). The process paths on the x-axis tension plane for a strain in the y-axis rolling process of 0.1, 0.07 and 0.17 are marked A-A', C-C' and B-B', respectively. Paths a-a', c-c' and b-b' represent the texture paths for x-axis compression to strain of 0.1 with these initial textures. In both figures, m-m' and n-n' delineate the region within which reconstruction of textures from such process paths is at least 90% accurate.

tions. Use of process planes for performing process sequence selection is a concept worth pursuing since a process plane constructed from a single simulation captures a number of extrapolatory processing paths. Thus, a search for optimal ODFs over a large set of computed process paths is replaced with a search over a smaller set of process planes. Analysis in the rest of the section introduces methods for identifying process sequences that can be used to reach desired final properties. Once a process sequence is established, existing optimization techniques such as the gradient based techniques in [60, 61, 62] can be used to identify parameters such as strain rates for each processing stage. Computational details and key issues in process plane optimization problems are presented in detail in the following sections.

2.3.2 Identification of ODFs (from a given process) closest to an optimal ODF in the 'material plane'

As described in Section 2.2.2, location of optimal ODFs on the 'material plane' does not convey information on how to realize such ODFs in practice. There may be several processing solutions to this problem. Here, we choose a particular processing path and check if it can closely produce an optimal texture in the material plane. The optimal ODF from the 'material plane' is assumed to be given by a perturbation ($\boldsymbol{r}$) to an ODF in the 'process plane'. We wish to minimize the perturbation from the 'process plane' in some sense such that an ODF from the process plane is as close as possible to the optimal ODF in the material plane.

The optimal ODF is written as $\boldsymbol{A}_{opt} = \sum_{m=1}^{b} a_m \boldsymbol{\phi}_m + \boldsymbol{r} > 0$, where $\boldsymbol{A} = \sum_{m=1}^{b} a_m \boldsymbol{\phi}_m$ provides the closest solution in the basis $\boldsymbol{\phi}$ and $\boldsymbol{r}$ is the perturbation (or error) from the optimal ODF. The normalization constraint is given as $\boldsymbol{q}^T \boldsymbol{A}_{opt} = 1$, and $\boldsymbol{q}^T \boldsymbol{A} = 1$ such that in the LP problem, the former constraint is equivalently specified as $\boldsymbol{q}^T \boldsymbol{r} = 0$. The bound in the value of the solution ODF from the given ODF, $r_0 \geq 0$, is minimized. The problem is posed as $\min_{\boldsymbol{a}} r_0$ such that $\boldsymbol{p}^T \sum_{m=1}^{b} a_m \boldsymbol{\phi}_m + \boldsymbol{p}^T \boldsymbol{r} = \boldsymbol{d}$, where $\boldsymbol{d}$ is the desired property distribution. Positivity of the optimal ODF dictates the constraint $\boldsymbol{A} + \boldsymbol{r} \geq 0$. In the solution procedure, the basis ($\boldsymbol{\phi}_m$) and the error ($\boldsymbol{r}$) are represented as a vector containing values at independent nodes (set of nodes representing distinct orientations while accounting for crystal symmetries). The ODF in the basis also requires the positivity constraint $\sum_{m=1}^{b} a_m \boldsymbol{\phi}_m \geq 0$. The additional constraint on the bound in the value of the solution ODF from the given ODF is defined as $|r_i| \leq r_0$ equivalent to pairs of linear inequalities: $-r_i - r_0 \leq 0$ and $r_i - r_0 \leq 0$, $i = 1, \ldots, N$, where N is the number of independent nodes. This problem uses $\boldsymbol{x} = [r_1, \ldots, r_N, a_1, \ldots, a_b, r_0]^T$

as the variable to be identified. The error (r_i) from the nodal values of the optimal ODF is allowed to be of either sign. Interested readers are referred to Appendix B which provides details on the LP implementation of this problem.

Fig. 2.6 depicts an example where the problem is to identify the point on a process plane that best represents an optimal ODF in the material plane with desired stiffness properties $\{c_{11} = 210.8575GPa, c_{22} = 210.4191GPa, c_{66} = 66.3110GPa\}$. The basis functions $\{\boldsymbol{\phi}_1, \boldsymbol{\phi}_2, \boldsymbol{\phi}_3\}$ for the process plane considered for this problem were generated from snapshots for x-axis tension up to 0.1 strain of an initial texture that was obtained from y-axis rolling of a random texture to 0.1 strain. The process plane is then constructed from the equations $a_1\varphi_1 + a_2\varphi_2 + a_3\varphi_3 = 1$, where $\varphi_i = \int_V \boldsymbol{\phi}_i dv$ with the constraint $a_1\boldsymbol{\phi}_1 + a_2\boldsymbol{\phi}_2 + a_3\boldsymbol{\phi}_3 \geq 0$. Texturing during the x-axis tension process for various deviations in strain involved during the y-axis rolling process trace curves (process paths) along this plane as shown by paths 1, 2 in Fig. 2.6(b) with the initial point being the textures obtained for various perturbations in strains of the y-axis rolling process and rest of the points following the plane dynamics based on the basis functions ($\boldsymbol{\phi}$).

Formation of augmented system in LP problems. Augmented LP problem for the algorithm in Section 2.3.2 is presented here. Problem objective is identification of an ODF satisfying given property values ($\boldsymbol{d}$) in the 'material plane' that is closest to a 'process plane'. The equality constraint is specified by three independent equations as described in Section 2.3.2:

$$\begin{aligned} \boldsymbol{p}^T(\sum_{m=1}^{b} a_m\phi_m + \boldsymbol{r}) &= d \\ \boldsymbol{q}^T(\sum_{m=1}^{b} a_m\phi_m) &= 1 \\ \boldsymbol{q}^T\boldsymbol{r} &= 0. \end{aligned}$$

Three basis functions ϕ_1, ϕ_2 and ϕ_3 with corresponding coefficients a_1, a_2 and a_3 are used to fully represent the ODFs during a particular process. The unknowns in the LP tableau are then written as $\boldsymbol{x} = [r_1, \ldots, r_N, a_1, a_2, a_3, r_0]^T$. Thus, the augmented system combining the constraints in Eq. (2.15) can be written as $\boldsymbol{P}_{aug}\boldsymbol{x} = \boldsymbol{b}$ where $\boldsymbol{b} = [\boldsymbol{d}, 1, 0]^T$ and

$$\boldsymbol{P}_{aug} = \begin{bmatrix} \boldsymbol{p}^T & \boldsymbol{p}^T\boldsymbol{\phi}_1 & \ldots & \boldsymbol{p}^T\boldsymbol{\phi}_3 & 0 \\ \boldsymbol{0}_{N\times 1}^T & \boldsymbol{q}^T\boldsymbol{\phi}_1 & \ldots & \boldsymbol{q}^T\boldsymbol{\phi}_3 & 0 \\ \boldsymbol{q}^T & 0 & \ldots & 0 & 0 \end{bmatrix}$$

Similar augmentations are performed for the inequality constraints for the problem given as:

$$\begin{aligned} -r_i - r_0 &\leq 0 \\ r_i - r_0 &\leq 0 \\ \sum_{m=1}^{b} a_m\phi_m + \boldsymbol{r} &\geq 0 \\ \sum_{m=1}^{b} a_m\phi_m &\geq 0 \end{aligned}$$

The augmented system combining the constraints in Eq. (2.15) can be written as $\boldsymbol{M}_{aug}\boldsymbol{x} \leq \boldsymbol{0}$ where each row of $\boldsymbol{M}_{augmented}$ corresponds to the inequalities in Eq. (2.15) as indicated below:

$$\boldsymbol{M}_{aug} = \begin{bmatrix} -\boldsymbol{I}_{N\times N} & \boldsymbol{0}_{N\times 1} & \boldsymbol{0}_{N\times 1} & \boldsymbol{0}_{N\times 1} & -\boldsymbol{1}_{N\times 1} \\ \boldsymbol{I}_{N\times N} & \boldsymbol{0}_{N\times 1} & \boldsymbol{0}_{N\times 1} & \boldsymbol{0}_{N\times 1} & -\boldsymbol{1}_{N\times 1} \\ -\boldsymbol{I}_{N\times N} & -\boldsymbol{\phi}_1 & -\boldsymbol{\phi}_2 & -\boldsymbol{\phi}_3 & \boldsymbol{0}_{N\times 1} \\ -\boldsymbol{0}_{N\times N} & -\boldsymbol{\phi}_1 & -\boldsymbol{\phi}_2 & -\boldsymbol{\phi}_3 & \boldsymbol{0}_{N\times 1} \end{bmatrix}$$

where $\boldsymbol{I}$ is the identity matrix and the notation $\boldsymbol{1}_{N\times 1}$ and $\boldsymbol{0}_{N\times 1}$ indicates a vector of ones and zeros, respectively, of size $N \times 1$. The objective is to minimize the bound on the error $\boldsymbol{r}$ given by r_0. The objective is given as $\boldsymbol{f}^T\boldsymbol{x}$ where

$$\boldsymbol{f} = \begin{bmatrix} \boldsymbol{0}_{1\times N} & \boldsymbol{0}_{1\times 3} & 1 \end{bmatrix}^T$$

Thus, the final LP problem reduces to the solution of the following problem:

$$\min_{\boldsymbol{a}} \boldsymbol{f}^T \boldsymbol{x} \text{ satisfying the constraints}$$

$$\boldsymbol{P}_{aug}\boldsymbol{x} = \boldsymbol{b}$$

$$\boldsymbol{M}_{aug}\boldsymbol{x} \leq \boldsymbol{0}$$

Our objective is to identify the location $\{a_1, a_2, a_3\}$ on the process plane which best represents the optimal ODF on the 'material plane'. Once this location is found, the process path on which the point lies can be identified. The desired stiffness constants and the stiffness constants for the optimal ODF identified in the process plane using the procedure above are compared in Fig. 2.6(a). The ODF in the material plane that obtains the desired property is shown in Fig. 2.6(d) but the processing route for this ODF is unknown. The ODF from the process that closely represents this ODF is shown in Fig. 2.6(c). This ODF is represented by the point A' on the process plane shown in Fig. 2.6(b). From the fact that the ODF in the process plane closely represents the ODF in the material plane, it is established that the process under consideration is well-suited for achieving the desired set of properties. A possible process path to reach point A' is marked as $A - A'$ in the figure. Location of point A and the strains involved to reach A cannot be obtained in the context of the present analysis and need to be obtained by solving a separate optimization problem such as those presented in [60, 61, 62]. In such an optimization problem, strain rates of the sequence of processes identified from this analysis (rolling and tension) are incrementally varied from an initial guess so as to minimize the deviation from the optimum texture A' at the end of the process. The strain rates in the ensemble (that generated the basis functions for the process planes) are used as the initial guess. The optimization problem is considerably faster since it solves a reduced-order texture evolution problem at

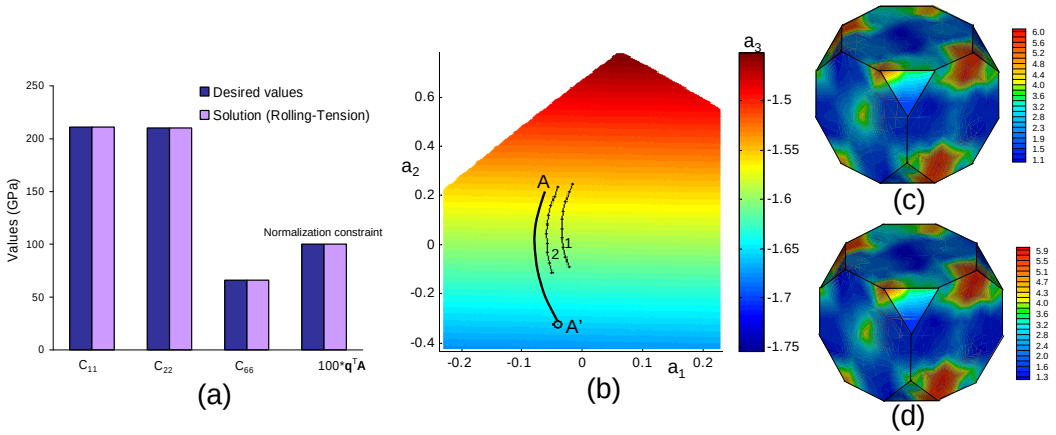

Figure 2.6: (a) Desired properties and the closest properties obtainable from the process plane. The last bar shows that the solution ODF is normalized. (b) The optimal point A' is indicated on the process plane along with a possible processing path A-A' leading to it. Processing paths 1, 2 for various different starting textures obtained from different levels of straining in the first (rolling) stage are also shown. (c) Reconstructed optimal ODF from the process plane. (d) Exact ODF that reproduces the desired property.

each iteration, utilizing the basis functions already calculated for each process [62]. In this problem, we started by assuming a process sequence that we wanted to work with and then checking whether it can achieve an optimal ODF. In general, this search is repeated over several process planes from a database until a viable solution is found.

2.3.3 Identification of ODFs (from a given process) to obtain properties closest to a desired set of properties

Similarly to the optimization problem described in Section 2.3.2 where process plane ODFs closest to optimal ODFs in the material plane were identified, another optimization problem can be posed where the objective is to identify ODFs in the

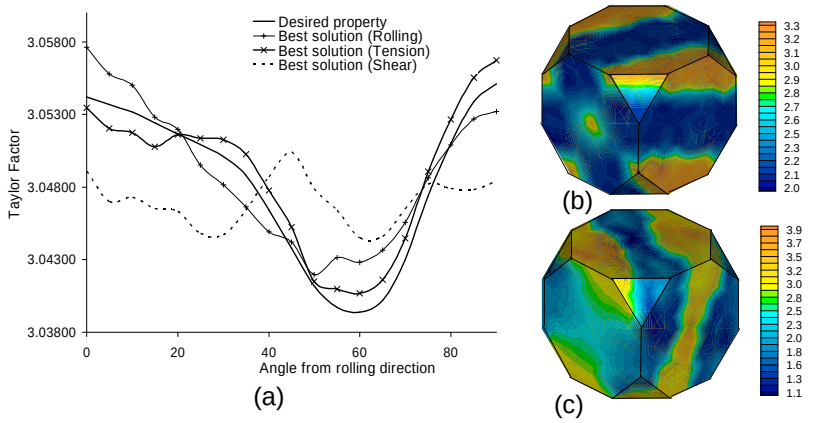

Figure 2.7: (a) For a desired property distribution shown, the closest property distributions obtainable in the x-axis tension, rolling and x-y shear process planes are shown. (b) The optimal solution ODF from tension process plane and (c) The optimal solution ODF identified in the rolling process plane.

process plane that closely reproduce a desired set of properties. The optimization problem in this case is posed so as to identify ODFs in the process plane whose properties are closest to a desired set of properties in some sense.

The objective is to minimize the bound ($e_0 \geq 0$) on the absolute value of error from a desired property: $\min_{\boldsymbol{a}} e_0$ such that $\sum_{m=1}^{b} \boldsymbol{p}^T \boldsymbol{\phi}_m a_m + \boldsymbol{p}^T \boldsymbol{e} = \boldsymbol{d}$, where $\boldsymbol{d}$ is the desired set of properties. The normalization constraint is given as $\sum_{m=1}^{b} \boldsymbol{q}^T \boldsymbol{\phi}_m a_m = 1$. Positivity of the ODF dictates the constraint $\sum_{m=1}^{b} \boldsymbol{\phi}_m a_m \geq 0$. Bound on the absolute value of error is defined as $|e_i| \leq e_0$. This is equivalent to pairs of linear inequalities: $-e_i - e_0 \leq 0$ and $e_i - e_0 \leq 0$, where $i = 1, \ldots, n_p$, where n_p denotes the number of properties to be optimized. This problem uses $\boldsymbol{x} = [e_1, \ldots, e_{n_p}, a_1, \ldots, a_b, e_0]^T$ as the variable to be identified. The error e_i is allowed to be of either sign.

As an example, for a desired variation of Taylor factor from the rolling to transverse direction shown in Fig. 2.7(a), the closest property distributions obtainable

from the x-axis tension, y-axis rolling and x-y shear process planes are shown. Basis functions for each process was computed from an ensemble of textures obtained by deforming an initial random texture to 0.1 strain with the respective process. As seen in Fig. 2.7(a), the optimal ODF obtained from the x-y shear process plane fails to reproduce the desired property distribution. The property distribution however is represented well by the optimal ODFs identified from the tension or rolling process planes which are shown in Fig. 2.7(b) and (c), respectively.

2.4 Identification of process paths and optimal ODFs from process-property spaces

Property closures similar to those constructed for the material plane (in Section 2.2.2) can be constructed for visualizing the range of properties obtainable from different process planes. They represent the set of all properties (for a given homogenization method) obtainable from ODFs represented by a process plane. The procedure to obtain extremum properties from the process plane is to pose the LP problem as: $\min_{\boldsymbol{a}} \boldsymbol{f}^T\boldsymbol{a}$ where $f_m = -\boldsymbol{p}^T\boldsymbol{\phi}_m$ for maximizing properties and $f_m = \boldsymbol{p}^T\boldsymbol{\phi}_m$ for minimizing properties, with $m = 1, \ldots, b$. The linear constraint is that the solution ODF is normalized to unity, $\boldsymbol{g}^T\boldsymbol{a} = 1$ where $g_m = \boldsymbol{q}^T\boldsymbol{\phi}_m, m = 1, \ldots, b$.

Positivity of the ODF dictates that $\sum_{m=1}^{b} \boldsymbol{\phi}_m a_m \geq 0$. The procedure for mapping the range of properties obtainable from a process plane is similar to that presented in Section 2.2.2. The nature of property-process space inherently allows development of several processing routes for obtaining a desired property. Processes can be associated with properties by superimposing the property closures

of process planes in the property space. As an example, Fig. 2.8 shows the property space of Taylor factors along the rolling and transverse directions. Property closures of four different process planes are superimposed in this property space. Process plane for x-axis tension was constructed using basis functions calculated from an ensemble of textures obtained by deforming a random starting texture (R) to a strain of 0.1. Properties for this ensemble fall along path R-e in the figure. Process plane for y-axis rolling was constructed using basis functions calculated from an ensemble of textures obtained by deforming random texture (R) to a strain of 0.2. Properties for this ensemble fall along path R-d in the figure. Third process plane was constructed using basis functions calculated from an ensemble of textures obtained by y-axis rolling of a random texture up to strain of 0.1 (corresponding to point a) as the starting texture which is processed to an additional 0.1 strain under x-axis tension to end point b. Properties for this ensemble fall along path a-b in the figure. Fourth process plane is constructed using basis functions calculated from an ensemble of textures obtained from z-axis rolling of texture at point b to an additional strain of 0.1. Properties for this ensemble fall along path b-f in the figure. Now, to tailor properties of a random texture (point R - (3.067,3.067)) and reach desired property (point C - (3.077,3.084)), two different process paths can be graphically seen. Simplest route is a direct tension process (path $R - C$). However, route $R - a - b - C$ is also possible for reaching the desired property. The presence of such a route could have been inferred from the superimposed property closures of process planes shown in Fig. 2.8 since desired property point C lies on the fourth process plane which involves a process path of the type $R - a - b - C$.

In association with databases of process planes, such a methodology would be able to identify several process sequences that might lead to a desired property

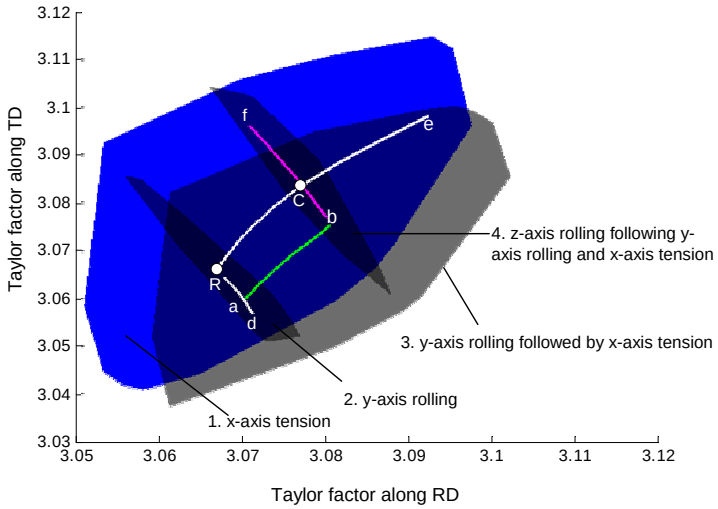

Figure 2.8: Property closures of different process planes plotted in the property space for designing process sequences. Two different routes to reach a desired property C from a random ODF (represented at R) are shown. Route R-C follows a x-axis tension process and route R-a-b-C follows a process sequence of y-axis rolling, x-axis tension followed by z-axis rolling.

point C starting from a random texture. Once process sequences are identified, the exact process parameters (locations of point 'a' and 'b') can be found by existing gradient optimization algorithms such as in [60, 61, 62] as explained in Section 2.3.2. To retrieve the optimal ODF (at point C) for the tension process, the property iso-lines of Taylor factor in rolling and transverse direction corresponding to point C are drawn on the property contours of tension process plane as shown in Figs. 2.9(b) and (c), respectively. The intersection point of the iso-property lines in Figs. 2.9(b,c) gives the desired ODF as shown in Fig. 2.9(d). The graphical solution described here is useful for optimizing up to three properties, which allows visualization of the space. In other cases, where a large number of properties (or a property distribution) need to be optimized, the first step of identifying best processing route needs to be replaced with a linear programming problem of the type used for obtaining desired properties in Fig. 2.6 or Fig. 2.7.

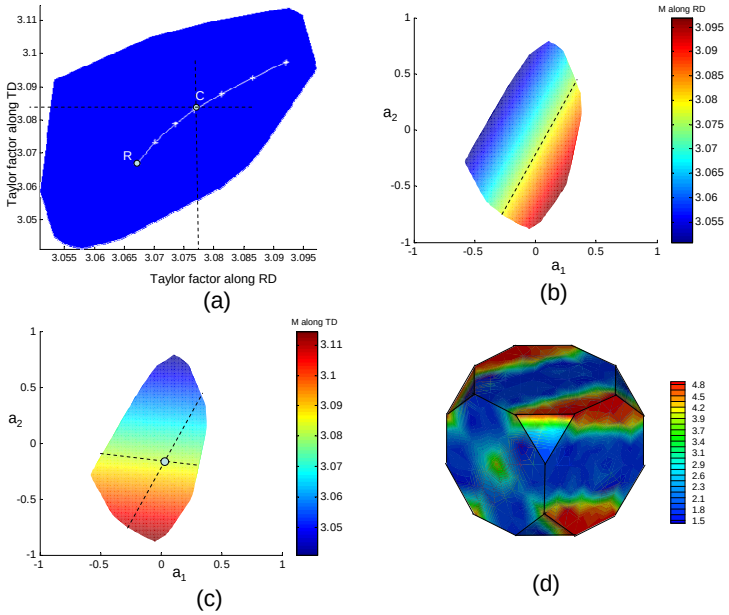

Figure 2.9: (a) Shows property closure for x-axis tension process with a path leading from property R to C. The ODF corresponding to optimal property C needs to be identified. This is identified from the point of intersection of property iso-lines from the structure-property space shown in (b) and (c). The intersection point of the isolines in plots (b) and (c) gives the desired ODF as shown in (d).

2.4.1 Identification of ODFs with desired non-linear properties

Properties presented until now were linear in the ODF represented by the relationship $< \chi >= \boldsymbol{p}^T \boldsymbol{A}$. In the space of coefficients of basis functions for a process, iso-property surfaces for linear properties are represented as a family of parallel planes given by $\boldsymbol{p}^T \sum_{m=1}^{3} \boldsymbol{\phi}_m a_m =< \chi >$. Iso-property surfaces for non-linear properties are represented by a non-linear equation of the form $< \chi >= f(a_1, a_2, a_3)$ in the $\{a_1, a_2, a_3\}$ space. Fig. 2.10(b), for example, represents the iso-property surface for a non-linear property, the Lankford R-parameter, in the space of reduced-order

coefficients of basis functions in a x-axis tension process.

Method of computing the R-parameter is presented in [60]. The basis functions were constructed from an ensemble of textures obtained from processing a random texture to 0.1 strain under x-axis tension. The solution to $R = f(a_1, a_2, a_3) = 1.023$ at 45 degrees to the rolling direction corresponds to two surfaces out of which only one intersects the process plane. Points lying along the curve of intersection of iso-property surface and the process plane represent valid ODFs in the $\{a_1, a_2, a_3\}$ space with $R = 1.023$.

Similar surfaces of the Young's modulus along the rolling direction are plotted in Fig. 2.10(a). The Youngs Modulus along the RD is calculated by first inverting the average stiffness matrix found using the approach in Section 2.2.1 to obtain the average compliance matrix ($< \boldsymbol{S} >$). Young's modulus is then represented as $E = \frac{1}{<\boldsymbol{S}>_{11}}$. The solution of $E = 143.5GPa$ corresponds to 6 surfaces out of which only one intersects the process plane. In both Fig. 2.10(a) and Fig. 2.10(b), the process planes are colored according to the value of the non-linear property at each point. It is interesting to note that the property iso-surface intersecting the process plane is planar in both cases suggesting that the property may be represented in a linear basis of coefficients as $f(a_1, a_2, a_3) = \sum_{m=1}^{3} \boldsymbol{p}_m^{*\,T} a_m =< \chi >$ and similar linear programming methodologies as before may be used to invert the property-ODF relationship.

2.5 Conclusions

Developments presented here advance materials-by-design for polycrystalline materials through the following new contributions:

- Concept of 'material plane' in Rodrigues space was employed to construct linear programming solutions to several problems including identification of optimal or extremal ODFs and construction of property closures for given linear homogenization relations.
- A new concept of 'process plane' was established that represents the space of reduced-order coefficients for a given process. The process plane is capable of extrapolating several different processing paths.
- Linear programming methods were constructed to solve problems involving identification of ODFs on the process plane that are as close as possible to desired ODFs on the 'material plane'.
- Graphical solution to the process sequence selection problem was enabled through identification of process paths on property spaces that represent ranges of properties represented by a process plane.

Selection of optimal textures and processing paths is enabled using databases of reduced-order basis functions and the optimization techniques described in this chapter. The error in reconstruction of process paths increases gradually with increase in extrapolation. This means that processing paths for some parts of the process plane cannot be established accurately. The optimization methodology at present is for linear properties, although studies indicate that iso-property curves of non-linear properties such as the Lankford R-parameter are almost linear in the process plane. This suggests the possibility that these properties may be approximated in a linear basis of reduced coefficients. In order to extend the optimization strategy for identifying microstructures with desired non-linear properties, we resort to gradient optimization approaches. Taking advantage of the model reduction methodology presented in this chapter, we present an adaptive optimization

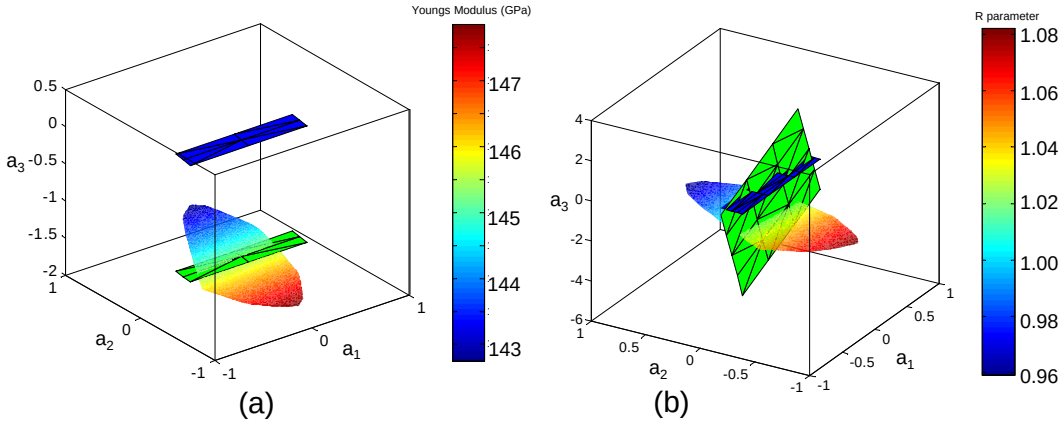

Figure 2.10: ODFs with a desired non-linear property lie on the curve of intersection of iso-property surfaces (for the desired property) with the process plane. Figure shows iso-property surfaces for (a) Youngs Modulus = 143.5 GPa and (b) Lankford R-parameter = 1.023. There are several iso-surfaces in the space of basis coefficients $\{a_1, a_2, a_3\}$ for these two cases although only one such surface intersects the process plane for x-axis tension.

methodology that allows optimization of a variety of texture-dependent properties and identification of processing paths to reach these properties in the next chapter.

Chapter 3

On the synergy between microstructure classification and deformation process sequence selection for the control of material properties

[2] The previous chapter presented the model reduction methodology for textures and a novel graphical representation scheme for identifying processing paths that lead to desired properties. This section details the methodology required to identify the process parameters in such optimal processing paths using gradient optimization. In particular, classification of F.C.C. polycrystal texture is used as a scheme to adaptively select reduced order models for each iteration of the gradient optimization scheme. Given a desired ODF, a hierarchical classifier matches its ODF features in the form of pole density functions of important orientation fibers to a class of textures in the database. Texture classes are affiliated with processing information, hence, enabling identification of multiple process paths that lead to a desired texture. The process parameters identified by the classifier are fine-tuned using a gradient optimization algorithm driven by sensitivity analysis of texture evolution. An adaptive reduced-order model for texture evolution based on proper orthogonal decomposition is employed in which the reduced ODF modes corresponding to the intermediate stages of the design process are adaptively selected from the database.

[2] Reprinted from V. Sundararaghavan and N. Zabaras, "On the synergy between classification of textures and deformation process sequence selection", Acta Materialia, Vol. 53/4, pp. 1015-1027, 2005.

In section 3.1, the representation of F.C.C. texture in Rodrigues space is defined followed by introduction to the concept of orientation fibers. In section 3.2, we introduce our classification framework. In section 3.3, a texture evolution model based on reduced representation of texture is discussed followed by the process design methodology in section 3.4. In section 3.5 we present relevant applications of the methodology.

3.1 Texture representation and feature extraction

Orientation distribution function (ODF) [27, 25], the probability density function for orientations, is employed for the quantification of crystallographic texture. Various methods are available for computing ODF evolution (see [77]) during deformation processing. Texture evolution methodologies use parameterizations for the crystal lattice rotation which together with the crystal symmetry define the problem domain. We employ the Rodrigues-Frank axis-angle parametrization of the orientation space. This is based on the unique association of an orientation with a rotation axis, and an angle of rotation about the axis.

3.1.1 Representation of FCC texture in Rodrigues space

The Rodrigues' parametrization is created by scaling the axis of rotation as $\mathbf{r} = \mathbf{n}tan(\frac{\theta}{2})$. A proper rotation $\mathbf{R}$ relates the lattice orientation to a reference orientation. Given the Rodrigues parametrization $\mathbf{r}$, the rotation $\mathbf{R}$ can be obtained as,

$$\mathbf{R} = \frac{1}{1 + \mathbf{r}.\mathbf{r}}(\mathbf{I}(1 - \mathbf{r}.\mathbf{r}) + 2(\mathbf{r} \otimes \mathbf{r} + \mathbf{I} \times \mathbf{r})). \tag{3.1}$$

The fundamental region represents a region of the orientation space such that each crystal orientation is represented uniquely within the space. Fundamental region for the cubic symmetry group results in a truncated cube. The planes that form the faces of the cube are introduced by symmetry rotations about $\langle 100 \rangle$ family of axes and the corners are truncated by planes introduced by rotations about the $\langle 111 \rangle$ axes. The ODF (represented by $\mathcal{A}$) describes the local density of crystals over this fundamental region of orientation space. The volume fraction of crystals within a part ($\Re^*$) of the fundamental region is given by $v_f(\Re^*) = \int_{\Re^*} \mathcal{A} dv$.

3.1.2 Classification for identifying processes that lead to desired ODF

ODF classification framework creates a self-organizing database of textures from which relationships between processes and textures can be identified. The task of the classifier is to identify a class of textures (and associated process parameters) that may result in a desired ODF. Apart from using numerical control algorithms, the underlying inverse problem can also be approached using pattern recognition approaches over large and comprehensive databases. Direct classification of the ODFs using the finite element representation (the nodal values) over such databases are not computationally feasible due to high-dimensionality of the data set. We employ the approach in [78, 134] where classification is carried out over a hierarchy of classes using lower-order microstructural features. The lower order features for the ODF is realized in the form of pole-density functions of important orientation fibers in the fundamental region and are used to create the class hierarchy. These features are extracted from a given desired ODF and pattern recognition is employed to propagate the information over the existing class

hierarchy to identify the required texture class (and process parameters). The significance of the lower order features employed is briefly explained in the following sub-section.

Orientation Fibers

A $\langle \mathbf{h} \rangle$ fiber about sample axis $\mathbf{y}$ connects orientations that align the crystal $\mathbf{h}$ axis with the sample $\mathbf{y}$ direction. The rotation $\mathbf{R}$ required to align $\mathbf{h}$ with $\mathbf{y}$ is based on a rotation of $\mathbf{h}$ through an angle $\phi = \cos^{-1}\mathbf{h} \cdot \mathbf{y}$ about axis $\mathbf{h} \times \mathbf{y}$. Note that $\mathbf{h}$ and $\mathbf{y}$ remain aligned even if the orientations change due to rotations about $\mathbf{h}$ or $\mathbf{y}$ axis. These orientations define the orientation fiber. In the Euler angle space, the fibers are curves described by trigonometric functions. Orientation fibers reduce to straight lines over Rodrigues' space. The orientations along the fiber over Rodrigues space is obtained by varying the parameter λ in the following equation,

$$\mathbf{r} = \frac{1}{1 + \mathbf{h}.\mathbf{y}}(\mathbf{h} \times \mathbf{y} + \lambda(\mathbf{h} + \mathbf{y})) \tag{3.2}$$

Here, $\lambda = \tan(\phi + \bar{\phi})/2$ where ϕ and $\bar{\phi}$ are arbitrary, corresponding to rotations about $\mathbf{h}$ and $\mathbf{y}$, respectively. Fiber textures develop as flow of crystals over the space of orientations are channeled along particular orientation fibers. Certain families of fibers are of particular importance in F.C.C textures. For example, the $\langle 110 \rangle$ family of fibers appear under uniaxial compression, plane strain compression and simple shear. FCC metals are typically associated with texturing to $\langle 111 \rangle$ and $\langle 100 \rangle$ fibers under tension and $\langle 110 \rangle$ under compression. In torsion tests, the z-axis $\langle 111 \rangle$ fibers and x-axis $\langle 110 \rangle$ are seen to predominate. The texturing of FCC

metals under plane strain compression is dominated by the α fiber (ND $\langle 110 \rangle$) connecting the ideal Goss and brass orientations, and the β fiber connecting the brass, S, and copper orientations ([30]).

For a particular $\mathbf{h}$, the pole figure takes values $\mathcal{P}(\mathbf{h}, \mathbf{y})$ at locations $\mathbf{y}$ on an unit sphere. The pole density function, $\mathcal{P}(\mathbf{h}, \mathbf{y})$ gets contributions from orientations for which the mapping $\mathbf{R}$ brings $\pm\mathbf{h}$ (or symmetric equivalent) into alignment with the sample axis($\mathbf{y}$) as, $\mathbf{R} \cdot \mathbf{h} = \hat{\mathbf{h}}, \hat{\mathbf{h}} \parallel \mathbf{y}$. Using the crystal symmetries in the ODF, the expression for pole density function can be obtained as [66],

$$\mathcal{P}(\mathbf{h}, \mathbf{y}) = \frac{1}{2}[\mathcal{P}^0(\mathbf{h}, \mathbf{y}) + \mathcal{P}^0(-\mathbf{h}, \mathbf{y})] \tag{3.3}$$

where, $\mathcal{P}^0(\mathbf{h}, \mathbf{y})$ represents a path integral given as,

$$\mathcal{P}^0(\mathbf{h}, \mathbf{y}) = \frac{1}{2\pi} \int_{\hat{\mathbf{h}} \parallel \mathbf{y}} \mathcal{A} d\theta \tag{3.4}$$

The integration is performed over all the fibers in the fundamental region corresponding to crystal direction $\mathbf{h}$ and sample direction $\mathbf{y}$. Given the finite element discretization of the fundamental region, integration is done by tracking the fiber through each finite element. Within a finite element, $\mathcal{A}$ is interpolated using the element shape functions and the nodal point values associated with the element. The vector of all independent nodal values is represented by A^{np}. Pole density function ($\mathcal{P}(\mathbf{h}, \mathbf{y})$) of an orientation fiber family ($\mathbf{h}$) is found over a sample direction ($\mathbf{y}$) using a system vector ($m(\mathbf{h}, \mathbf{y})$, computed using Eq. 3.3,3.4 through a vector dot product as,

$$\mathcal{P}(\mathbf{h}, \mathbf{y}) = m(\mathbf{h}, \mathbf{y})^T A^{np} \tag{3.5}$$

The feature vector ($\mathbf{x}_i^l$) for the i^{th} ODF in the database at level l in the classification scheme is found as follows. The level l is associated with a particular fiber family ($\mathbf{h}$) and the pole density functions are calculated at various values

of $\mathbf{y} = [\mathbf{y}_1, \mathbf{y}_2, ..., \mathbf{y}_m]$ as, $\mathbf{x}_i^l = \mathbf{M}A_i^{np}$ where the system matrix ($\mathbf{M}$) is formed as
$\mathbf{M} = [m(\mathbf{h}, \mathbf{y}_1)^T;$
$m(\mathbf{h}, \mathbf{y}_2)^T; ...; m(\mathbf{h}, \mathbf{y}_m)^T]$.

The system matrix is calculated and stored beforehand for the fiber families used for classification. Fig. 3.1 shows the classification scheme for textures based on Pole density functions as lower-order features at various levels. An advantage of the clustering scheme is its ability to capture non-uniqueness in the process-design solutions. Through classification, identification of several processing paths that can lead to the desired texture is made possible.

Classifier Model The unsupervised classification problem aims to unearth the relationships between a set of data without the need for any user-defined data in the form of class labels. Given a data-set (D) consisting of n features of the ODF, $\mathbf{x}_i$, $i = 1, ..., n$, with each feature attribute being a vector of m values as $\mathbf{x}_i^T = \{x_{1i}, ..., x_{mi}\}, \mathbf{x}_i \in \Re^m$. The unsupervised classification problem is posed as follows:

Find the cluster centers $\{\boldsymbol{C}^1, \boldsymbol{C}^2, \ldots, \boldsymbol{C}^k\}$ *in* $\Re^m$ *such that the sum of the 2-norm distance squared between each feature* $\boldsymbol{x}_i$ *and its nearest cluster center* $\boldsymbol{C}^h$ *is minimized.*

The clustering problem can be written using the above mentioned 'distortion measure' as the problem of finding the cluster centers $\{\mathbf{C}^1, \mathbf{C}^2, \ldots, \mathbf{C}^k\}$ so that the cost function (J) is minimized,

$$J(\mathbf{C}^1, \ldots, \mathbf{C}^k) = \sum_{i=1}^{n} min_{h=1,...,k}(\frac{1}{2}\|\mathbf{x}_i - \mathbf{C}^h\|_2^2) \tag{3.6}$$

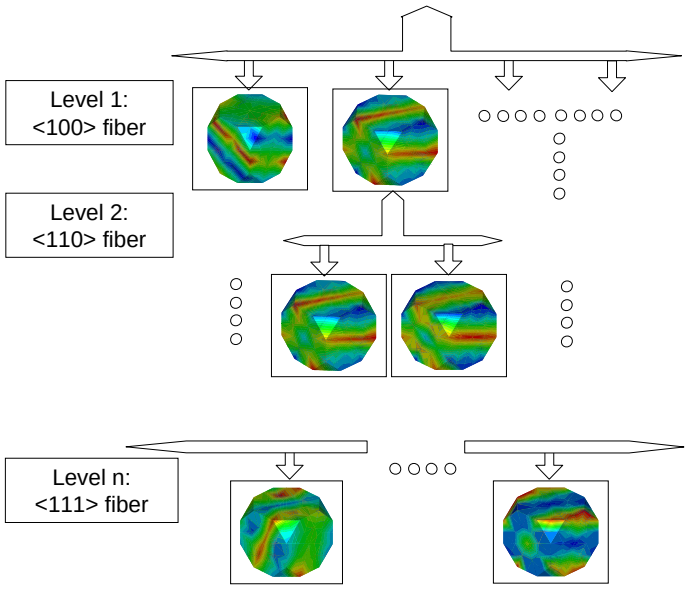

Figure 3.1: The classification hierarchy for ODFs. The feature vector contains the pole density functions at different sample directions for the family of fibers specified at each classification level.

3.2 K-Means Clustering Algorithm

The cluster center ($\mathbf{C}^i$) needs to be the centroid of the closest set of features ($\mathbf{x}_i$) for the distortion to be the minimum. Given a database D of n points in $\Re^m$ and cluster centers $\{\mathbf{C}^{1,i}, \mathbf{C}^{2,i}, \ldots,$
$\mathbf{C}^{k,i}\}$ in $\Re^m$ at iteration i, the Lloyd's algorithm computes the cluster centers, $\{\mathbf{C}^{1,i+1}, \ldots, \mathbf{C}^{k,i+1}\}$ at iteration $i+1$ in the following 2 steps: *1. Cluster Assignment*: For each data $\mathbf{x}_i$, assign $\mathbf{x}_i$ to cluster $h(i)$ such that center $\mathbf{C}^{h(i),i}$ is nearest to $\mathbf{x}_i$ in the 2-norm. *2. Cluster Update*: Compute $\mathbf{C}^{h(i),i+1}$ as the centroid of all points assigned to cluster h.

The algorithm is stopped when $\mathbf{C}^{h,i+1} = \mathbf{C}^{h,i}, h = 1, \ldots, k$, otherwise i is incremented by 1 and steps 1 and 2 are repeated. At the start of the algorithm, the k cluster centers, $\{\mathbf{C}^{1,0}, \mathbf{C}^{2,0}, \ldots, \mathbf{C}^{k,0}\}$ are randomly initialized. The cluster center

solutions produced depend on these initial values, and bad initial guesses may result in suboptimal partitioning. The standard solution is to try several starting configurations. The results of the k-means algorithm depends on the number of clusters (k) required to be provided by the user. For the ODF classification problem, the number of classes are not known a-priori. We employ the 'x-means' algorithm [79] for discovering the actual number of classes that exist in the set of ODFs. The Schwarz criterion, based on the Bayesian information criterion is employed in the x-means algorithm to estimate the actual number of clusters in the data-set. Given the data-set (D), the model chosen maximizes the Bayesian information criterion (BIC) given as,

$$BIC = \hat{l}(D) - \frac{p}{2} log(n) \tag{3.7}$$

where, $\hat{l}(D)$ is the log-likelihood of the data taken at the maximum likelihood point, p is the number of free parameters in the model, $p = m.k + k - 1 + k$, consisting of $m.k$ cluster center coordinates, $k - 1$ class probabilities and k variance estimates. The maximum likelihood estimate for the variance, assuming spherical-Gaussian distribution of data within a cluster (i) consisting of r_i data points ($\mathbf{x}_j^i, j = 1, \ldots, r_i$) is given as,

$$\hat{\sigma}_i^2 = \frac{1}{r_i - 1} \sum_{j=1}^{r_i} \|\mathbf{x}_j^i - \mathbf{C}^i\|^2 \tag{3.8}$$

The probabilities of each point within the cluster (i) is given as,

$$\hat{P}(\mathbf{x}_j^i) = \frac{r_i}{n} \frac{1}{\sqrt{2\pi}\hat{\sigma}_i{}^m} \exp(-\frac{1}{2\hat{\sigma}_i{}^2} \|\mathbf{x}_j^i - \mathbf{C}^i\|^2) \tag{3.9}$$

The log-likelihood of all the data within the cluster is given as,

$$\begin{aligned} l(D_i) &= \log \prod_{j=1}^{r_i} P(\mathbf{x}_j^i) \\ &= \sum_{j=1}^{r_i} (\log(\frac{1}{\sqrt{2\pi}\hat{\sigma}_i{}^m}) - \frac{1}{2\sigma_i^2} \|\mathbf{x}_j^i - \mathbf{C}^i\|^2 + \log \frac{r_i}{n}) \end{aligned} \tag{3.10}$$

Hence, at the maximum likelihood estimate, the log-likelihood of the data belonging to cluster i is given as,

$$\hat{l}(D_i) = -\frac{r_i}{2} log(2\pi) - \frac{r_i.m}{2} \log(\hat{\sigma_i}^2) - \frac{r_i - 1}{2} + r_i \log(r_i) - r_i \log(n) \tag{3.11}$$

The log-likelihood of the entire data set is the sum of the log-likelihoods of all clusters, hence, the BIC (Eq. 3.7) for the entire data-set can be written as,

$$BIC = -\frac{n}{2} log(2\pi) - \frac{m}{2} \sum_{i=1}^{k} r_i \log(\hat{\sigma_i}^2) - \frac{n-k}{2} + \sum_{i=1}^{k} r_i \log(r_i) - n \log(n) - \frac{(m+2)k - 1}{2} log(n) \tag{3.12}$$

In the x-means algorithm, the Schwarz criterion is tested for configurations arising from different values of k, and the best configuration is chosen. Convergence properties are further improved in the algorithm by letting few cluster centers (parent clusters) obtained from the k-means step to split further into two centers. This is performed through local k-means operation on the parent cluster using two new centers. The Schwarz criterion is then tested locally within the parent cluster. The parent cluster is retained only if the BIC degrades due to the splitting operation. Fig. 3.2 shows a comparison of the x-means and the k-means methodologies for a two-dimensional feature set. Fig. 3.2(a) shows a configuration produced by the k-means algorithm with the number of classes (k) is given as 4. The configuration has converged but has not produced the distortion corresponding to the global minimum. Fig. 3.2(b) shows the k-means results with number of classes

(a) (b) (c)

Figure 3.2: Results of the x-means and k-means algorithm on a 2D feature set. The squares represent the cluster centers (a) Clustering using k-means: local optimum produced by the k-means algorithm ($k = 4$) (b) Clustering using k-means with number of classes fixed at $k = 6$ (c) 4 clusters identified by the x-means algorithm

$k = 6$. With k-means, it is not possible to extract the true clustering in the data-set. Higher the number of classes, the lesser is the distortion but the possibility of overfitting the data increases. Fig. 3.2(c) shows the cluster centers identified by the x-means algorithm. Based on the Schwarz criterion, x-means identified the 4 natural clusters in the data-set.

3.3 Texture evolution model

The evolution of ODF is governed by the ODF conservation equation. The conventional Eulerian rate form of the conservation equation is given by [30]:

$$\frac{\partial \mathcal{A}(\mathbf{r},t)}{\partial t} + \bigtriangledown \mathcal{A}(\mathbf{r},t) \cdot \mathbf{v}(\mathbf{r},t) + \mathcal{A}(\mathbf{r},t) \bigtriangledown \cdot \mathbf{v}(\mathbf{r},t) \;=\; 0 \tag{3.13}$$

where $\mathbf{v}(\mathbf{r},t)$ is the Eulerian reorientation velocity. The polycrystal average of an orientation dependent property, $\chi(\mathbf{r},t)$, is determined using the Eulerian ODF by an integral over the fundamental region:

$$\langle \chi \rangle \;=\; \int_{\mathcal{R}} \chi(\mathbf{r},t)\; \mathcal{A}(\mathbf{r},t)\; dv \tag{3.14}$$

A desired property $\langle\Phi\rangle$ distribution at the material point can hence be obtained by controlling the ODF ($\mathcal{A}$). From Eq. 3.13, it is seen that the evolution of the ODF ($\mathcal{A}$) is controlled by the reorientation velocity $\mathbf{v}(\mathbf{r},t)$. Hence, desired property $\langle\Phi\rangle$ can be obtained through control of the macro-design variable, namely the velocity gradient, $\mathbf{L}$, which is linked with $\mathbf{v}(\mathbf{r},t)$ using the extended Taylor macro-micro linking hypothesis. The hypothesis assumes that each crystal experiences the corresponding macroscopic deformation identically and hence, equates the crystal velocity gradient and the macro velocity gradient ($\mathbf{L}$).

The reorientation velocity is then evaluated through crystal constitutive relations, which involve the crystal velocity gradient. The velocity gradient of a crystal with orientation, $\mathbf{r}$, yields the following form [30]:

$$\boldsymbol{L} \;=\; \boldsymbol{\Omega} \;+\; \boldsymbol{R}\sum_{\alpha}\dot{\gamma}^{\alpha}\bar{\boldsymbol{T}}^{\alpha}\boldsymbol{R}^{T} \tag{3.15}$$

where $\boldsymbol{\Omega}$ is the lattice spin, $\dot{\gamma}^{\alpha}$ is the shearing rate along the slip system α and $\bar{\boldsymbol{T}}^{\alpha}$ is the Schmid tensor for the slip system α, given by $(\bar{\boldsymbol{m}}^{\alpha} \otimes \bar{\boldsymbol{n}}^{\alpha})$, where $\bar{\boldsymbol{m}}^{\alpha}$ is the slip direction and $\bar{\boldsymbol{n}}^{\alpha}$ is the slip plane normal, both in the crystal lattice frame. The expressions for the spin and symmetric parts are obtained as shown below:

$$\boldsymbol{\Omega} \;=\; \boldsymbol{W} \;-\; \sum_{\alpha}\dot{\gamma}^{\alpha}\boldsymbol{R}\bar{\boldsymbol{Q}}^{\alpha}\boldsymbol{R}^{T} \tag{3.16}$$

$$\bar{\boldsymbol{D}} \;=\; \sum_{\alpha}\dot{\gamma}^{\alpha}\;\bar{\boldsymbol{P}}^{\alpha} \tag{3.17}$$

where $\bar{\boldsymbol{P}}^{\alpha}$ and $\bar{\boldsymbol{Q}}^{\alpha}$ are the symmetric and skew parts of the Schmid tensor respectively and $\bar{\boldsymbol{D}}$ is the macroscopic deformation rate expressed in the lattice frame through, $\bar{\boldsymbol{D}} \;=\; \boldsymbol{R}^{T}\boldsymbol{D}\boldsymbol{R}$. The shearing rate on slip systems is given by a power law and we further assume that all slip systems have identical hardness.

$$\dot{\gamma}^{\alpha} \;=\; \dot{\gamma}^{0}\left|\frac{\tau^{\alpha}}{s}\right|^{1/m} sign\left(\frac{\tau^{\alpha}}{s}\right) \tag{3.18}$$

where s is the slip system hardness, m is the strain rate sensitivity, $\dot{\gamma}^0$ is a reference rate of shearing and τ^α is the resolved shear stress on slip system α. Further, the resolved stress is related to the crystal Cauchy stress as

$$\tau^\alpha \;=\; \bar{\boldsymbol{\sigma}} \bullet \bar{\boldsymbol{P}}^\alpha \tag{3.19}$$

By solving the system of equations (3.17 $-$ 3.19), the crystal cauchy stress ($\bar{\boldsymbol{\sigma}}$) and the shear rate ($\dot{\gamma}^\alpha$) can be evaluated. Next, using Equation (3.16), we can evaluate the lattice spin vector as,

$$\omega \;=\; \text{vect}\,(\boldsymbol{\Omega}) \tag{3.20}$$

which is then used to evaluate the reorientation velocity as,

$$\mathbf{v} \;=\; \frac{1}{2}\,(\omega \;+\; (\omega \cdot \mathbf{r})\mathbf{r} \;+\; \omega \otimes \mathbf{r}) \tag{3.21}$$

Finally, the ODF, $\mathcal{A}$, over the current fundamental region $\mathcal{R}$ is evaluated from the Eulerian form (Equation (3.13)) of the conservation equation. The full and reduced order methodologies for solving the PDE (Equation (3.13)) is given in the next subsection.

3.3.1 Full and reduced order approaches

Eq. (3.13) has the form of the advective transport equation and is subject to discontinuities in the velocity divergence. The finite element formulation (full-order model) involves SUPG stabilization and takes the following form:

$$\int_{\mathcal{R}} \left\{ \frac{\partial \mathcal{A}}{\partial t} + \bigtriangledown \mathcal{A} \cdot v + \mathcal{A} \bigtriangledown \cdot v \right\} \; w \; dv \;+\; \int_{\mathcal{R}_t} \bigtriangledown \cdot (\epsilon \bigtriangledown \mathcal{A}) \; \psi \; dv = 0 \tag{3.22}$$

where w and ψ are the Petrov-Galerkin and classical Galerkin weighting functions respectively and ϵ is the shock capturing parameter.

In multi-scale deformation problems where several ODFs need to be controlled, the full-order model requires considerable computational resources due to large number of degrees-of-freedoms needed for the analysis as well as the associated mathematical and computational complexity. The proper orthogonal decomposition (POD) technique is popular reduced order modeling approach for decreasing the computational burden in such problems. Reduced-order modeling is based on the development of a reduced set of basis functions, $\phi(\mathbf{r})$, to represent the associated ODF. The method of snapshots is introduced for generating the basis. It assumes that the basis, ϕ, can be expressed as a linear combination of the N snapshots from direct simulation as:

$$\phi_j \;=\; \sum_{i=1}^{N} w_i^j \mathcal{A}^{(i)} \tag{3.23}$$

where w_i^j can be determined by the solving the eigenvalue problem:

$$\boldsymbol{C}\;\boldsymbol{W} \;=\; \boldsymbol{\Lambda}\;\boldsymbol{W} \tag{3.24}$$

where, $\boldsymbol{C}$ is the spatial correlation matrix defined as,

$$\boldsymbol{C}_{i,j} \;=\; \frac{1}{N}\int_{\mathcal{R}} \mathcal{A}^{(i)}(\mathbf{r})\;\mathcal{A}^{(j)}(\mathbf{r})\;dV \tag{3.25}$$

and $\boldsymbol{\Lambda}$ and $\boldsymbol{W}$ are the complete eigen- description of the system. Once the modes have been evaluated, Equation (3.23) is used to generate the basis for reduced-order modeling, such that at any processing stage j,

$$\mathcal{A}^{(j)}(\mathbf{r},t) \;=\; \sum_{i=1}^{M^{(j)}} a_i^{(j)}(t)\phi_i^{(j)}(\mathbf{r}) \tag{3.26}$$

where M^j is the number of modes used in stage j, and $a_i^{(j)}$ are the reduced order coefficients used for representing the ODFs in stage j. Using this approximation in the weak form of the ODF conservation equation results in the following ordinary differential equation (ODE):

$$\dot{a} \;=\; \mathcal{R}a \tag{3.27}$$

where,

$$\mathcal{R}_{i,j} = \int_{\mathcal{R}} (\bigtriangledown \phi_j \cdot \mathbf{v}\ \phi_i + \phi_j\ \phi_i\ \ \bigtriangledown \cdot \mathbf{v}) dv \tag{3.28}$$

Eq. 3.27 is solved over n timesteps (0 to t_n) at each stage. At any stage j, $j = 1, \ldots, p$, the initial value of a is given through the following equation,

$$a_i^{(j)}(0) \ = \ \int_{\mathcal{R}} \mathcal{A}^{(j-1)}(\mathbf{r}, t_n) \phi_i^{(j)}(\mathbf{r}) dv \tag{3.29}$$

where, $\phi^{(j)}(\mathbf{r})$ is the reduced basis at stage j. The initial microstructure is assumed to be random and taken as $\mathcal{A}^{(1)}(r, 0) \ = \ 2.435$. Equations (3.27) $-$ (3.29) define the reduced-order model for the ODF conservation equation. Thus, to obtain desired orientation distribution functions (e.g. desired texture and thus desired properties), one needs to only control a small finite number of degrees of freedom (i.e. the vector a).

3.4 Design of processes

The objective of the microstructure-sensitive design process is to control the properties in the micro-scale through design of appropriate deformation processes. The direct problem described in Section 3.3 simulates the ODF evolution given the macro velocity gradient. The process design methodology aims to identify the macro velocity gradient that yields a desired ODF (or desired property distribution). Given a good initial guess, gradient based methods converge to a local optimum within a few iterations and hold computational advantage over heuristic global solution search techniques. Intelligent choice of the initial guesses can be made using prior information available in the form of a database through clas-

sification. Refer [60, 61] for complete details on the implementation of the design problem for a single stage using gradient-based approach. The calculation of gradients in the optimization framework involves reduced-order modeling of the polycrystal continuum sensitivity equation and calculation of sensitivities of the reorientation velocity through the crystal plasticity relations by design differentiation of the linking hypothesis. The following section addresses the extension of the technique to a multi-stage design process.

3.4.1 Multi-stage design process

Let us consider Equation (3.13). We denote the sensitivity of the ODF to a small change in the process parameter ($\boldsymbol{\alpha}$) as $\overset{\circ}{\mathcal{A}} = \hat{\overset{\circ}{\mathcal{A}}}(r, t; \boldsymbol{\alpha}, \Delta\boldsymbol{\alpha})$. Taking the design differentiation of Equation (3.13) results in the following partial differential equation:

$$\frac{\partial \overset{\circ}{\mathcal{A}}}{\partial t} + \bigtriangledown \overset{\circ}{\mathcal{A}} \cdot v + \bigtriangledown \mathcal{A} \cdot \overset{\circ}{v} + \overset{\circ}{\mathcal{A}} \bigtriangledown \cdot v + \mathcal{A} \bigtriangledown \cdot \overset{\circ}{v} = 0 \tag{3.30}$$

The PDE can be solved to develop the sensitivity of the ODF field assuming that the sensitivity of the reorientation velocity and its divergence are known. This is evaluated in the constitutive sensitivity problem (Refer [60, 61]).

In this reduced-order model, we utilize the basis developed earlier for the direct problem and approximate the sensitivity fields as linear combinations of these basis functions. The computations are similar to those performed for the direct analysis, and the reduced system is obtained as follows:

$$\dot{b} = \mathcal{G} b + \mathcal{H} \tag{3.31}$$

where

$$\mathcal{G}_{i,j} = \int_{\mathcal{R}} (\bigtriangledown \phi_j \cdot v \ \phi_i \ + \ \phi_j \ \phi_i \ \bigtriangledown \cdot v) dv \tag{3.32}$$

$$\mathcal{H}_i = - \int_{\mathcal{R}} (\bigtriangledown \mathcal{A} \cdot \overset{\circ}{v} \ \phi_i \ + \ \mathcal{A} \ \phi_i \ \bigtriangledown \cdot \overset{\circ}{v}) dv \tag{3.33}$$

For the first stage, $\overset{\circ}{\mathcal{A}}^{(1)}(r,0) = 0$. At the end of stage j, $\overset{\circ}{\mathcal{A}}^{(j)}(r,t_n)$ is calculated from the coefficients obtained from the solution of Eq. 3.31 at the final time step as,

$$\overset{\circ}{\mathcal{A}}^{(j)}(r,t_n) = \sum_{i=1}^{M^{(j)}} b_i^{(j)}(t_n)\phi_i^{(j)}(r) \tag{3.34}$$

where $\phi^{(j)}(r)$ the reduced basis at stage j. The initial value of b for $(j+1)$th stage is given through the following equation,

$$b_i^{(j+1)}(0) \ = \ \int_{\mathcal{R}} \overset{\circ}{\mathcal{A}}^{(j)}(r,t_n)\phi_i^{(j+1)} dv \tag{3.35}$$

where $\phi^{(j+1)}(r)$ is the set of reduced basis employed for the sensitivity problem at stage $j+1$. Once the sensitivity at the last time step of the final stage is found, the expectation of the sensitivity of a property to a small change in the process parameter is found as,

$$\langle \overset{\circ}{\chi} \rangle \ = \ \int_{\mathcal{R}} \chi(\mathbf{r},t) \ \ \overset{\circ}{\mathcal{A}}^{(p)}(\mathbf{r},t_n) \ dv \tag{3.36}$$

The design variable, namely the macro-velocity gradient (L) is decomposed uniquely as in Equation (3.37). Each matrix in the decomposition of Equation (3.37) corresponds to a given deformation process namely tension/compression (α_1), plane strain compression(α_2), shear modes($\alpha_3, \alpha_4, \alpha_5$) and rotation modes

$(\alpha_6, \alpha_7, \alpha_8)$.

$$\begin{aligned}
\mathbf{L} \;=\; & \alpha_1 \begin{bmatrix} 1 & 0 & 0 \\ 0 & -0.5 & 0 \\ 0 & 0 & -0.5 \end{bmatrix} + \alpha_2 \begin{bmatrix} 0 & 0 & 0 \\ 0 & 1 & 0 \\ 0 & 0 & -1 \end{bmatrix} + \alpha_3 \begin{bmatrix} 0 & 1 & 0 \\ 1 & 0 & 0 \\ 0 & 0 & 0 \end{bmatrix} \\
+ \quad & \alpha_4 \begin{bmatrix} 0 & 0 & 1 \\ 0 & 0 & 0 \\ 1 & 0 & 0 \end{bmatrix} + \alpha_5 \begin{bmatrix} 0 & 0 & 0 \\ 0 & 0 & 1 \\ 0 & 1 & 0 \end{bmatrix} + \alpha_6 \begin{bmatrix} 0 & -1 & 0 \\ 1 & 0 & 0 \\ 0 & 0 & 0 \end{bmatrix} \\
+ \quad & \alpha_7 \begin{bmatrix} 0 & 0 & -1 \\ 0 & 0 & 0 \\ 1 & 0 & 0 \end{bmatrix} + \alpha_8 \begin{bmatrix} 0 & 0 & 0 \\ 0 & 0 & -1 \\ 0 & 1 & 0 \end{bmatrix}
\end{aligned} \tag{3.37}$$

We define the design problem of interest as the selection of the processing sequence, with stages involving tension/compression, plane strain compression, shear or rotation, and the corresponding process parameters $\boldsymbol{\alpha}$ that lead to a desired property Ω that is a function of the ODF. This can be stated as follows:

$$\min_{\boldsymbol{\alpha}} \quad \mathcal{F}(\boldsymbol{\alpha}) \;=\; \frac{1}{N_s} \sum_{i=1}^{N_s} \left(\Omega^i \left(\mathcal{A}(\boldsymbol{\alpha})\right) - \Omega^{desired^i}\right)^2 \tag{3.38}$$

where N_s is the total number of sampling points, $\Omega^{desired}$ is the discrete representation of the desired microstructural property and $\boldsymbol{\alpha}$ is the design parameter involved in the iterative optimization algorithm corresponding to the process parameter (α_j) from stage $j = 1$ to p. The calculation of sensitivities of property χ to a component α_i of α require solution to sensitivity problems at $p - j + 1$ stages. The i^{th} multi-stage sensitivity problem is driven by $\Delta\alpha_i = 10^{-2}$ with $\Delta\alpha_j = 0$ for $j \neq i$. The gradients of property (χ) with respect to α_i is calculated as,

$$\frac{\partial \chi}{\partial \alpha_i} = \frac{\overset{\circ}{\chi}\left(\mathbf{r}, t, \alpha_1, .., \alpha_p, 0, .., \Delta\alpha_i, .., 0\right)}{\Delta\alpha_i} \tag{3.39}$$

The sensitivities are then used in a gradient descent algorithm to obtain the optimum process parameters that minimize the objective function in Eq. 3.38.

3.4.2 Adaptive reduced order model

The classification technique is database-driven and the availability of existing information can be further utilized to accelerate the texture evolution models. As discussed in [60, 61], the reduced order model needs to fully represent not only the optimal solution but also all the intermediate solutions during the optimization process. This calls for a method where the bases for the ODF are chosen adaptively during the control algorithm. We follow the method proposed by Ravindran([67]). At processing stage j, we begin optimization step 1 with reduced order modes ($\phi^{(j,1)}(\mathbf{r})$) obtained from the database corresponding to the initial process parameter estimate up to stage j, $\alpha^{(j,1)} = [\alpha^{(1,1)}$,
$..., \alpha^{(j,1)}]$ obtained through classification. This reduced-order model is now used in the gradient optimization algorithm to find the new iterate in the second optimization step, $\alpha^{(j,2)} = [\alpha^{(1,2)}$,
$.., \alpha^{(j,2)}]$. In general, the reduced order basis corresponding to a new iterate $\alpha^{(j,i+1)}$ at optimization step $(i+1)$ in stage j is found through the following steps:

1. Select the new reduced order basis ($\phi^{(j,i+1)}(\mathbf{r})$) from the existing database by searching for the closest parameter (β^D) within a user-defined tolerance limit,
$$\|\beta^D - \alpha^{(j,i+1)}\|_2 \leq \epsilon \tag{3.40}$$
2. If $\|\beta^D - \alpha^{(j,i+1)}\|_2 > \epsilon$, then compute the snapshots corresponding to $\alpha^{(j,i+1)}$, generate the new reduced basis ($\phi^{(j,i+1)}(\mathbf{r})$) from the snapshots and update the existing database with the new $\alpha^{(j,i+1)}$ and $\phi^{(j,i+1)}(\mathbf{r})$.

Remark 1: An initial uniform texture is assumed at the first processing stage. The reduced-order basis corresponding to the pure deformation modes (obtained

from an ensemble of data corresponding to a deformation $\alpha_i = 1$, if mode i is used in the first stage) is found to be sufficient to represent the texturing in the first stage.

Remark 2: The sensitivity problem uses the same basis as the direct problem. However, a sensitivity problem of stage i (where process variable corresponding to stage i is perturbed) uses the stage i basis for the sensitivity problems in stages $i+1$ to p.

Remark 3: Over large databases, the search procedure in step (1) of the adaptive reduced order algorithm can be addressed efficiently using classification algorithms.

3.4.3 Effect of adaptive basis threshold

The difference between the reduced and full order control solutions depend upon the sensitivity of the desired property to the numerical error induced by the introduction of reduced basis. Selection of the threshold parameter (ϵ) plays a critical role in the adaptive basis scheme described above. Small thresholds result in more accurate solutions but are computationally expensive due to frequent basis changes. Larger thresholds involve less frequent basis changes but may result in inaccurate solutions since the basis might not model the process employed accurately. Further, the sensitivities may be inaccurate leading to divergence in the objective function. Fig. 3.3 shows the increase in error caused with increasing values of ϵ used for the basis selected. The strain rate for the first stage is fixed and that of the second stage is increased which results in different values of ϵ. The ODF resulting from a basis with $\epsilon = 0$ after a time of 0.1 sec is used as the reference

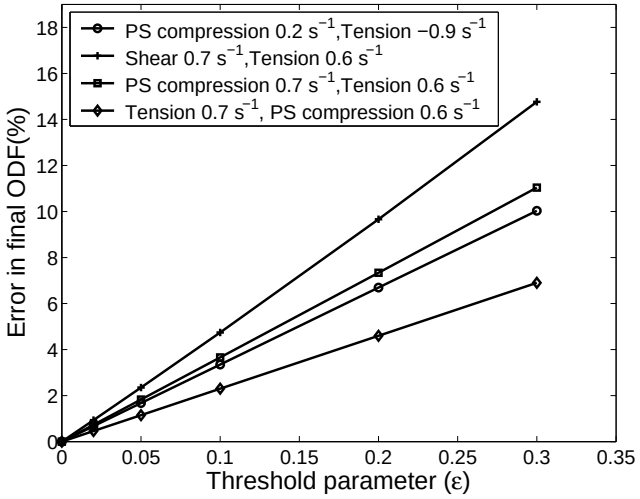

Figure 3.3: Error induced due to different thresholds for the basis, the error not only depends on the threshold but also on the sequence of processing stages involved.

($\mathcal{A}^{ref}$). The error is defined as $100 \times \frac{\|\mathcal{A}^{ref} - \mathcal{A})\|_2}{\|\mathcal{A}\|_2}$. The error not only depends on the threshold but also on the types of processing stages involved. With tension as the second processing stage, changing the first stage to shear from plane strain compression results in about 30 % increase in error at the same threshold. Within a processing sequence, however, the increase in error due to change in processing parameters is small. The results also indicate that the thresholds can be varied based on the processing sequence, a tension-plane strain compression processing sequence can have twice as much threshold than the shear-tension sequence with similar errors induced by the reduced order approximation.

3.4.4 Database architecture

The database contains several data sets, each set corresponding to a particular process sequence and associated processing parameters. Every data set also contains a reduced ODF basis for the process that it represents. The final ODF in

each data set is used in the classification scheme to identify classes of textures. The processing parameters that lead to a desired final texture is found by first identifying the class of texture to which the desired texture belongs. The required processing parameters and process sequences are then found from the data sets in the identified class. The best process path can then be selected from this set.

Let data set 'A' containing a processing sequence of tension and shear be found to result in a particular desired texture using the classifier. In a control problem involving the above 2 stages, a basis corresponding to the pure deformation mode (tension) is used for the first processing stage and is unchanged during the intermediate iterations of the control problem. For the second stage (shear), a basis of data set 'A' is initially used. If during an intermediate stage of the control problem, the process parameters for the tension and shear stages change beyond the allowed threshold (ϵ), then the database is initially searched for a data set with process parameters within the allowed threshold. If such a data set is not available, a new data set is added to the database corresponding to the new process parameters. The basis for this data set is used in subsequent iterations of the design problem until the process parameters once again change above the selected threshold. Using this scheme, just three modes of the basis (with three unknowns) are found to adequately represent the texturing at any stage in an optimization step, enhancing the computational efficiency of the algorithm. The success of the data-mining approach is limited to the amount of information in the database. Selection of good processing sequence solutions require a comprehensive database with data sets containing rich combination of processes. New information added to the database during the optimization process improves the possibility of identification of processing parameters and reduced basis functions directly from the database in future optimization runs.

3.5 Applications in materials design

A validation of the adaptive reduced order approach is provided together with relevant design problems utilizing the classification framework. F.C.C. materials with 12 slip systems are modeled in the examples. An initial uniform texture is assumed which corresponds to a value of $\mathcal{A}(r,0) = 2.435$. Relevant material constants used in the design examples are $\dot{\gamma}^{\alpha} = 1.0s^{-1}, m = 0.05$ and $s = 27.17MPa$ [30]. The reduced order basis for each design iteration is generated from an ensemble of data obtained from a deformation test for a time of $0.1s$ with a time step of $\delta t = 0.01s$. The first three modes of the selected reduced basis is used for modeling the texture evolution at any deformation stage. For the examples, the time for which each deformation stage acts is fixed at 0.1 s. The optimization problem is executed until the objective function normalized with the initial objective showed less than 10^{-4} improvement between iterations.

A study of the adaptive reduced basis algorithm is conducted comparing the reduced-order results with full-order approach. A 3 stage problem with each stage corresponding to a deformation test for a time of 0.1 s was carried out. The three stages employed are (1) Tension (Strain rate: $0.8s^{-1}$) (2) Plane strain compression (Strain rate: $0.2s^{-1}$) (3) Shear (Strain rate: $0.2s^{-1}$). The full model and the reduced-order ODF at the end of the three stages are shown alongside in Fig. 3.4. In Fig. 3.5, the final reduced-order sensitivity of the ODF with a perturbation of $0.01s^{-1}$ in the strain rate of the first stage is compared with the sensitivities obtained using (1) the full order sensitivity problem and (2) Finite difference method by perturbation of the full-order direct problem. The sensitivity of the first stage is transferred to the second stage and subsequently to the third stage. The basis of the first stage is utilized for all three stages for the sensitivity problem.

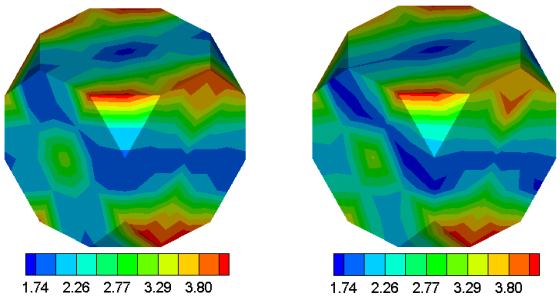

(a) (b)

Figure 3.4: Comparison of the ODF at the third and final stage obtained through (a) the full-order model, (b) the reduced-order model

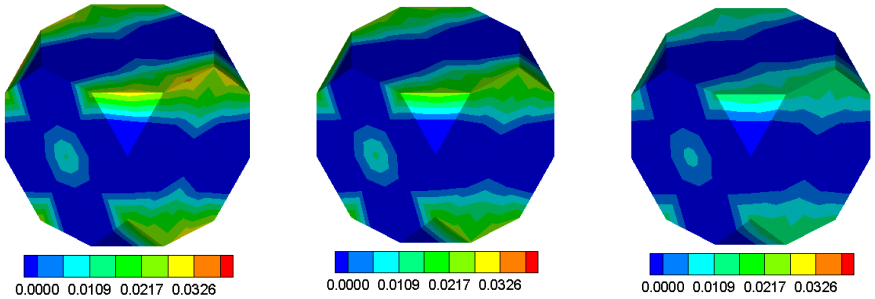

(a) (b) (c)

Figure 3.5: Comparison of the sensitivity of the ODF at the third and final stage due to perturbation in the process parameter (α) of the first stage obtained using (a) the full-order model, (b) the reduced-order model and (c) FDM solution at the final stage (t = 0.30 seconds)

3.5.1 Design for desired ODF

The optimization problem involves designing the macro velocity gradient to obtain desired orientation distribution function (ODFs). Given the initial processing sequence and the parameters identified by the classifier, the reduced-order optimization scheme identifies the processing parameters that lead to the desired texture. As an example, the desired ODF shown in Fig. 3.6(a) was initially identified to arise from a two-stage problem, with plane strain compression and

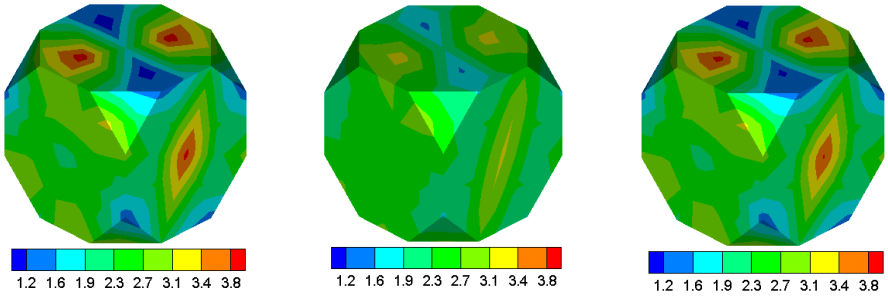

(a) (b) (c)

Figure 3.6: Control of material texture: (a) the desired texture, (b) the initial guess identified by the classifier and (c) reduced order optimized ODF

compression modes respectively by the classifier. The initial ODF corresponding to the strain rates for the two stages, 0.65 and $-0.1s^{-1}$ respectively is shown in Fig. 3.6(b). The strain rates for the two processes after the adaptive reduced order optimization procedure is obtained as 0.9472 and $-0.2847s^{-1}$ respectively and the optimized ODF is shown in Fig. 3.6 (c).

The advantage of the the data-mining methodology lies in the identification of multiple processing paths that lead to a desired texture. Fig. 3.7(b) shows a class of textures with different processing routes that can result in a desired ODF. Given the desired ODF, the classifier uses the lower order features, namely, the pole density functions, over 4 levels in the class hierarchy corresponding to the fibers in the $< 110 >, < 100 >, < 111 >$, and $< 211 >$ fiber families respectively. The orientation fibers are chosen based on their particular importance in FCC textures (see section 3.1.2) and their close affiliation with the processes involved. The desired texture in Fig. 3.7(a) is seen to be dominated by two fibers, the z-axis $< 110 >$ fiber and the alpha fiber (running from brass to the goss component) shown in Fig. 3.7(c). ODF intensities in the alpha fiber are associated with the process of plane strain compression, although the texture shows stronger development of

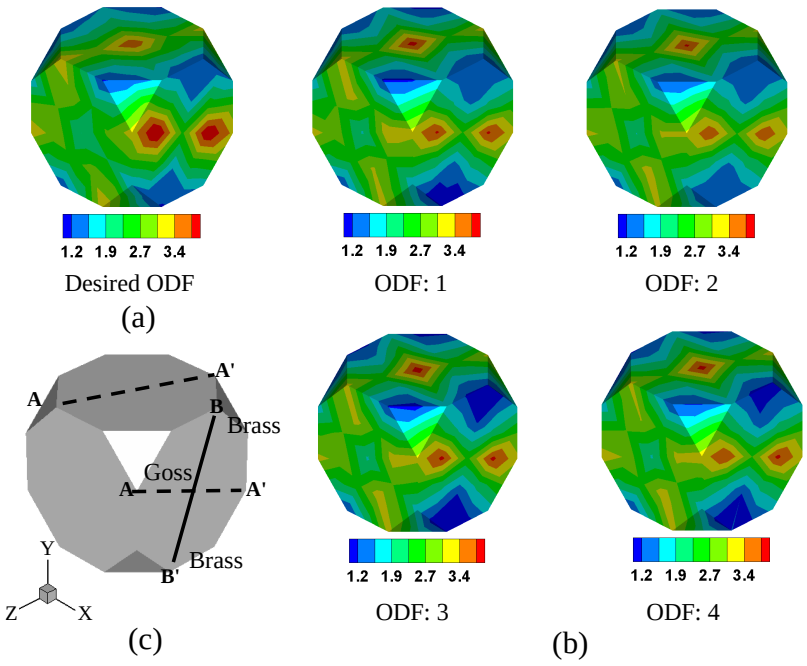

Figure 3.7: ODF:1,2,3,4 represent a class of ODFs similar to the desired ODF in their lower order features. Positions of z-axis $< 110 >$ (AA') and alpha fibers (BB') in the boundaries of the fundamental region are indicated in (c)

Table 3.1: Process parameters of the ODF class in Fig. 3.7.

ODF:	Stage 1	Stage 2	Stage 3
1	PSC $(-0.677s^{-1})$	Shear $(-0.165s^{-1})$	Tension $(-0.881s^{-1})$
2	Tension $(-0.835s^{-1})$	PSC $(-0.606s^{-1})$	
3	Tension $(-0.917s^{-1})$	Shear $(-0.074s^{-1})$	PSC $(-0.760s^{-1})$
4	Tension $(-0.907s^{-1})$	PSC $(-0.669s^{-1})$	Rotation $(0.179s^{-1})$

the brass component relative to Goss. Texturing to the z-axis $< 110 >$ fiber is normally associated with F.C.C. metals under compression along the z-axis. From the processing sequences identified (Table. 3.1), we see that these two processes are dominant in all the processing sequences found by the classifier.

3.5.2 Design for desired Elastic modulus

The data-mining methodology can be extended to classification of ODFs based on material property distribution exhibited by the ODF. Given a desired texture-dependent property, the classification is performed based on the property feature (variation of the property as a function of angle from the rolling direction) for the ODFs in the database. The clustering scheme enables identification of ODFs and the corresponding processes that can reproduce a desired property distribution.

This example demonstrates the control of the velocity gradient of a sequence of processes in order to obtain a particular distribution of the elastic modulus of an FCC Copper polycrystal about the normal direction away from the rolling direction. The stiffness in the crystal is given by the fourth tensor $\mathcal{C}_{ijkl}$ (values in GPa) in the crystal lattice frame for crystals with cubic symmetry as follows:

$$\boldsymbol{C} = \begin{bmatrix} 168.0 & 121.4 & 121.4 & 0 & 0 & 0 \\ 121.4 & 168.0 & 121.4 & 0 & 0 & 0 \\ 121.4 & 121.4 & 168.0 & 0 & 0 & 0 \\ 0 & 0 & 0 & 75.4 & 0 & 0 \\ 0 & 0 & 0 & 0 & 75.4 & 0 \\ 0 & 0 & 0 & 0 & 0 & 75.4 \end{bmatrix}$$

The polycrystal stiffness, $\bar{\boldsymbol{C}}$, is computed through a weighted average (over $\mathcal{A}$) of the stiffness of individual crystals expressed in the sample reference frame. The elastic modulus is then computed through this polycrystal stiffness as

$$\boldsymbol{E} = \frac{1.0}{\left(\bar{\boldsymbol{C}}\right)^{-1}_{(11)}} \tag{3.41}$$

Furthermore, the elastic modulus about an angle with the rolling direction (RD) can be evaluated using the above equation, but after a coordinate transformation

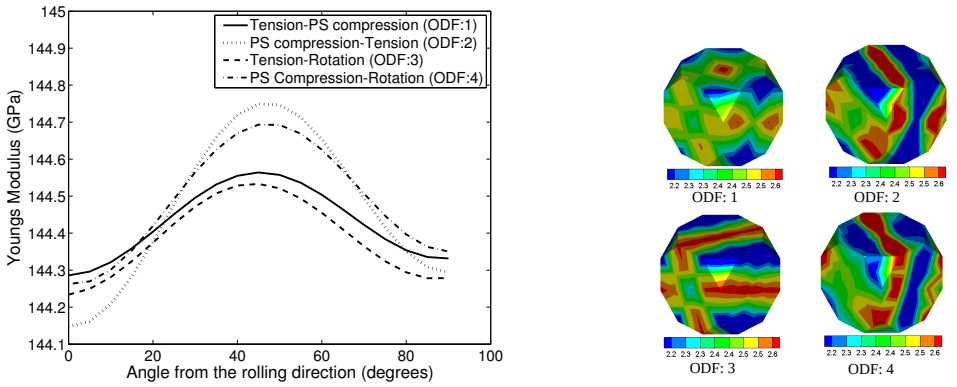

(a) (b)

Figure 3.8: (a) Classification based on property distribution: Young's modulus distribution of a class of ODFs (b) The corresponding ODFs.

of $\bar{\boldsymbol{C}}$.

The classification scheme captures the non-uniqueness in process design, identifying several different textures (and processes) that might result in a desired property distribution. An example of a class of ODFs obtained from the database based on the Youngs modulus property variation from rolling direction to the transverse direction in the sample is shown in Fig. 3.8 (b). The property distribution feature for a set of 4 ODFs within a class is shown in Fig. 3.8 (a). In contrast to the texture design problem, the property design problem clearly illustrates the presence of multiple solutions. A range of different processing sequences (indicated in Fig. 3.8(a)) yield similar distributions of the young's modulus. Thus, the methodology enables identification of new processes and selection of the economical process routes that leads to a desired property distribution based on available database of information.

To achieve a desired Young's modulus distribution as shown in Fig. 3.9 (a), we resort to the gradient based optimization scheme with the processing sequences found using the classifier as the initial guess. As an example, a processing sequence

of stage 1 of shear mode (mode 1) and stage 2 of tension mode is employed in the optimization procedure for achieving the desired property. A threshold of 0.05 is used for the selection of the adaptive basis. Using an initial guess -0.7 s^{-1} , and 0.15 s^{-1} for the strain rates as found from classification, the final optimized process parameters were obtained as -0.03579 s^{-1} and 0.17339 s^{-1} respectively. The elastic property distribution corresponding to the optimized process parameters identified are shown are shown along with the desired distribution in Fig. 3.9(a). The variation in the objective during the iteration process is shown in Fig. 3.9(b). The classification methodology is general and can be extended towards problems involving design of several other texture dependant properties through appropriate design of the processing sequence and process parameters.

3.6 Conclusions

The chapter presents a data-driven reduced order optimization procedure for the design of a process sequence to control the texture and texture-dependent properties. The inverse problem of identifying processes corresponding to desired texture is initially solved using the classifier algorithm over a database. The classifier matches the lower order features of the texture in the form of the pole density function over a class hierarchy to identify the sequence of processes that lead to the desired texture, hence, identifying multiple process paths that lead to the desired texture. These parameters are then fine tuned using gradient based optimization schemes. An unsupervised classifier based on the k-means algorithm is used for the identification of natural clusters within the database. The number of classes in the texture database is not known a-priori, hence, a Bayesian information criterion is used to identify the number of clusters.

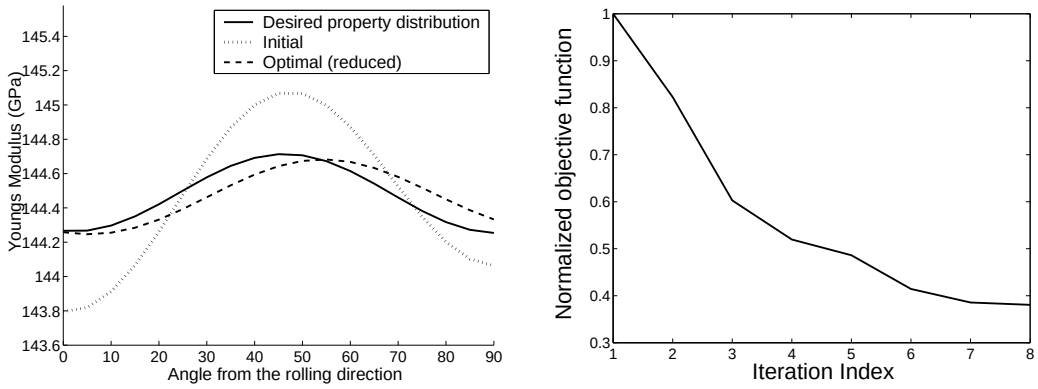

(a) (b)

Figure 3.9: Optimization of Youngs modulus distribution: (a) Comparison of the desired distribution and optimized distribution (b) Variation of the objective function with iterations

Compared to the full order optimal control approach, reduced-order control is computationally feasible and provides an efficient method for solving process design problems in reasonable time. The method of proper orthogonal decomposition provides a systematic way to obtain reduced-order models, however, the basis functions used for the control problem not only needs to represent the solution but also the textures arising from intermediate iterates of the design variable.

This chapter demonstrates a adaptive reduced-order model in which modes corresponding to the intermediate stages of the design process are adaptively selected from a database. Further, the database continuously improves during the optimization problems by addition of new, unknown data sets, which would be useful during future optimization runs. Evolution of properties during processing of materials depends not only on the texture as discussed in this chapter but also a variety of other features such as inter-granular misorientations and higher order correlations of crystal orientation. In the next chapter, a framework for extending the model to include additional microstructural features is presented.

Chapter 4

Development of multi-scale homogenization techniques

[2] Evolution of properties during processing of materials depends not only on the texture but also a variety of other features such as intergranular misorientation and higher order correlations of crystal orientation. A finite element homogenization approach is presented for calculating the evolution of macro-scale properties during processing of microstructures. This approach enhances the models presented in the previous chapters by incorporating effects such as misorientation and higher order correlations of crystal orientation, veritably increasing the range of properties that can be modelled. In addition, the method lends itself to subsequent development of multi-scale processing model. Macro-scale parameters such as forging rates can be linked with microstructure deformation using boundary conditions drawn from the theory of multi-scale homogenization. Homogenized stresses at the macro-scale are obtained through volume-averaging laws. A constitutive framework for thermo–elastic-viscoplastic response of single crystals is then utilized along with a fully-implicit Lagrangian finite element algorithm for modelling microstructure evolution. Development of texture and stress-strain response in 2D and 3D FCC Aluminum polycrystalline aggregates using the homogenization algorithm is compared with both Taylor-based simulations and published experimental results. In the next few sections, the microstructure interrogation technique used is introduced. Examples of homogenization and applications to design prob-

[3] Reproduced from V. Sundararaghavan and N. Zabaras, "Design of microstructure-sensitive properties in elasto-viscoplastic polycrystals using multi-scale homogenization", International Journal of Plasticity, Vol. 22, pp. 1799-1824, 2006.

lems of practical significance are then presented.

4.1 Microstructure interrogation

The approach adopted here for interrogation of microstructures involves finite element based elasto-visco-plastic analysis of microstructures using constitutive models based on the continuum slip theory. The overall response of the microstructure at the macro-scale is derived on the basis of homogenization. In this section, the microstructure interrogation and property evaluation scheme is systematically developed using the theory of non-linear homogenization. Let $\boldsymbol{y} : \mathcal{B}_{ref} \rightarrow \mathcal{B}$ represent the non-linear deformation map of the microstructure at time t, and $\boldsymbol{F} = \nabla_{ref}\boldsymbol{y}$ the associated tangent map (see Fig. 4.1). $\boldsymbol{F}$ maps points $\boldsymbol{Y} \in \mathcal{B}_{ref}$ onto points $\boldsymbol{y}(\boldsymbol{Y}, t)$ of the current configuration $\mathcal{B}$.

The reference microstructure configuration is considered of volume $V(\mathcal{B}_{ref})$ and boundary $\partial\mathcal{B}_{ref}$ with outward normal $\boldsymbol{N}$. The microstructure at time t of volume $V(\mathcal{B})$ and boundary $\partial\mathcal{B}$ with outward normal $\boldsymbol{n}$ is attached to the material point $\mathbf{X}$ in the macro-continuum (see Fig. 4.1). Further, we use superposed bars (e.g. $\bar{\boldsymbol{F}}$) to denote homogenized quantities and angular brackets (e.g. $\langle \boldsymbol{F} \rangle$) to denote volume-averaged quantities. In the subsequent analysis, the standard tensorial notation developed in [81] is followed. The most general assumption behind homogenization theory is that the deformation gradient as seen at the macro-scale can be represented purely in terms of the motion of the exterior boundary of the microstructure [36],

$$\bar{\boldsymbol{F}} = \frac{1}{V(\mathcal{B}_{ref})} \int_{\partial\mathcal{B}_{ref}} \boldsymbol{y} \otimes \boldsymbol{N} dA \tag{4.1}$$

The deformation of the microstructure is then related to the homogenized defor-

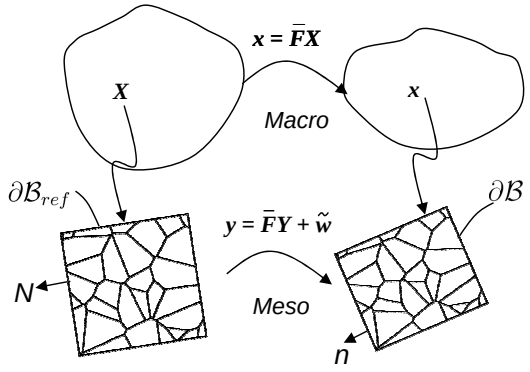

Figure 4.1: The microstructure homogenization technique: Each integration point in the macro-continuum is associated with an underlying microstructure. The microstructure reference configuration ($\mathcal{B}_{ref}$) and the mapping to the present microstructure configuration ($\mathcal{B}$) are shown in contrast with the homogenized macro-continuum.

mation gradient in the macro-continuum based on the assumption,

$$\mathbf{y} = \bar{\boldsymbol{F}}\mathbf{Y} + \tilde{\mathbf{w}} \tag{4.2}$$

where the deformation consists of a homogeneous part $\bar{\boldsymbol{F}}\boldsymbol{Y}$ and an inhomogeneous part $\tilde{\mathbf{w}}$ referred to as the fluctuation field. As a consequence, we have the relationship, $\boldsymbol{F} = \bar{\boldsymbol{F}} + \tilde{\boldsymbol{F}}$ (with $\tilde{\boldsymbol{F}} = \nabla\tilde{\mathbf{w}}$) between the microscopic ($\boldsymbol{F}$) and the macroscopic ($\bar{\boldsymbol{F}}$) deformation gradients. From the homogenization law (Eq. (4.1)) and the decomposition described above, it can be shown that the superposed field $\tilde{\mathbf{w}}$ follows the equation,

$$\frac{1}{V(\mathcal{B}_{ref})}\int_{\partial\mathcal{B}_{ref}} \tilde{\mathbf{w}} \otimes \boldsymbol{N} dA = 0 \tag{4.3}$$

The condition is satisfied by the use of any one of the three linking assumptions: (1) $\tilde{\mathbf{w}} = 0$ in $\mathcal{B}_{ref}$, (2) $\tilde{\mathbf{w}} = 0$ in $\partial\mathcal{B}_{ref}$, and (3) a periodic boundary condition (refer [53]) which is not dealt with in the present work. The first two multi-scale boundary conditions are popular in homogenization (i) based on Taylor hypothesis that all crystals deform identically ($\boldsymbol{F} = \bar{\boldsymbol{F}}$) and (ii) homogeneous deformation on the boundaries of the microstructure while allowing for non-uniform

deformations within the microstructure. The Taylor hypothesis poses a stringent kinematic constraint on the grains and thus provides a stiff response. In addition, as explained earlier, this assumption fails to model inter- and intra-granular mis-orientation development which is a key feature in polycrystalline materials. The second hypothesis, which allows for homogeneous deformations at the boundary of the microstructure (referred to as the *HB* (homogeneous boundary) condition from here on) and inhomogeneous deformation within grains allowing study of mis-orientation evolution, is adopted in this work.

Macroscopic stress is defined according to a simple virtual work consideration. Here, the variation of the internal work δW_{int} performed by the homogenized PK-I stress tensor $\bar{\boldsymbol{P}}$ at the macroscopic point on arbitrarily virtual displacements of the microstructure $\delta \boldsymbol{y}$ is required to be equal to the work δW_{ext} performed by the external loads on the microstructure. Internal work done by the macroscopic stress can be written as

$$\delta W_{int} = \int_{\mathcal{B}_{ref}} \bar{\boldsymbol{P}} \bullet \nabla_{ref} \delta \boldsymbol{y} dV \tag{4.4}$$

$$= \bar{\boldsymbol{P}} \bullet \int_{\partial \mathcal{B}_{ref}} \delta \boldsymbol{y} \otimes \boldsymbol{N} dA \tag{4.5}$$

External work is given as $\delta W_{ext} = \int_{\partial \mathcal{B}_{ref}} \boldsymbol{p} \cdot \delta \boldsymbol{y} dA$, where $\boldsymbol{p}$ is the traction vector at the boundary of the reference microstructure. For the HB condition, the virtual displacements at the boundary of the microstructure are obtained from the variation of the macroscopic deformation gradient as,

$$\delta \boldsymbol{y} = \delta \bar{\boldsymbol{F}} \boldsymbol{Y} \tag{4.6}$$

Thus, the external work can be written as $\delta W_{ext} = \delta \bar{\boldsymbol{F}} \bullet \int_{\partial \mathcal{B}_{ref}} \boldsymbol{Y} \otimes \boldsymbol{p} dA$. For satisfying the balance of virtual work,

$$\delta \bar{\boldsymbol{F}} \bullet \int_{\partial \mathcal{B}_{ref}} \boldsymbol{Y} \otimes \boldsymbol{p} dA = \bar{\boldsymbol{P}} \bullet \int_{\partial \mathcal{B}_{ref}} \delta \boldsymbol{y} \otimes \boldsymbol{N} dA$$

$$= \bar{\boldsymbol{P}}\delta\bar{\boldsymbol{F}}\bullet \int_{\partial\mathcal{B}_{ref}} \boldsymbol{Y}\otimes\boldsymbol{N}dA$$
$$= \delta\bar{\boldsymbol{F}}\bullet \bar{\boldsymbol{P}}V(\mathcal{B}_{ref})$$

Taking into account the fact that the equality should be satisfied for any arbitrary variation of the deformation gradient tensor $\delta\bar{\boldsymbol{F}}$, we obtain the macroscopic stresses to be of the form

$$\bar{\boldsymbol{P}} = \frac{1}{V(\mathcal{B}_{ref})}\int_{\partial\mathcal{B}_{ref}} \boldsymbol{Y}\otimes\boldsymbol{p}dA \tag{4.7}$$

An equilibrium state of the micro-structure at a certain stage of the deformation process is then assumed with the equations,

$$\nabla_{ref}\bullet\boldsymbol{P} = 0 \text{ in } \mathcal{B}_{ref} \tag{4.8}$$

$$\boldsymbol{P}^T\boldsymbol{N} = \boldsymbol{p} \text{ on } \partial\mathcal{B}_{ref} \tag{4.9}$$

Using the divergence theorem, macroscopic stresses as defined by Eq. (4.7) can be shown to be the volume-average of the microscopic stresses ($\boldsymbol{P}$)

$$\bar{\boldsymbol{P}} = \frac{1}{V(\mathcal{B}_{ref})}\int_{\mathcal{B}_{ref}} \boldsymbol{P}dV = \langle\boldsymbol{P}\rangle \tag{4.10}$$

The following relationship between the homogenized PK-1 stress and homogenized Cauchy stress is then assumed,

$$\bar{\boldsymbol{P}} = (\det\bar{\boldsymbol{F}})\bar{\boldsymbol{T}}\bar{\boldsymbol{F}}^{-T} \tag{4.11}$$

Readers are referred to the fact that virtual work principle similar to that used in the derivation of homogenized PK-1 stress can be used to prove that the macroscopic Cauchy stress ($\bar{\boldsymbol{T}}$) is also a volume-average (in the current configuration) of the microstructural counterpart ($\boldsymbol{T}$) as,

$$\bar{\boldsymbol{T}} = \langle\boldsymbol{T}\rangle \tag{4.12}$$

However, once Eq. (4.10) is assumed, then Eq. (4.11) is used to define the homogenized Cauchy stress. Thus, in the present approach, Eq. (4.12) is abandoned in favor of Eq. (4.10) (refer [35]). It is to be noted that [37] and [35] advocate the nominal stress tensor ($\boldsymbol{S} = (\det\boldsymbol{F})\boldsymbol{F}^{-1}\boldsymbol{T}$) as the averaging measure. The choice of PK-I stress as the stress measure for averaging in our work is motivated by the fact that $\boldsymbol{P}$ and $\boldsymbol{F}$ are work conjugated.

Apart from these definitions, in macro-problems with temperature effects, the temperature linking is achieved through equating the macro- ($\bar{\theta}$) and micro- (θ) temperatures and the macro- and micro- mechanical dissipation. Microstructure (material point) simulations are deemed isothermal in this work since the macro-scale temperature evolution problem is not solved.

The kinematic problem for microstructure deformation employs the updated Lagrangian framework. Here, the total micro-scale deformation gradient $\boldsymbol{F}_{n+1}$ at time $t = t_{n+1}$ of configuration $\mathcal{B}_{n+1}$ with respect to the initial undeformed configuration ($\mathcal{B}_0$) at time $t = 0$ is assumed to be decomposed as

$$\boldsymbol{F}_{n+1} = \nabla_0\tilde{\boldsymbol{y}}(\boldsymbol{Y}_0, t_{n+1}) = \nabla_n\hat{\boldsymbol{y}}(\boldsymbol{Y}_n, t)\nabla_0\tilde{\boldsymbol{y}}(\boldsymbol{Y}_0, t_n) = \boldsymbol{F}_r\boldsymbol{F}_n = \boldsymbol{F}^e\boldsymbol{F}^p \qquad (4.13)$$

where $\boldsymbol{F}^e$ is the micro-scale elastic deformation gradient at time $n+1$, $\boldsymbol{F}^p$ is the micro-scale plastic deformation gradient at time $n+1$, $\boldsymbol{F}_r$ is the relative deformation gradient with respect to the configuration at time n and $\boldsymbol{F}_n$ refers to the total micro-scale deformation gradient in the reference configuration ($\mathcal{B}_n$) with respect to the initial undeformed configuration. Going back to Fig.4.1, using the updated Lagrangian description of kinematics, $\mathcal{B}_{ref}$ would now refer to $\mathcal{B}_n$. Quantities used in the derivation of homogenized stresses would now be defined with respect to $\mathcal{B}_n$. For example, the microscopic deformation gradient $\boldsymbol{F}$ would be equal to $\boldsymbol{F}_r$

as defined in Eq. (4.13).

The equilibrium equations can be expressed in the reference configuration $\mathcal{B}_n$ as,

$$\nabla_n \cdot \boldsymbol{P}_r = \boldsymbol{0} \tag{4.14}$$

where the PK-I stress $\boldsymbol{P}_r(\boldsymbol{Y}_n, t)$ is expressed as $\boldsymbol{P}_r(\boldsymbol{Y}_n, t) = (\det \boldsymbol{F}_r)\boldsymbol{T}\boldsymbol{F}_r^{-T}$. The solution of a generic loading increment involves the solution to the principle of virtual work (PVW) given as follows: Calculate $\boldsymbol{y}(\boldsymbol{Y}_n, t)$ such that

$$\int_{\mathcal{B}_n} \boldsymbol{P}_r \cdot \nabla_n \tilde{\boldsymbol{u}} dV_n = 0 \tag{4.15}$$

for every admissible test function $\tilde{\boldsymbol{u}}$ expressed over the reference configuration $\mathcal{B}_n$. The weak form is solved in an incremental-iterative manner as a result of material non-linearities. FEM is used for the solution of the weak form and bilinear quadrilateral elements are used for the microstructure along with the assumed strain analysis scheme to counter the effect of near-incompressibility. Microstructure homogenization and multi-scaling procedure has been implemented in an object-oriented and parallel environment in C++ and PetSc parallel toolbox and is applicable to both 2D and 3D microstructures, building from our earlier work on large deformation process modeling and design in [13]. The microstructure material point problem has been parallelized by efficiently partitioning microstructure elements to every processor. Microstructure interrogation can be thought of as a material point simulator with the macro-point under consideration being subject to deformations corresponding to various processing conditions that are transferred to the boundaries of the microstructure using the HB condition.

In this work, the equivalent strain is computed based on the volume-average of the deformation rate ($\bar{\boldsymbol{D}} = \langle \boldsymbol{D} \rangle$) following the measure for which the constitutive

laws in [54] were originally developed. This is performed as a post processing step and is not required for multi-scaling. The average effective plastic strain $\bar{\epsilon}_{eff}$ is defined as

$$\bar{\epsilon}_{eff} = \int_0^t \sqrt{\frac{2}{3}\bar{\boldsymbol{D}} \cdot \bar{\boldsymbol{D}}} dt \tag{4.16}$$

Average strain measures can be alternatively derived [84] through an additional assumption that the macroscopic plastic work rate equals the plastic work rate of the microstructure in an averaged sense [80]. It should be noted that this assumption does not hold for the definition of average deformation rate used in this work.

The equivalent stress for the microstructure is represented using the von-Mises norm as,

$$\bar{\sigma}_{eff} = \sqrt{\frac{3}{2}\bar{\boldsymbol{T}}'.\bar{\boldsymbol{T}}'} \tag{4.17}$$

4.1.1 Single crystal constitutive problem

The constitutive problem adopted for a single FCC crystal $\boldsymbol{T} = \boldsymbol{T}(\boldsymbol{F}_{n+1}, \theta, \text{state})$, and computation of reorientations of crystals is described in detail in [54]. Useful features of this model include its ability to accurately model large strain elasto-viscoplastic response incorporating strain rate and temperature effects. A fully-implicit integration scheme with implicit evaluation of consistent tangent moduli as proposed in [56] is used in the microstructure deformation simulation. The constitutive problem uses a total-Lagrangian description of deformation gradient (with $\boldsymbol{F}_{n+1}$ denoting the deformation gradient at current time with respect to the initial undeformed configuration).

In the constitutive model, it is assumed that deformation takes place in a single

crystal through dislocation glide and the evolution of the plastic flow is given by

$$\dot{\boldsymbol{F}}^p(\boldsymbol{F}^p)^{-1} \;=\; \boldsymbol{L} \;=\; \sum_\alpha \dot{\gamma}^\alpha \boldsymbol{S}_0^\alpha \tag{4.18}$$

where $\boldsymbol{S}_0^\alpha \;=\; \boldsymbol{m}^\alpha \otimes \boldsymbol{n}^\alpha$ is the Schmid tensor, $\dot{\gamma}^\alpha$ is the plastic shearing rate on the slip system α and $\boldsymbol{m}^\alpha$ and $\boldsymbol{n}^\alpha$ are the slip directions and the slip plane normals, respectively in the initial configuration (at $t = 0$). An Euler-backward time integration procedure leads to the following approximation:

$$\boldsymbol{F}^p \;=\; \exp(\Delta t \sum_\alpha \dot{\gamma}^\alpha \boldsymbol{S}_0^\alpha)\boldsymbol{F}_n^p \;\approx\; (\boldsymbol{I} + \Delta t \sum_\alpha \dot{\gamma}^\alpha \boldsymbol{S}_0^\alpha)\boldsymbol{F}_n^p \tag{4.19}$$

for small Δt. Substituting Eq. (4.19) into Eq. (4.13) results in:

$$\boldsymbol{F}^e \;=\; \boldsymbol{F}^e_{trial}(\boldsymbol{I} - \Delta t \sum_\alpha \dot{\gamma}^\alpha \boldsymbol{S}_0^\alpha) \tag{4.20}$$

where $\boldsymbol{F}^e_{trial}$ is the trial elastic deformation gradient and is given as $\boldsymbol{F}_{n+1}(\boldsymbol{F}_n^p)^{-1}$. In the constitutive equations to be defined below, the Green elastic strain measure defined on the relaxed configuration (plastically deformed, unstressed configuration) $\check{\mathcal{B}}$ is utilized. It is computed using Eq. (4.20) as

$$\begin{aligned} \check{\boldsymbol{E}}^e &= \frac{1}{2}\left(\boldsymbol{F}^{eT}\boldsymbol{F}^e - \boldsymbol{I}\right) \\ &= \check{\boldsymbol{E}}^e_{trial} - \frac{\Delta t}{2}\sum_\alpha \dot{\gamma}^\alpha \left((\boldsymbol{S}_0^\alpha)^T(\boldsymbol{F}^e_{trial})^T\boldsymbol{F}^e_{trial} + (\boldsymbol{F}^e_{trial})^T\boldsymbol{F}^e_{trial}\boldsymbol{S}_0^\alpha\right) \end{aligned} \tag{4.21}$$

where $\check{\boldsymbol{E}}^e_{trial} \;=\; \frac{1}{2}\left((\boldsymbol{F}^e_{trial})^T\boldsymbol{F}^e_{trial} - \boldsymbol{I}\right)$.

The conjugate stress measure is then defined as

$$\check{\boldsymbol{T}} \;=\; \det\boldsymbol{F}^e(\boldsymbol{F}^e)^{-1}\boldsymbol{T}(\boldsymbol{F}^e)^{-T} \tag{4.22}$$

where $\boldsymbol{T}$ is the Cauchy stress for the crystal in the sample reference frame. All vector and tensorial quantities are expressed in the initial configuration $\mathcal{B}_0$. Furthermore, crystal specific properties like the stiffness and compliance have to be

transformed to this sample reference frame using the crystal orientation ($\boldsymbol{r}$). The constitutive relation, for stress, for small temperature changes about the initial temperature, θ_0, is given by

$$\check{\boldsymbol{T}} \;=\; \boldsymbol{\mathcal{L}}^e \left[\check{\boldsymbol{E}}^e \;-\; \boldsymbol{A}(\theta - \theta_0)\right] \tag{4.23}$$

where $\boldsymbol{\mathcal{L}}^e$ is the fourth-order anisotropic elasticity tensor expressed in terms of the crystal stiffness parameters and the orientation $\boldsymbol{r}$, and $\boldsymbol{A}$ is the second-order anisotropic thermal expansion tensor. Substitution of Eq. (4.21) into Eq. (4.23) results in the following

$$\begin{aligned}\check{\boldsymbol{T}} \;=\; \check{\boldsymbol{T}}_{trial} \quad - \quad \frac{\Delta t}{2}\sum_{\beta}\dot{\gamma}^{\beta}\boldsymbol{\mathcal{L}}^e\left[(\boldsymbol{S}_0^{\beta})^T(\boldsymbol{F}^e_{trial})^T\boldsymbol{F}^e_{trial} + (\boldsymbol{F}^e_{trial})^T\boldsymbol{F}^e_{trial}\boldsymbol{S}_0^{\beta}\right] \\ - (\theta - \theta_0)\boldsymbol{\mathcal{L}}^e\left[\boldsymbol{A}\right]\end{aligned} \tag{4.24}$$

where $\check{\boldsymbol{T}}_{trial} \;=\; \boldsymbol{\mathcal{L}}^e\left[\check{\boldsymbol{E}}^e_{trial}\right]$.

Further, if $s^{\alpha}(\theta)$ is the slip system resistance at temperature θ K, then the thermal and athermal components of the slip system resistance and the resolved shear stress are defined as

$$s^{\alpha} \quad = \quad s^{\alpha}_{at} \;+\; s^{\alpha}_{t} \tag{4.25}$$

$$\tau^{\alpha}_{t} \quad = \quad |\tau^{\alpha}| \;-\; s^{\alpha}_{at} \tag{4.26}$$

where the subscripts t and at denote the thermal and athermal parts, respectively and τ^{α}, the resolved shear stress for the α^{th} slip system, is computed as $\check{\boldsymbol{T}} \bullet \boldsymbol{S}_0^{\alpha}$. Such a formulation was developed in [54] and [82]. Here, part of the resolved shear stress has to overcome the athermal barriers (such as strong precipitates). Thermal barriers (such as Peierls stress and forest dislocations) are overcome by a combination of thermal energy and the resolved shear stress. Stress levels with resolved shear stress ($|\tau^{\alpha}|$) greater than slip resistance (s^{α})are unattainable. If

the resolved shear stress exceeds the athermal resistance, slip is activated. The shearing rate is then expressed accordingly as,

$$\dot{\gamma}^{\alpha} = \begin{cases} 0 & \tau_t^{\alpha} \leq 0 \\ \dot{\gamma}^0 \exp\left\{-\frac{\Delta G^{\alpha}(\tau_t^{\alpha}, s_t^{\alpha})}{k_B \theta}\right\} \text{sign}(\tau^{\alpha}), & 0 < \tau_t^{\alpha} < s_t^{\alpha} \end{cases} \tag{4.27}$$

where, the activation enthalpy is given by

$$\Delta G^{\alpha}(\tau_t^{\alpha}, s_t^{\alpha}) = \Delta F^{\alpha} \left[1 - \left\{\frac{\tau_t^{\alpha}}{s_t^{\alpha}}\right\}^p\right]^q \tag{4.28}$$

In the equation above, ΔF^{α} is the activation energy at $0K$, p and q are material parameters (generally, $0 < p < 1$ and $1 < q < 2$) and k_B is the Boltzmann constant. Furthermore, the slip system resistance parameters s_{at}^{α} and s_t^{α} evolve with deformation as

$$\dot{s}^{\alpha} = \sum_{\beta} h^{\alpha\beta} |\dot{\gamma}^{\beta}| \tag{4.29}$$

and $h^{\alpha\beta}$ is defined as

$$h^{\alpha\beta} = q^{\alpha\beta} h^{\beta} \quad \text{(no sum on } \beta) \tag{4.30}$$

$$h^{\beta} = h_0^{\beta} \, |1 - s^{\beta}/s_s^{\beta}|^{r_1} \, \text{sign}\left\{1 - \frac{s^{\beta}}{s_s^{\beta}}\right\} \tag{4.31}$$

In Eq. (4.30), $q^{\alpha\beta}$ represents the latent-hardening parameter with the following property

$$q^{\alpha\beta} = \begin{cases} 1 & \text{if } \alpha = \beta \\ q_h = 1.4 & \text{if } \alpha \neq \beta \end{cases} \tag{4.32}$$

Further, s_s^{β} represents the saturation value of s^{β}, h_0^{β} and r_1 are material response parameters. For FCC materials, s_s^{β}, the saturation state of s^{β} is considered as a constant in this work. Interested readers are referred to [54] and references therein for a more detailed physical interpretation of parameters in the constitutive model. An Euler-backward time integration of Eq. (4.29) along with Eqs. (4.30) and (4.31)

result in the following

$$s^{\alpha}_{n+1} \;=\; s^{\alpha}_{n} + \Delta t \sum_{\beta} q^{\alpha\beta} g^{\beta}(\tau^{\beta}_{n+1}, s^{\beta}_{n+1}, \theta) \tag{4.33}$$

where $g^{\beta} \;=\; h^{\beta}|\dot{\gamma}^{\beta}|$. For FCC materials, the ratio $\eta \;=\; \frac{s^{\alpha}_{t}}{s^{\alpha}_{at}}$, which is a constant, is utilized to evaluate the thermal and athermal parts of slip system hardness as

$$s^{\alpha}_{at} \;=\; s^{\alpha}_{n+1}\frac{1}{1+\eta} \tag{4.34}$$

$$s^{\alpha}_{t} \;=\; s^{\alpha}_{n+1}\frac{\eta}{1+\eta} \tag{4.35}$$

The resolved shear stress τ^{α} and the slip system resistance s^{α} is solved from the coupled system given by Eqs. (4.24), (4.27) and (4.33) using an iterative scheme (algorithm can be found in [56].

For calculation of texture, we employ the Rodrigues-Frank space representation of texture. Details of neo-Eulerian representations and the use of Rodrigues-Frank space can be found in [56]. The re-orientation velocity is here evaluated as:

$$\boldsymbol{v} \;=\; \frac{\partial \boldsymbol{r}}{\partial t} \;=\; \frac{1}{2}\left(\boldsymbol{\omega} \;+\; (\boldsymbol{\omega}\cdot\boldsymbol{r})\boldsymbol{r} \;+\; \boldsymbol{\omega}\times\boldsymbol{r}\right) \tag{4.36}$$

where $\boldsymbol{r}$ is the orientation (Rodrigues' parametrization) and $\boldsymbol{\omega}$ represents the spin vector defined as $\boldsymbol{\omega} \;=\; \text{vect}\left(\dot{\boldsymbol{R}}^{e}\boldsymbol{R}^{eT}\right) \;=\; \text{vect}\left(\boldsymbol{\Omega}\right)$, where $\boldsymbol{R^{e}}$ is evaluated through the polar decomposition of the elastic deformation gradient $\boldsymbol{F}^{e}$ as $\boldsymbol{F}^{e} \;=\; \boldsymbol{R}^{e}\boldsymbol{U}^{e}$. Considering the Euler-backward time integration of $\dot{\boldsymbol{R}}^{e}\boldsymbol{R}^{eT} \;=\; \boldsymbol{\Omega}$, where $\boldsymbol{\Omega}$ is the spin tensor, leads to the following:

$$\boldsymbol{R}^{e}_{n+1} \;=\; \exp(\Delta t\boldsymbol{\Omega}_{n+1})\boldsymbol{R}^{e}_{n} \tag{4.37}$$

and

$$\boldsymbol{\Omega}_{n+1} \;=\; \frac{1}{\Delta t}\ln\left\{\boldsymbol{R}^{e}_{n+1}\boldsymbol{R}^{eT}_{n}\right\} \tag{4.38}$$

Once the constitutive problem is solved, $\boldsymbol{F}^{e}_{n+1}$ can be evaluated from Eq. (4.20). From the elastic deformation gradient, $\boldsymbol{R}^{e}_{n+1}$ and $\boldsymbol{R}^{e}_{n}$ are evaluated and one can

then evaluate the spin tensor $\boldsymbol{\Omega}_{n+1}$ using Eq. (4.38). The re-orientation velocity can be computed from Eq. (4.36) which is used to update the orientation of the crystal $\boldsymbol{r}$.

This completes the constitutive problem which is solved at each integration point of the discretized microstructure. In addition, to solve the non-linear Eq. (4.15) for the microstructure, a Newton-Raphson (NR) iterative scheme along with a line search procedure is employed. An implicit technique for linearization of the PK-I stress for the NR iterations based on the constitutive problem described here can be found in [56].

Although FE homogenization provides an improved model accounting for non-uniform deformations within the microstructure, two shortcomings need to be pointed out in the context of multi-scaling. Firstly, the dimensions of the microstructure representative volume element (RVE) do not influence the averaging procedure. This arises from the assumption that the microstructure is infinitesimal compared to the macro-scale and hence, is seen as a macroscopic material point. Thus, the homogenization result is independent of the overall dimensions of the microstructure. Secondly, use of first-order expansion of microstructural deformation (Eq. (4.2)) restricts the analysis to simple deformation modes (rotation, tension, shear or combinations thereof) at the micro-scale. In spite of these drawbacks, the homogenization approach followed here allows additional convenience of using the same algorithm as a plug-in in large strain continuum scale simulations with minimal modifications to account for microstructural degrees of freedom. To perform multi-scaling, the consistent tangent moduli for the macro-scale is derived in the next section.

Consistent tangent moduli at macro-scale for multi-scale modelling

using the homogenization approach: Eq. 4.7 shows the homogenization relation for the PK-I stress tensor. When using finite element method to numerically evaluate this integral (for the case of HB condition), the equation is approximated as follows,

$$\bar{\boldsymbol{P}} = \frac{1}{V(\mathcal{B}_{ref})} \sum_{i=1}^{N_b} \boldsymbol{Y}^i \otimes \boldsymbol{f}^i \tag{4.39}$$

where, $\boldsymbol{f}^i$ is the external force at boundary node i; $\boldsymbol{Y}^i$ is the position vector of boundary node i in the reference state and N_b is the number of nodes on the boundary of the microstructure. The consistent tangent modulus can be obtained from the relation:

$$\delta\bar{\boldsymbol{P}} = \frac{1}{V(\mathcal{B}_{ref})} \sum_{i=1}^{N_b} \boldsymbol{Y}^i \otimes \delta\boldsymbol{f}^i \tag{4.40}$$

To obtain $\delta\boldsymbol{f}$ as a function of $\delta\boldsymbol{F}_r$, the global stiffness matrix obtained from finite element solution of Eq. 4.15 is used [85]. The global matrix is rearranged to the following form:

$$\begin{bmatrix} \boldsymbol{K}_{bb} & \boldsymbol{K}_{bi} \\ \boldsymbol{K}_{ib} & \boldsymbol{K}_{ii} \end{bmatrix} \begin{bmatrix} \delta\boldsymbol{u}^b \\ \delta\boldsymbol{u}^i \end{bmatrix} = \begin{bmatrix} \delta\boldsymbol{f}^b \\ \boldsymbol{0} \end{bmatrix}$$

where, indices b and i refer to quantities at the boundary nodes and at the internal nodes respectively. $\boldsymbol{K}_{bb}$, $\boldsymbol{K}_{bi}$, $\boldsymbol{K}_{ib}$ and $\boldsymbol{K}_{ii}$ correspond to the rearranged sub-matrices of the total RVE stiffness matrix $\boldsymbol{K}$ so that the incremental forces at boundary nodes $\delta\boldsymbol{f}^b$ and the incremental displacements $\delta\boldsymbol{u}^b$ are arranged at the top rows of the force and displacement matrix. The stiffness matrix $\boldsymbol{K}$ is obtained at the end of a converged microstructural sub-problem at an integration point

on the macro-scale. Matrix equation above is then re-arranged further to obtain the matrix K_B relating incremental boundary displacements to the corresponding change in boundary forces.

$$\boldsymbol{K}_B \delta \boldsymbol{u}^b = \delta \boldsymbol{f}^b \tag{4.41}$$

$$\boldsymbol{K}_B = \boldsymbol{K}_{bb} - \boldsymbol{K}_{bi} \boldsymbol{K}_{ii}^{-1} \boldsymbol{K}_{ib}. \tag{4.42}$$

This equation is further rearranged into the following form,

$$\sum_{j=1}^{N_b} \boldsymbol{\kappa}^{ij} \delta \boldsymbol{u}^j = \delta \boldsymbol{f}^i \tag{4.43}$$

$$\tag{4.44}$$

where, $\delta \boldsymbol{f}^i$ is the change in boundary force at boundary node i due to incremental boundary displacements $\delta \boldsymbol{u}^j$ at all boundary nodes $j = 1, .., N_b$; and $\boldsymbol{\kappa}^{ij}$ are sub-matrices corresponding to rows and columns of degrees of freedom associated with boundary nodes i and j in matrix $\boldsymbol{K}_B$. The above equation is then substituted into Eq. 4.40 so that we obtain $\delta \bar{\boldsymbol{P}}$ in the following numerical form:

$$\delta \bar{\boldsymbol{P}} = \frac{1}{V(\mathcal{B}_{ref})} \sum_{i=1}^{N_b} \boldsymbol{Y}^i \otimes (\sum_{j=1}^{N_b} \boldsymbol{\kappa}^{ij} \delta \boldsymbol{u}^j) \tag{4.45}$$

The final step is the use of the homogenization boundary condition $\delta \boldsymbol{u}^j = \delta \boldsymbol{F} Y^j$ as follows,

$$\delta \bar{\boldsymbol{P}} = \frac{1}{V(\mathcal{B}_{ref})} \sum_{i=1}^{N_b} \sum_{j=1}^{N_b} \boldsymbol{Y}^i (\boldsymbol{\kappa}^{ij} \delta \boldsymbol{F} \boldsymbol{Y}^j)^T \tag{4.46}$$

The above equation can be rearranged as follows (written in indicial notation for clarity):

$$\delta \bar{\boldsymbol{P}}_{mn} = \frac{1}{V(\mathcal{B}_{ref})} \sum_{i=1}^{N_b} \sum_{j=1}^{N_b} \boldsymbol{Y}^i_{\ n} \boldsymbol{\kappa}^{ij}_{mo} \boldsymbol{Y}^j_{\ p} \delta \boldsymbol{F}_{op} \tag{4.47}$$

This leads to the form of consistent tangent moduli at the macroscopic scale at the material point for the homogenization problem by comparing with the linearized equation $\delta\bar{\boldsymbol{P}}_r = \boldsymbol{\mathcal{C}} : \delta\boldsymbol{F}_r$ where the consistent tangent moduli $\boldsymbol{\mathcal{C}}$ is given as follows,

$$\boldsymbol{\mathcal{C}}_{mnop} = \frac{1}{V(\mathcal{B}_{ref})} \sum_{i=1}^{N_b} \sum_{j=1}^{N_b} \boldsymbol{Y}^{i}_{\ n} \boldsymbol{\kappa}^{ij}_{mo} \boldsymbol{Y}^{j}_{\ p}. \tag{4.48}$$

4.2 Numerical examples

In the numerical examples that follow, idealized grain structures are used to compare the performance of homogenization model vis-a-vis Taylor-based models in example 1 and experimental results in example 2. Interrogation of realistic 3D polyhedral micro-structure is demonstrated in example 3. A material composed of 99.987% pure polycrystalline FCC aluminum is used in these examples. The anisotropic elasticity tensor for FCC aluminum can be specified in terms of the three stiffness parameters (crystal stiffness tensor $\boldsymbol{C}$ in the crystal frame) which are approximated (in GPa) in terms of the temperature θ (in K) in [54] as follows

$$\begin{aligned} c_{11} &= 123.323 + 6.7008 * 10^{-8}\theta^3 - 1.1342 * 10^{-4}\theta^2 - 7.8788 * 10^{-3}\theta \\ c_{12} &= 70.6512 + 4.4105 * 10^{-8}\theta^3 - 7.5498 * 10^{-5}\theta^2 + 3.9992 * 10^{-3}\theta \\ c_{44} &= 31.207 + 7.047 * 10^{-9}\theta^3 - 1.214 * 10^{-5}\theta^2 - 8.327 * 10^{-3}\theta \end{aligned} \tag{4.49}$$

Furthermore, the saturation values of the slip system resistances are taken equal for all slip systems as $s_s(300K) = 50.6\ MPa$. Slip is assumed to occur in the twelve $\{111\} < 110 >$ slip systems. Additional material properties taken from [54] are listed in Table 4.1.

Example 1: Comparison of response of idealized 2D polycrystal in simple shear

Table 4.1: Material properties of FCC Aluminum.

Material parameter	value
$\dot{\gamma}^0$	1.732E+06 /s
h_0	250 MPa
r_1	2.0
p	0.141
q	1.1
$s_{at,0}$	8.76 MPa
$s_{t,0}$	8.76 MPa
ϖ	1.0
ρ	2.77 Mg/m^3
c	920.0 J/kg-K

and plane strain compression with Taylor models:

The result of pure shear and plane strain compression of a 99.98% pure FCC aluminum aggregate using homogenization are compared with Taylor models based on stress-strain curves and texture evolution. The parameters used for the simulations are temperature of 300 K with strain rate of 6.667E-4 s^{-1}. Microstructure is modeled as a collection of 400 grains with each grain represented with a single finite element as shown in Fig. 4.2(a). The corresponding initial ODF is plotted in Fig. 4.2(d). The ODF is obtained by assuming that each orientation acts as a Gaussian point source within the fundamental region. This converts the discrete set of 400 orientations to a continuous distribution of orientations in the fundamental region. This representation was used in the ODF-Taylor simulation of [56]

for comparing with the FE-homogenized model. The reference fundamental region is discretized into 148 tetrahedral elements with cubic symmetry enforced in the solution procedure (for more details of this technique refer to [56]). The ODF-Taylor method utilizes a finite element solution of ODF conservation law which conserves the crystal volume fractions over the polycrystal when grains reorient during deformation. The other model used for comparison is based on discrete-Taylor analysis of the aggregate of grains in Fig. 4.2(a). The constitutive law was calibrated with experimental results in [54] to suit Taylor based computations. Here, same constitutive law parameters are used for both Taylor model and FE homogenization. From Fig. 4.2(c) it can be seen that homogenization technique provide a softer response than the Taylor model. The equivalent stress-strain curve obtained from ODF-Taylor and aggregate-Taylor almost exactly match. These models theoretically provide the upper bound of the stress-strain curve for the given microstructure due to strong kinematic constraint of equal deformation in all crystals. On the contrary, using finite element homogenization we find that crystal deformation is partitioned so that both compatibility and equilibrium are satisfied leading to a softer response. Uneven distribution of deformation among grains due to the effect of neighbors with various degrees of misorientation can be seen from the final microstructure in Fig. 4.4(a). Comparison of the ODFs in Figs. 4.2(e-f) and Figs. 4.4(c-d) show that Taylor model provides sharper textures as expected, while over-predicting the final texture. The $< 110 >$ and the $< 111 >$ pole figure from both the ODF-Taylor model and FE-homogenized model are further compared in shear (Fig. 4.3(a)) and plane strain compression (Fig. 4.3(b)) at equivalent strain of 0.3 reveal the sharper features of the Taylor model compared to FE-homogenization.

Example 2: Comparison of response of idealized 3D polycrystal in simple shear

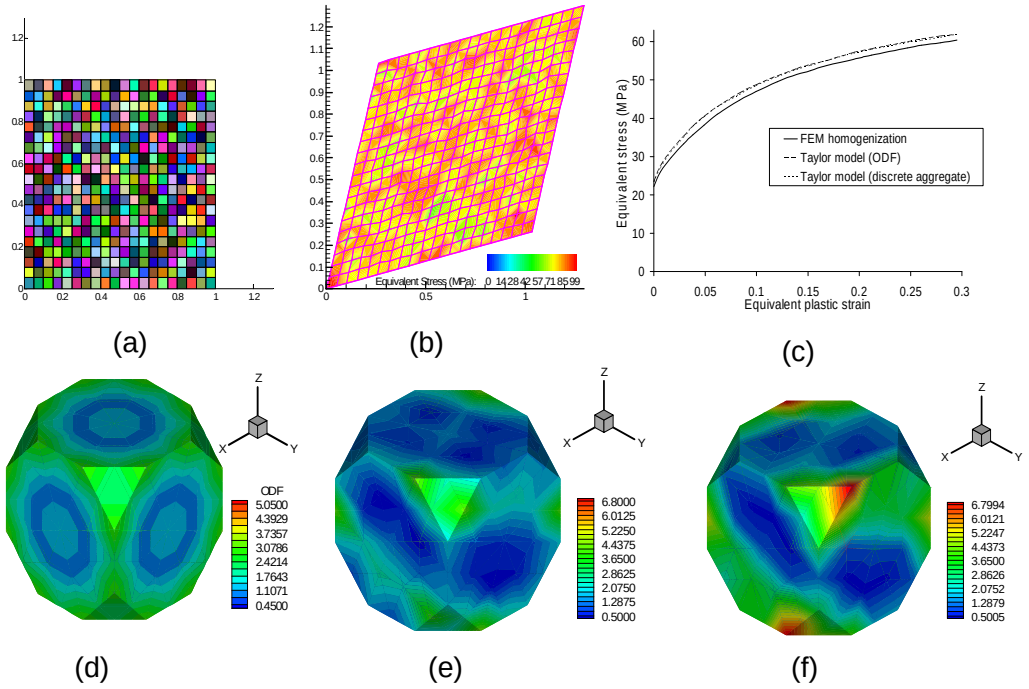

Figure 4.2: Homogenization of an idealized 2D polycrystal: (a) Idealized 2D polycrystal with 400 grains with 1 finite element per grain. (b) Equivalent stress field after deformation in pure shear mode at a strain rate of 6.667E-4 s^{-1}. (c) Comparison of the equivalent stress-strain curve predicted through homogenization with Taylor simulation. (d) The initial texture of the polycrystals represented as an ODF in Rodrigues space. (e) Texture prediction using finite element homogenization and (f) texture prediction using the Taylor model at time t = 210 sec. The Taylor model gives sharper and stronger textures and provides upper bound of the stress-strain curve.

with experimental results from literature.

The experimental results of simple shear of an aggregate of FCC Aluminum crystals were obtained by digitizing the stress-strain curves presented in [93]. The experiment was performed at a constant strain rate of $6.667E-4s^{-1}$ and a temperature of 300 K. The numerical experiment simulated a simple shear motion with the final state of the microstructure depicted in Fig. 4.5(c). The initial texturing of the material is modelled to be random with the initial $< 110 >$ and $< 111 >$ pole

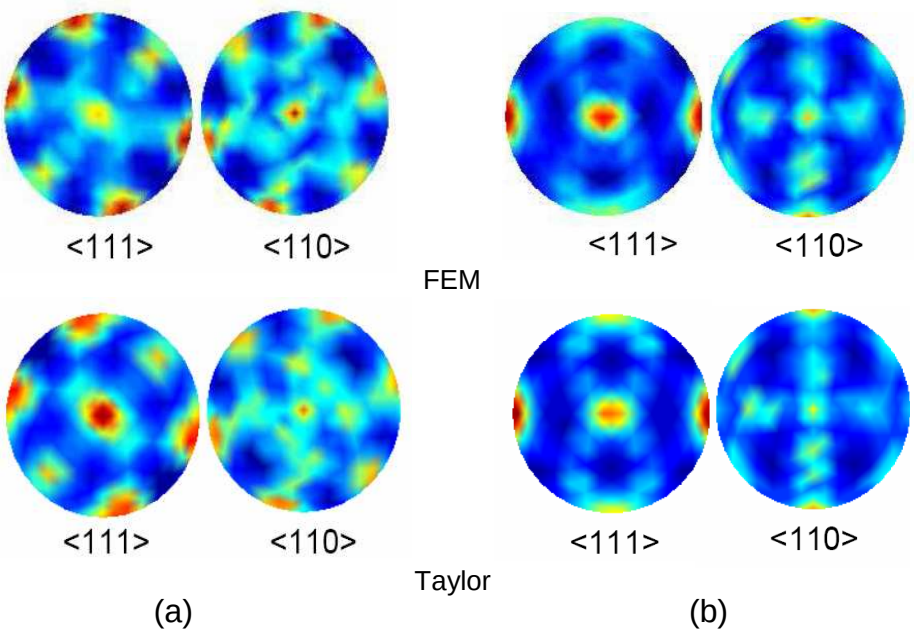

Figure 4.3: Comparison of the FEM and Taylor predictions of final $< 110 >$ and $< 111 >$ textures after (a) pure shear and (b) plane strain compression.

figures shown in Fig. 4.5(b). A 512 grain idealized microstructure (with 1 finite element per grain) is used in the homogenization procedure to numerically generate the response to simple shear. The predicted and experimental stress-strain responses are superposed in Fig. 4.5(d). The simulation was also carried out using the the 400 grain 2D idealized microstructure in example 1 using an initial random texture and the corresponding stress-strain curve is also superposed in Fig. 4.5(d) showing that a 2D approximation is equally valid in this case. Numerical response closely follows the experimental response but is softer since parameters calibrated using Taylor model (in [54]) were used in the homogenization model. The final texture of the material represented using the $< 110 >$ and $< 111 >$ pole figures are also depicted in Fig. 4.5(b). As expected, simulated texture is dominated by x-axis $< 110 >$ fibers, (along the x-face of the ODF) at the strain level of 0.3, as seen from the final ODF obtained in Fig. 4.5(a).

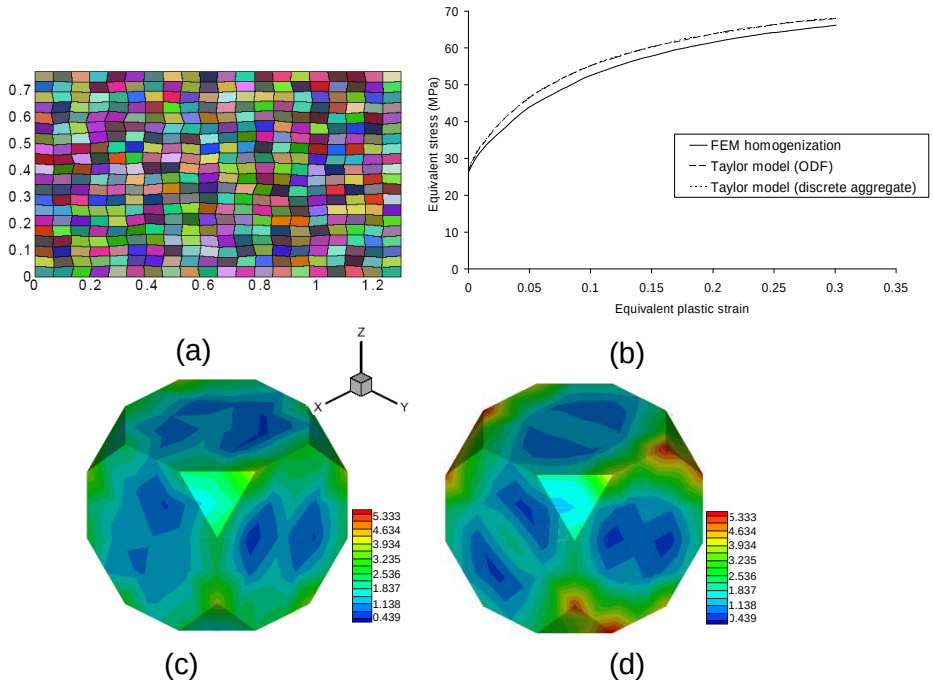

Figure 4.4: (a) Final deformed state of the microstructure in example 1 after plane strain compression. (b) Comparison of the equivalent stress–strain curve predicted through homogenization with Taylor simulation. (c) Texture prediction using finite element homogenization and (d) the Taylor model at $t = 130$ sec.

Example 3: Response of realistic 3D microstructures.

Example of interrogation of realistic 3D microstructures obtained from Monte Carlo Potts grain growth program from the work in [134] is demonstrated in Fig. 4.6. Finite element discretization of the 3D microstructure was directly transferred from the structured mesh used in the Monte Carlo Potts simulation. The domain is discretized using a $24 \times 24 \times 24$ grid and is shown in Fig. 4.6.

The homogenized response of the microstructure in plane strain compression and shear are compared and presented in Fig. 4.6(b). The equivalent stress field for both shear and plane strain compression are compared at a homogenized strain level of 0.060 in Fig. 4.6(c) and (d), respectively. The simulation was performed

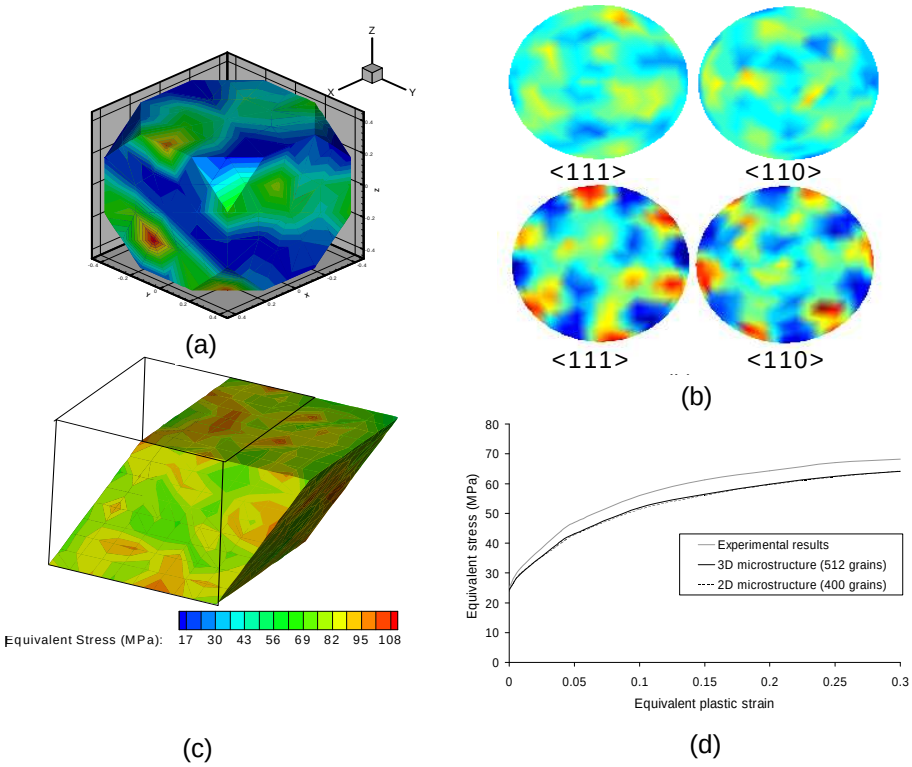

Figure 4.5: Homogenization of an idealized 3D polycrystal with 512 grains: (a) The final ODF obtained after simple shear. (b) The initial random texture of the material (top) represented using the $<110>$ and $<111>$ pole figures. The final pole figures after deformation are shown at the bottom (c) Equivalent stress field after deformation in pure shear mode. (d) Comparison of the equivalent stress-strain curve predicted through homogenization with experimental results from [93].

on 60 X64 Intel processors with a clock speed of 3.6 GHz using PetSc KSP solvers on the Cornell theory center's supercomputing facility. Each simulation was carried out over 2000 equal time steps and took about 1200 minutes to solve in the parallel environment. In all examples, an assumed strain analysis scheme is used to treat the effect of near-incompressibility based on the work in [13]. To aid in speeding up the solution process for complex forging processes, the design simulator was also parallelized using MPI. The simulator was developed using object oriented programming and dynamically linked to the PetSc for parallel assembly

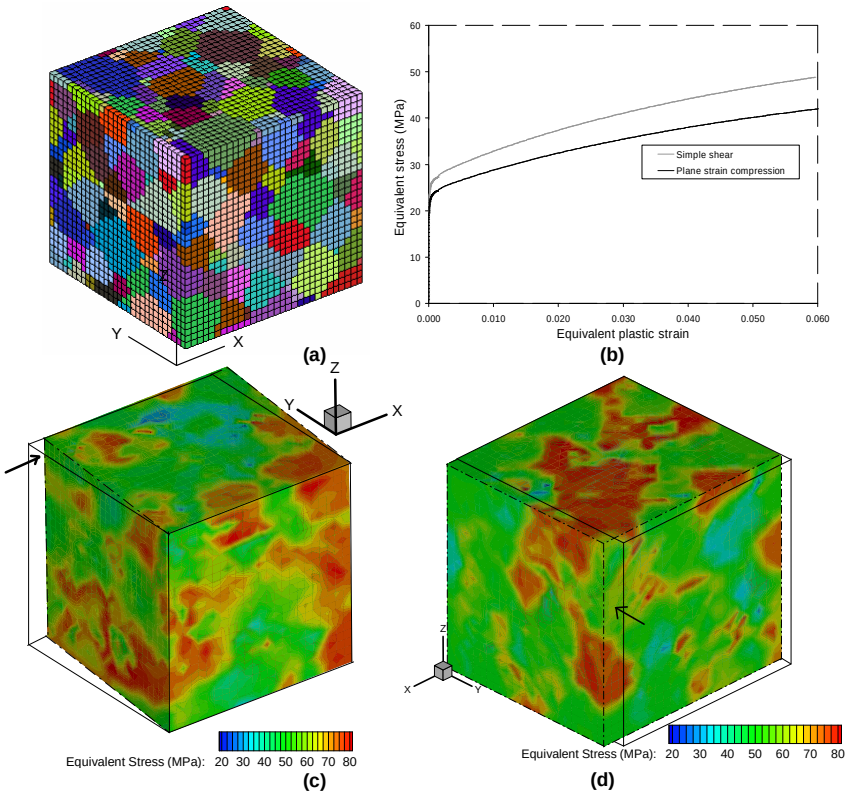

Figure 4.6: (a) Microstructure obtained from a MC grain growth simulation (b) Comparison of equivalent stress-strain curve for the two cases and equivalent stress field of a 3D microstructure (above) after (c) simple shear and (d) plane strain compression.

and solution of linear systems.

4.3 Conclusions

A finite element homogenization model is presented for modelling elasto-viscoplastic behavior and texture evolution in a polycrystal subject to finite strains. The technique utilizes macro-micro linking techniques obtained from homogenization theory. An updated Lagrangian finite element formulation is invoked to interrogate the microstructure and averaging schemes are utilized to identify the macro-

response. The model is found to be capable of predicting non-homogeneous stress and deformation fields in 2D and 3D microstructures. Comparison to ODF-Taylor, aggregate-Taylor and experimental results with respect to the equivalent stress-strain curves and texture development reveals that the model performs as expected providing softer response and smoother textures.

Work presented here is focused on the material point problem of controlling microstructures to obtain desired response. The method lends itself to subsequent development of multi-scale processing model. The homogenization approach can be easily linked with large strain continuum scale simulations with minimal modifications to account for microstructural degrees of freedom. In the next chapter, we explore the applicability of controlling process parameters such as strain rates in order to obtain desired response.

Chapter 5

Design of microstructure-sensitive properties in elasto-viscoplastic polycrystals using multi-scale homogenization

Deformation process design for desired material properties has for long been empirical in nature. Such approaches are not only time consuming but also quite costly. With these issues in mind, in this section, an efficient framework is developed for computational design for desired microstructure-sensitive properties. The design framework adopted here is based on a gradient optimization method. To calculate the gradients of the objective function and constraints, one needs to calculate the sensitivities i.e. change in the property to be controlled due to infinitesimal perturbations to the design parameters.

The sensitivities are evaluated using the continuum sensitivity method (CSM). The continuum sensitivity method (CSM) used for designing processes involves differentiation of the governing field equations of homogenization, as explained in the previous chapter, with respect to the processing parameters and development of the weak forms for the corresponding sensitivity equations that are solved using finite element analysis. The sensitivity of the deformation field within the microstructure is exactly defined and an averaging principle is developed to compute

[4] Reproduced from V. Sundararaghavan and N. Zabaras, "Design of microstructure-sensitive properties in elasto-viscoplastic polycrystals using multi-scale homogenization", International Journal of Plasticity, Vol. 22, pp. 1799-1824, 2006.

the sensitivity of homogenized stresses at the macro-scale due to perturbations in the process parameters.

Computed sensitivities are used within a gradient-based optimization framework for controlling the response of the microstructure. Processing parameters that would lead to a desired equivalent stress-strain curve in a sample poly-crystalline microstructure are identified for single and two-stage loading using the design algorithm.

5.1 Continuum sensitivity technique for process optimization at a material point

A problem of interest to manufacturing engineers is to identify improved processing parameters that would closely achieve desired properties in materials. We define the design problem of interest as identification of the right combination of process modes involving plane strain tension/compression (rolling), shear and rotation, and the corresponding process parameters $\boldsymbol{\alpha}$ that would lead to a desired property χ that is a function of the given microstructure. The macro-velocity gradient ($\tilde{\boldsymbol{L}} = \dot{\bar{\boldsymbol{F}}}\bar{\boldsymbol{F}}^{-1}$) is decomposed uniquely for 2D microstructure analysis as follows

$$\tilde{\boldsymbol{L}} = \alpha_1 \begin{bmatrix} 1 & 0 & 0 \\ 0 & -1 & 0 \\ 0 & 0 & 0 \end{bmatrix} + \alpha_2 \begin{bmatrix} 0 & 1 & 0 \\ 1 & 0 & 0 \\ 0 & 0 & 0 \end{bmatrix} + \alpha_3 \begin{bmatrix} 0 & -1 & 0 \\ 1 & 0 & 0 \\ 0 & 0 & 0 \end{bmatrix} \quad (5.1)$$

Similar decomposition for $3D$ deformation problems can be found in [61]. Each matrix in the decomposition of Eq. (5.1) corresponds to a given deformation process

namely plane strain tension/compression (α_1), plane shear mode (α_2) and rotation mode (α_3). Note that here $\tilde{\boldsymbol{L}}$ is introduced to define the deformation modes at the macro-scale as in our earlier work and that $\tilde{\boldsymbol{L}} \neq \bar{\boldsymbol{L}}$.

The macroscopic deformation gradient at time step $n+1$ ($\bar{\boldsymbol{F}}_{n+1}$) is computed based from the definition of $\tilde{\boldsymbol{L}}_{n+1}$ using a backward Euler approximation as,

$$\bar{\boldsymbol{F}}_{n+1} = \bar{\boldsymbol{F}}_n(\boldsymbol{I} + \tilde{\boldsymbol{L}}_{n+1}\Delta t) \tag{5.2}$$

The design problem is posed as the identification of process parameters $\boldsymbol{\alpha} = [\alpha_1, \alpha_2, \alpha_3]$ that would lead to a desired homogenized property χ. This can be stated by the minimization problem:

$$\min_{\boldsymbol{\alpha}} \quad \mathcal{F}(\boldsymbol{\alpha}) \;=\; \frac{1}{N_s} \sum_{i=1}^{N_s} \left(\chi^i\left(\mathcal{B}(\boldsymbol{\alpha})\right) - \chi^{desired^i}\right)^2 \tag{5.3}$$

where N_s is the total number of sampling points and $\chi^{desired}$ is the discrete representation of the desired homogenized microstructural property.

We denote the sensitivity (directional-derivative) of the microstructure to a small change in the process parameter ($\boldsymbol{\alpha}$) as $\overset{\circ}{\mathcal{B}} = \overset{\hat{\circ}}{\mathcal{B}}(r, t; \boldsymbol{\alpha}, \Delta\boldsymbol{\alpha})$. The i^{th} sensitivity problem is driven by $\Delta\alpha_i = 10^{-5}$ with $\Delta\alpha_j = 0$ for $j \neq i$. The gradients of property (χ) with respect to α_i is calculated as,

$$\frac{\partial \chi}{\partial \alpha_i} = \frac{\overset{\circ}{\chi}\left(\mathbf{r}, t, \alpha_1, .., \alpha_3, 0, .., \Delta\alpha_i, .., 0\right)}{\Delta\alpha_i} \tag{5.4}$$

In general, the homogenized property (χ) is a function of a homogenized field ($\bar{\boldsymbol{\Upsilon}}$). In examples 1 and 2 of Section 5.2, the property to be optimized is taken to be the time history of homogenized equivalent stress ($\chi = \bar{\sigma}_{eff}$). Calculation of the homogenized equivalent stress involves calculation of the sensitivity of the PK-1 stress (in this case, $\boldsymbol{\Upsilon} = \boldsymbol{P}$). The expression for the sensitivity of a homogenized

field ($\bar{\boldsymbol{\Upsilon}}$) over the microstructure configuration ($\mathcal{B}$) is determined as follows,

$$\begin{aligned}\overset{\circ}{\bar{\boldsymbol{\Upsilon}}} &= \overset{\circ}{\overline{\frac{1}{V(\mathcal{B})}\int_{\mathcal{B}} \boldsymbol{\Upsilon}(\boldsymbol{y},t;\boldsymbol{\alpha})dV}} \\ &= -\frac{\overset{\circ}{V}(\mathcal{B})}{V(\mathcal{B})}\bar{\boldsymbol{\Upsilon}} + \frac{1}{V(\mathcal{B})}\int_{\mathcal{B}} (\overset{\circ}{\Upsilon}(\boldsymbol{y},t;\boldsymbol{\alpha}) + \Upsilon(\boldsymbol{y},t;\boldsymbol{\alpha}) tr(\overset{\circ}{\boldsymbol{F}}_{n+1}\,\boldsymbol{F}_{n+1}^{-1}))\, dV \quad (5.5)\end{aligned}$$

Sensitivities of the homogenized property are then used in the steepest descent optimization algorithm to obtain the optimum process parameters that minimize the objective function in Eq. (5.3). Computational schemes for rigorously computing these sensitivities from the governing equations of microstructure evolution are described next.

5.1.1 Deformation sensitivity problem

The interest in this problem is to compute how perturbations on the macro-design variables $\boldsymbol{\alpha}$ affect the micro-fields - mainly the stresses within the microstructure. We compute the resulting variation of the microstructure and other microstructural properties from the perturbation $\overset{\circ}{\bar{\boldsymbol{F}}}_{n+1}$ of $\bar{\boldsymbol{F}}_{n+1}$. $\overset{\circ}{\bar{\boldsymbol{F}}}_{n+1}$ is in turn obtained from perturbation $\overset{\circ}{\tilde{\boldsymbol{L}}}_{n+1}$ of the macro-velocity gradient $\tilde{\boldsymbol{L}}_{n+1}$ as,

$$\overset{\circ}{\bar{\boldsymbol{F}}}_{n+1} = (\boldsymbol{I} + \tilde{\boldsymbol{L}}_{n+1}\Delta t)(\overset{\circ}{\bar{\boldsymbol{F}}}_{n} + \overset{\circ}{\tilde{\boldsymbol{L}}}_{n+1}\,\bar{\boldsymbol{F}}_{n+1}\Delta t) \quad (5.6)$$

Similar multi-scale boundary conditions such as those developed in the previous section can be used for the sensitivity problem. In particular, we define the sensitivity linking as follows: the sensitivity of the averaged deformation gradient at a material point is taken to be the same as the sensitivity of the deformation gradient on the boundary of the underlying microstructure, in the reference

frame. The equilibrium equation for the microstructure is then considered and design-differentiated. This differential, sensitivity equilibrium equation is posed in a weak form so as to establish a principle of virtual work like equation for the calculation of the sensitivity of deformation fields in the microstructure. Consistent with this mode of analysis, the sensitivity constitutive problem is directly derived by differentiating the constitutive equations given in the previous section. Described below is the analysis for the development of a total Lagrangian sensitivity formulation for the kinematic problem (with microstructure at time step $t = t_0$ as the reference configuration at time step n). The design-differentiation of the equilibrium equation (Eq. (4.14)) results in:

$$\overset{\circ}{\overbrace{\nabla_0 \bullet \boldsymbol{P}}} = \mathbf{0} \tag{5.7}$$

where $\boldsymbol{P}$ is the PK-I stress defined earlier. A variational form for the sensitivity equilibrium equation (for parameter sensitivity) can be posed as follows: Evaluate $\overset{\circ}{\boldsymbol{y}} = \overset{\circ}{\hat{\boldsymbol{y}}}(\boldsymbol{Y}_0, t; \boldsymbol{\alpha}, \Delta\boldsymbol{\alpha})$ such that

$$\int_{\mathcal{B}_0} \overset{\circ}{\boldsymbol{P}} \bullet \nabla_0 \tilde{\boldsymbol{\eta}} dV_0 = 0 \tag{5.8}$$

for every $\tilde{\boldsymbol{\eta}}$, a kinematically admissible sensitivity deformation field expressed over the reference configuration. In order to solve the weak form, defined by Eq. (5.8), relationships between (a) $\overset{\circ}{\boldsymbol{F}}_{n+1}$ and $\overset{\circ}{\boldsymbol{y}}$ (sensitivity of the kinematic problem) and (b) $\overset{\circ}{\boldsymbol{P}}$ and $[\overset{\circ}{\boldsymbol{F}}_{n+1}, \overset{\circ}{\theta}]$ (sensitivity of the constitutive problem) needs to be defined. The relationship between $\overset{\circ}{\boldsymbol{F}}_{n+1}$ and $\overset{\circ}{\boldsymbol{y}}$ is purely kinematic ($\overset{\circ}{\boldsymbol{F}}_{n+1} = \nabla_0 \overset{\circ}{\boldsymbol{y}}$). The relationship between $\overset{\circ}{\boldsymbol{P}}$ and $[\overset{\circ}{\boldsymbol{F}}_{n+1}, \overset{\circ}{\theta}]$ is obtained from the sensitivity constitutive problem to be discussed in Section 5.1.2 and takes the form:

$$\overset{\circ}{\boldsymbol{P}} = \boldsymbol{\mathcal{B}} [\overset{\circ}{\boldsymbol{F}}_{n+1}] + \boldsymbol{A} \overset{\circ}{\theta} + \boldsymbol{B} \tag{5.9}$$

where $\boldsymbol{\mathcal{B}}$ is a fourth order tensor and $\boldsymbol{A}, \boldsymbol{B}$ are second order tensors. These tensors, are constants, defined from known direct and sensitivity fields at the previous time

step, are obtained by considering the crystal constitutive response as described in the next subsection.

5.1.2 Sensitivity constitutive problem

Through the crystal sensitivity constitutive sub-problem, the relationship between the crystal parameters, $\overset{\circ}{\boldsymbol{T}}$ and $\left\{\overset{\circ}{\boldsymbol{F}},\ \overset{\circ}{\theta}\right\}$ is computed. As part of the update procedure, one computes the set $\left\{\overset{\circ}{\boldsymbol{T}},\ \overset{\circ}{s},\ \overset{\circ}{\tau},\ \overset{\circ}{\boldsymbol{F}}^e,\ \overset{\circ}{\boldsymbol{F}}^p\right\}$ at each integration point in the microstructure at the end of the time increment t_{n+1}, where the sensitivity of the deformation gradient at the boundary of the microstructure $\overset{\circ}{\boldsymbol{F}}_{n+1}$ (and the sensitivity of the temperature field $\overset{\circ}{\theta}_{n+1}$) are known from the macro-perturbations.

The microstructure configuration $\mathcal{B}_{n+1}$ is known at t_{n+1} from the direct problem. The constitutive sensitivity problem for a crystal orientation is history-dependent and the solution of the sensitivity problem at time t_n is known for each crystal orientation, yielding the variables $\left\{\overset{\circ}{\boldsymbol{T}},\ \overset{\circ}{s},\ \overset{\circ}{\tau},\ \overset{\circ}{\boldsymbol{F}}^e,\ \overset{\circ}{\boldsymbol{F}}^p\right\}$ at the beginning of each time increment. Although the microstructure interrogation problem is at a fixed temperature, the following discussion also includes thermal sensitivity effects based on $\overset{\circ}{\theta}_{n+1}$ from the macro-scale.

Computing the linear relation between $\overset{\circ}{s}^\alpha$ and $\left\{\overset{\circ}{\check{\boldsymbol{T}}}_{n+1},\ \overset{\circ}{\theta}_{n+1}\right\}$ Consider the design-differentiation of the evolution equation for the deformation resistance, s^α (Eq. (4.29)). It results in:

$$\frac{\partial\ \overset{\circ}{s}^\alpha}{\partial t}\ =\ \sum_\beta \left[\overset{\circ}{h}^{\alpha\beta}\ |\dot{\gamma}^\beta|\ +\ h^{\alpha\beta}\ \overline{\overset{\circ}{|\dot{\gamma}^\beta|}}\right] \tag{5.10}$$

Incorporating Eqs. (4.30) and (4.31) and performing an Euler-backward integration

results in:

$$\overset{\circ}{s^{\alpha}}_{n+1} - \Delta t \sum_{\beta} q^{\alpha\beta} \frac{\partial g^{\beta}}{\partial s^{\beta}} \overset{\circ}{s^{\beta}}_{n+1} = \overset{\circ}{s^{\alpha}}_{n} +$$

$$\Delta t \sum_{\beta} q^{\alpha\beta} \frac{\partial g^{\beta}}{\partial \tau^{\beta}} \overset{\circ}{\tau^{\beta}}_{n+1} + \Delta t \sum_{\beta} q^{\alpha\beta} \frac{\partial g^{\beta}}{\partial \theta} \overset{\circ}{\theta}_{n+1} \tag{5.11}$$

Solving the above set of equations for $\overset{\circ}{s^{\alpha}}_{n+1}$ results in:

$$\overset{\circ}{s^{\alpha}}_{n+1} = \sum_{\beta} m^{\alpha\beta} \overset{\circ}{\tau^{\beta}}_{n+1} + \upsilon_1^{\alpha} \overset{\circ}{\theta}_{n+1} + \upsilon_2^{\alpha} \tag{5.12}$$

where $m^{\alpha\beta}$, υ_1^{α} and υ_2^{α} are constants. It is further known that $\tau^{\beta} = \check{\boldsymbol{T}} \bullet \boldsymbol{S}_0^{\alpha}$; design-differentiation of this relation results in $\overset{\circ}{\tau^{\beta}} = \overset{\circ}{\check{\boldsymbol{T}}} \bullet \boldsymbol{S}_0^{\alpha}$. Note that $\boldsymbol{S}_0^{\alpha}$ is a constant as it is expressed in the plastically deformed configuration which has the same crystal orientation as in the reference configuration. Substituting this relation into Eq. (5.12) results in the desired linear relation:

$$\left\{ \overset{\circ}{s}_{n+1} \right\} = \left[\frac{Ds}{D\tau} \right] : \overset{\circ}{\check{\boldsymbol{T}}} + \{\upsilon_1\} \overset{\circ}{\theta} + \{\upsilon_2\} \tag{5.13}$$

where $\left[\frac{Ds}{D\tau}\right]$ is a 3^{rd} order tensor and υ_1, υ_2 are vectors.

Computing the linear relation between $\overset{\circ}{\boldsymbol{F}^p}_{n+1}$ and $(\overset{\circ}{\check{\boldsymbol{T}}}_{n+1}, \overset{\circ}{\theta}_{n+1})$

The evolution equation for $\overset{\circ}{\boldsymbol{F}^p}$ is evaluated, by design-differentiating Eq. (4.18), as:

$$\frac{\partial \overset{\circ}{\boldsymbol{F}^p}}{\partial t} = \boldsymbol{L} \overset{\circ}{\boldsymbol{F}^p} + \overset{\circ}{\boldsymbol{L}} \boldsymbol{F}^p \tag{5.14}$$

where $\overset{\circ}{\boldsymbol{L}} = \sum_{\alpha} \left[\overset{\circ}{\dot{\gamma}^{\alpha}} \boldsymbol{S}_0^{\alpha} \right]$ can be computed as,

$$\overset{\circ}{\boldsymbol{L}} = \sum_{\alpha} \left[\frac{\partial \dot{\gamma}^{\alpha}}{\partial \tau^{\alpha}} \overset{\circ}{\tau^{\alpha}} + \frac{\partial \dot{\gamma}^{\alpha}}{\partial s^{\alpha}} \overset{\circ}{s^{\alpha}} + \frac{\partial \dot{\gamma}^{\alpha}}{\partial \theta} \overset{\circ}{\theta} \right] \boldsymbol{S}_0^{\alpha} \tag{5.15}$$

Euler-backward integration of Eq. (5.14), with Eqs. (5.13), (5.15) and the earlier definition of $\overset{\circ}{\tau}^{\alpha}$ results in the following:

$$\overset{\circ}{\boldsymbol{F}}{}^{p}_{n+1}(\boldsymbol{F}^{p}_{n+1})^{-1} \;=\; \boldsymbol{E} \;+\; \mathcal{F}\left[\overset{\circ}{\check{\boldsymbol{T}}}_{n+1}\right] \;+\; \boldsymbol{G}\,\overset{\circ}{\theta}_{n+1} \tag{5.16}$$

where $\boldsymbol{E}$, $\boldsymbol{G}$ are constant second-order tensors and $\mathcal{F}$ is a fourth-order tensor. Furthermore, $\overset{\circ}{\check{\boldsymbol{T}}}_{n+1}$ is related to $\overset{\circ}{\boldsymbol{F}}{}^{e}_{n+1}$ and $\overset{\circ}{\theta}_{n+1}$ as (by design differentiating Eq. (4.24)):

$$\overset{\circ}{\check{\boldsymbol{T}}} = \left(\frac{\partial \boldsymbol{\mathcal{L}}^{e}}{\partial\theta}\right)\left[\check{\boldsymbol{E}}^{e}\right]\;\overset{\circ}{\theta} \;+\; \boldsymbol{\mathcal{L}}^{e}\left[\mathrm{Sym}\left(\boldsymbol{F}^{eT}\;\overset{\circ}{\boldsymbol{F}}{}^{e}\right)\right] \tag{5.17}$$

where $\boldsymbol{\mathcal{L}}^{e}$, the fourth-order anisotropic elasticity tensor, is assumed to be a function of temperature only. Using Eqs. (5.16) and (5.17), one can further obtain $\overset{\circ}{\boldsymbol{F}}{}^{p}{}_{n+1}(\boldsymbol{F}^{p}_{n+1})^{-1}$ as a function of $\overset{\circ}{\boldsymbol{F}}{}^{e}_{n+1}$ and $\overset{\circ}{\theta}_{n+1}$.

Computing the linear relation between $\overset{\circ}{\boldsymbol{F}}{}^{e}{}_{n+1}$ and $(\overset{\circ}{\boldsymbol{F}}_{n+1}, \overset{\circ}{\theta}_{n+1})$

Starting from the multiplicative decomposition of the deformation gradient, one can write $\overset{\circ}{\boldsymbol{F}}_{n+1}=\overset{\circ}{\boldsymbol{F}}{}^{e}_{n+1}\boldsymbol{F}^{p}_{n+1} + \boldsymbol{F}^{e}_{n+1}\,\overset{\circ}{\boldsymbol{F}}{}^{p}_{n+1}$, which can then be simplified to,

$$\left(\boldsymbol{F}^{e}_{n+1}\right)^{-1}\left(\overset{\circ}{\boldsymbol{F}}_{n+1}\;\boldsymbol{F}^{-1}_{n+1}\right)\boldsymbol{F}^{e}_{n+1} = \left(\boldsymbol{F}^{e}_{n+1}\right)^{-1}\;\overset{\circ}{\boldsymbol{F}}{}^{e}_{n+1} + \overset{\circ}{\boldsymbol{F}}{}^{p}_{n+1}\left(\boldsymbol{F}^{p}_{n+1}\right)^{-1} \tag{5.18}$$

Substitution of the linear relationship between $\overset{\circ}{\boldsymbol{F}}{}^{p}_{n+1}$ and $[\overset{\circ}{\boldsymbol{F}}{}^{e}_{n+1},\;\overset{\circ}{\theta}_{n+1}]$ results in the desired linear relationship:

$$\overset{\circ}{\boldsymbol{F}}{}^{e}_{n+1} = \boldsymbol{\mathcal{C}}'\left(\boldsymbol{V}_{n+1}\right)\left[\overset{\circ}{\boldsymbol{F}}_{n+1}\right] + \boldsymbol{H}\left(\boldsymbol{V}_{n+1}, \overset{\circ}{\boldsymbol{V}}_{n}\right) + \boldsymbol{M}\left(\boldsymbol{V}_{n+1}\right)\overset{\circ}{\theta}_{n+1} \tag{5.19}$$

where $\boldsymbol{H}$ and $\boldsymbol{M}$ are known second-order tensor functions and $\boldsymbol{\mathcal{C}}'$, a known fourth-order tensor function. The relationship between $\overset{\circ}{\boldsymbol{T}}_{n+1}$ and $[\overset{\circ}{\boldsymbol{F}}_{n+1}, \overset{\circ}{\theta}_{n+1}]$ is obtained by design differentiating Eq. (4.22):

$$\begin{aligned}\overset{\circ}{\boldsymbol{T}} \;&=\; -\mathrm{tr}\left(\overset{\circ}{\boldsymbol{F}}{}^{e}\,(\boldsymbol{F}^{e})^{-1}\right)\boldsymbol{T} + \frac{1}{\det(\boldsymbol{F}^{e})}\;\overset{\circ}{\boldsymbol{F}}{}^{e}\;\check{\boldsymbol{T}}\boldsymbol{F}^{eT} \\ &+\; \frac{1}{\det(\boldsymbol{F}^{e})}\boldsymbol{F}^{e}\;\overset{\circ}{\check{\boldsymbol{T}}}\;\boldsymbol{F}^{eT} + \frac{1}{\det(\boldsymbol{F}^{e})}\boldsymbol{F}^{e}\check{\boldsymbol{T}}\overset{\circ}{\boldsymbol{F}}{}^{e\,T}\end{aligned} \tag{5.20}$$

Substitution of the linear relation between $\overset{\circ}{\boldsymbol{F}}{}^{e}_{n+1}$ and $[\overset{\circ}{\boldsymbol{F}}_{n+1},\ \overset{\circ}{\theta}_{n+1}]$ in Eq. (5.20), results in a linear relation between $\overset{\circ}{\boldsymbol{T}}_{n+1}$ and $[\overset{\circ}{\boldsymbol{F}}_{n+1},\ \overset{\circ}{\theta}_{n+1}]$. This can be converted in terms of the PK I stress as,

$$\begin{aligned}\overset{\circ}{\boldsymbol{P}} &= \mathrm{tr}\left(\overset{\circ}{\boldsymbol{F}}_{n+1}\,\boldsymbol{F}^{-1}_{n+1}\right)\det\boldsymbol{F}_{n+1}\boldsymbol{T}\boldsymbol{F}^{-T}_{n+1} + \det\boldsymbol{F}_{n+1}\,\overset{\circ}{\boldsymbol{T}}\,\boldsymbol{F}^{-T}_{n+1} \\ &- \det\boldsymbol{F}_{n+1}\boldsymbol{T}\boldsymbol{F}^{-T}_{n+1}\overset{\circ}{\boldsymbol{F}}{}^{T}_{n+1}\boldsymbol{F}^{-T}_{n+1} \end{aligned} \tag{5.21}$$

From these equations, one can generate the constants in Eq. (5.9) and use this in the solution of the sensitivity kinematic problem.

5.1.3 Sensitivity of macro-properties

Finally, once the sensitivity micro-problem (Eq. (5.8)) is solved for stress sensitivities in the microstructure due to a perturbation in the process parameter (strain rates), the macro-stress sensitivities ($\frac{\partial\bar{\boldsymbol{T}}}{\partial\alpha_i}$) need to be calculated from Eq. (5.4) to drive the gradient optimization problem. This requires calculation of sensitivities of homogenized PK-1 stress using microstructure-average of the sensitivity fields using Eq. 5.5. This is followed by conversion of sensitivity of PK-1 stress to sensitivity of homogenized Cauchy stress using the homogenized counterpart of Equation 5.21. Sensitivity of the equivalent stress is then evaluated as,

$$\overset{\circ}{\bar{\sigma}}_{eff} = \frac{3}{2\bar{\sigma}_{eff}}\bar{\boldsymbol{T}}' \cdot \overset{\circ}{\bar{\boldsymbol{T}}}' \tag{5.22}$$

The design examples as presented in the next section aim to control equivalent stresses over the deformation history of the material through design of strain rates ($\boldsymbol{\alpha}$). Gradients of the desired property ($\chi^i = \bar{\sigma}_{eff}(t = t_i), i = 1, .., N_s$) with respect to each process parameter α_j is then calculated using Eq. (5.4) and used in the gradient optimization algorithm which converges to an optimum value of the process parameter $\boldsymbol{\alpha}$ over a few iterations.

5.2 Numerical examples

We present design examples where the equivalent stress history of complex 2D microstructures are controlled by designing the deformation strain rates in single (example 1) and two-stage (example 2) processes.

Example 1: Design for desired plastic response under a combination of process modes.

Two 2D microstructures (Fig. 5.1(a,b)) (from now on referred to as microstructures A and B, respectively) with 151 and 162 grains, respectively generated using a standard voronoi construction and meshed using OOF-2 (2004) is employed in the design examples. Microstructure A is meshed using 3989 quadrilateral elements and microstructure B is meshed using 4200 quadrilateral elements. The mesh conforms to grain boundaries such that each element is fully within a particular grain. An initial random ODF is assigned to these microstructures as shown in the pole figures in Fig. 5.1(c,d) corresponding to microstructures A and B, respectively. Aim of this example is to demonstrate the technique for obtaining desired equivalent stress response in microstructure A by controlling a combination of process modes applied on the microstructure. Sensitivities are computed with a perturbation of $\Delta\boldsymbol{\alpha}_i = 1E-5$ for each process mode i. Thus, optimization is comprised of one direct and three sensitivity problems. The optimization problem is executed until the objective function becomes less than $1E-3$ or if the objective function normalized with the initial objective showed less than $1E-4$ improvement between iterations. The response is computed for a total time of 11 seconds with a total of 200 time steps.

The desired response is shown in Fig. 5.2(a) and is assumed to occur during

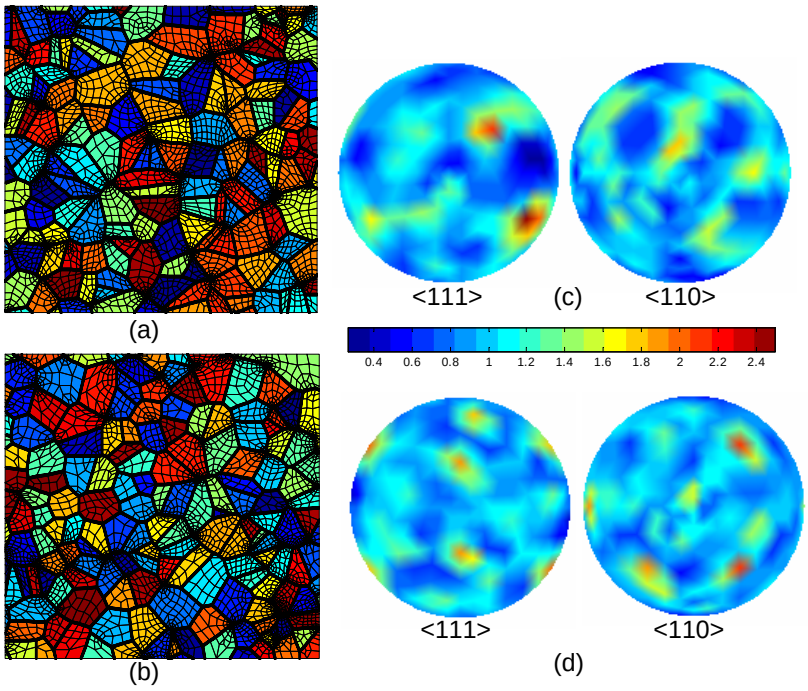

Figure 5.1: Initial microstructure for the design problems. (a) Microstructure A with 151 grains (b) Microstructure B with 162 grains. Initial random texture depicted using the $< 110 >$ and $< 111 >$ pole figures for microstructure A in (c) and microstructure B in (d).

a single processing stage with unknown velocity gradient. Through optimization, we desire to identify the velocity gradient applied on the microstructure. The desired response for the microstructure under consideration is assumed to be a simple cubic curve with equivalent stress vs time characteristics of 30 MPa at 0.5 sec, 40 MPa at 3 sec, 47.5 MPa at 7 sec, and 55 MPa at 11 sec of deformation as shown in Fig. 5.2(a). Initial guess strain rate of 5E-4 is given to all three process modes of shear, rotation and plane strain compression, i.e. a vector of $\boldsymbol{\alpha} = [5e-4, 5e-4, 5e-4]$ is used in the first iteration. The response obtained in the first iteration, two intermediate iterations and the final iteration are shown in Fig. 5.2(b). The desired response is obtained with a converged mean square error (Eq. (5.3)) of 0.51 and final parameters are found as $\boldsymbol{\alpha} = [1.66E-3, 8.42E-$

$3,5E-4]$. Fig. 5.2(d) shows rapid convergence of the objective function with increasing number of iterations showing the numerical efficiency of the algorithm. Final microstructure at a time of 11 sec is shown in Fig. 5.2(c). Initially each grain was assigned a unique orientation. During deformation, misorientation develops within grains leading to spread of orientations and development of strong intragranular texture. The misorientation development can be visualized using the change in neo-eulerian angle of rotation $\xi(t)$ at time t from the values of $\xi(t=0)$ of the initial texture. ξ is obtained from the Rodrigues parametrization given by $\boldsymbol{r} = \boldsymbol{n}\tan(\frac{\xi}{2})$ where $\boldsymbol{n}$ denotes the axis of rotation. The change in the neo-eulerian angle from the initially assigned orientation of grains shown in Fig. 5.2(c) clearly shows the formation of disoriented regions within grains at moderate deformation.

Example 2: Design of desired second stage microstructure response in two-stage processes with unloading and development of residual stresses.

The same model can be extended towards control in a multi-stage set up where a sequence of process modes can be designed to achieve desired response in the processed microstructure. A crucial aspect in multi-stage simulation is an accurate model of mechanics in-between stages. This phase consists of removal of loads from the microstructure and development of residual stresses. The unloading process here is modelled as a non-linear (finite deformation) elasto-static boundary value problem. If $\mathcal{B}$ represents the final configuration of the workpiece at the end of the loading phase with the total deformation gradient given as $\boldsymbol{F}_{n+1} = \boldsymbol{F}^e\boldsymbol{F}^p$, then the solution to the unloading process results in the final body configuration ($\mathcal{B}_u$) with the total deformation gradient after unloading given as $\boldsymbol{F}_u = \boldsymbol{F}^e_u\boldsymbol{F}^p$.

In this work, two assumptions are made to model unloading: firstly, no crystal reorientation is assumed to occur on unloading and secondly, no recovery (or evo-

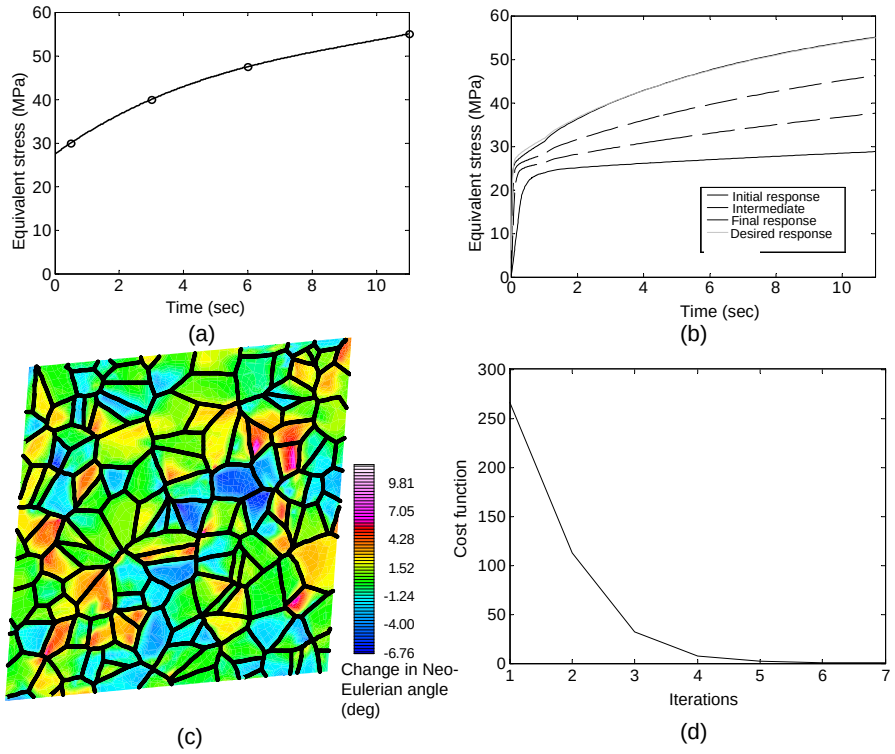

Figure 5.2: Design for desired material response (a) Desired response of the material given by a smooth cubic interpolation of 4 desired coordinates. (b) Change in the microstructure response over various iterations of the optimization problem. (c) Final microstructure at time t = 11 sec of the design solution with mis-orientation distribution over grains (d) Change in objective function over various design iterations of gradient minimization algorithm,

lution of state) is assumed to occur. Microstructure proceeds from one stage to another stage immediately upon completion of the unloading process. For design problems involving the unloading stage, we need to consider the sensitivity of a finite deformation elasto-static problem. The sensitivity constitutive problem is modified and the material deformation behavior treated as elastic in the unloading phase. During the unloading process, we assume for simplicity that the bottom edge of the microstructure is fixed to prevent motion in the normal direction.

Microstructure B is used in this example. A perturbation of 1E-5 is applied

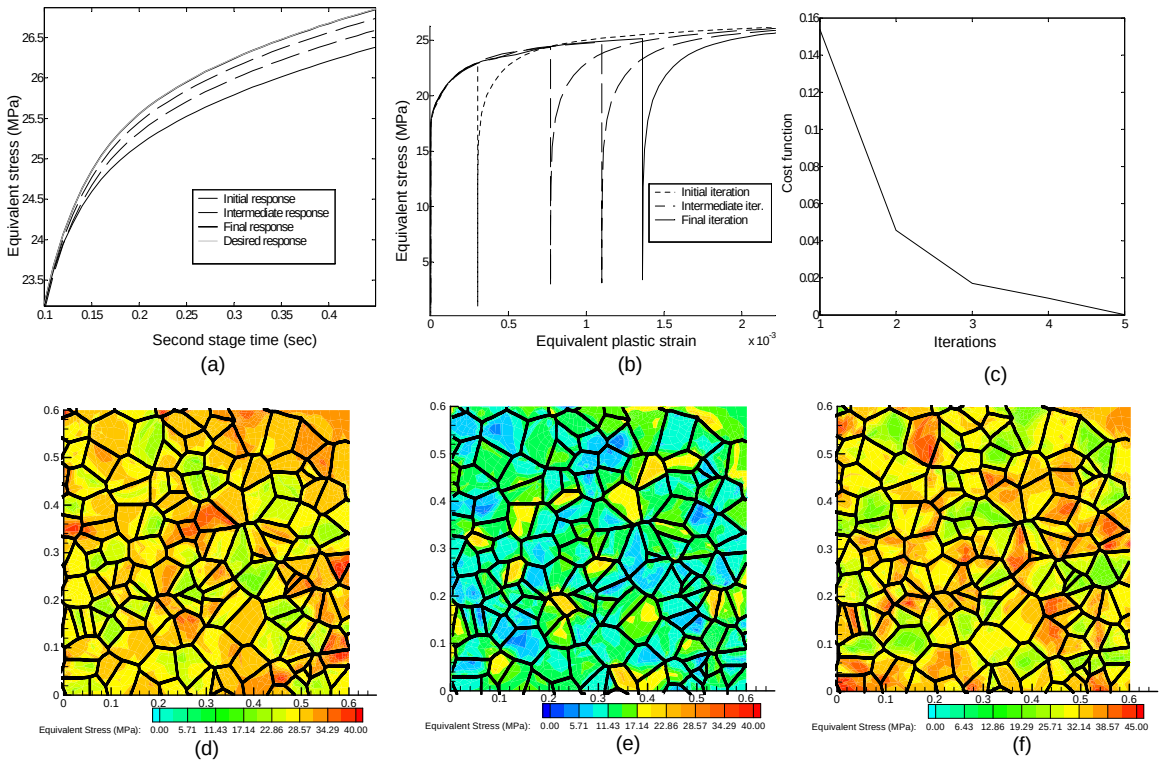

Figure 5.3: (a) Desired response in the second stage and response obtained at various design iterations. (b) Microstructure response in the first deformation stage at various design iterations. (c) Change in objective function over various design iterations of gradient minimization algorithm. (d) Equivalent stress distribution (at final design solution) at the end of first deformation stage (time t = 1 sec). (e) Residual equivalent stress distribution after unloading at the end of first stage. (f) Equivalent stress distribution at the microstructure at time t = 0.45 sec of the second stage (plane strain compression).

to the strain rate in the first stage. Sensitivity of residual stresses after unloading in the first stage are transferred to the second stage. Aim of this example is to demonstrate the technique for obtaining desired initial microstructure response after unloading from a process by controlling the strain rate of initial loading. Unloading produces a heterogeneous distribution of residual stresses in the microstructure. High residual stresses are displayed by grains in the vicinity of grains that displayed high stresses at the end of first stage as seen by comparing residual

stress distribution in Fig. 5.3(e) and the final stress state at the end of first stage in Fig. 5.3(d). The second stage response is not only affected by the heterogeneity of residual stresses but also due to changes in texture and slip system resistance (state variable) distribution at the start of second stage.

By controlling the strain rates used in the first stage, parameters such as initial texturing and state variable at the start of the second stage are also controlled. Numerical experiments reveal that the state variable distribution at the end of the first stage is a dominant factor in determining the material response at the second stage. Response shown in Fig. 5.3(a) corresponds to the desired equivalent stress-time curve in the second stage under plane strain compression of the microstructure at a strain rate of 5E-3 mm/s. The velocity gradient applied to the microstructure in the first stage (simple shear) is unknown and is taken as the design variable. Initial guess strain rate of 5E-4 s^{-1} is given to the first stage, i.e. a vector of $\boldsymbol{\alpha} = [0, 5e-4, 5e-4]$ is employed.

After optimization, the optimal first loading stage strain rates were found as $\boldsymbol{\alpha} = [0, 1.442E-3, 1.442E-3]$ resulting in a response which was within a mean square error of $1E-6$ from the desired response. Equivalent stress field of the microstructure before and after unloading (initial state for the second stage) and after 0.45 sec of second stage are presented in Fig. 5.3(d,e and f), respectively. Fig. 5.3(a-b) shows evolution of the response at various iterations of the optimization algorithm and Fig. 5.3(c) shows rapid convergence of the objective function with increasing number of iterations again demonstrating the numerical efficiency of the design algorithm. For all examples in this chapter, solution process was accelerated by parallelizing the program using MPI. The simulator was developed using object oriented programming ($C++$) and linked to the PetSc toolbox for

parallel assembly and solution of linear systems arising in the direct and the sensitivity problems. In the future, we plan to include techniques such as domain decomposition and adaptive remeshing techniques to further increase the efficiency and fidelity of 3D microstructure design simulations.

5.3 Conclusions

The problem of microstructure design is attempted using a novel continuum sensitivity analysis of homogenization. This involves differentiation of the governing field equations of homogenization with respect to the processing parameters and development of the weak forms for the corresponding sensitivity equations that are solved using finite element analysis. The technique is applied to identify optimal strain rates in single and multi-stage processes (with intermediate unloading stages) that would lead to a desired microstructure response. The algorithm is computationally efficient and is found to converge to the desired response within a few iterations. This analysis shows that there is a definite merit in further extending these approaches towards design of industrial forming processes so that components with desired stiffness or strength properties are obtained. The multi-scaling procedures involved are described in the next chapter, in a preliminary study based on the Taylor model.

Chapter 6

A multilength scale continuum sensitivity analysis for the control of texture-dependent properties in deformation processing

An efficient multi-scale technique for controlling texture development is presented in this section that allows tailoring properties in forming processes involving polycrystalline materials. This chapter is a culmination of the analysis developed in the previous chapters, where the tools developed are used for controlling the effect of macroscopic variables such as die and preform shapes on micro-scale features such as the crystallographic texture. The approach presented in this chapter uses continuum representation of texture over Rodrigues-Frank space for computing texture evolution at each integration point in the macro-simulation. A multi-length scale finite element simulator has been developed [90] that allows for crystal elasto-viscoplasticity and simulation of texturing in large deformation forming processes. Sensitivity of microstructure field variables such as slip resistances and texture due to perturbations in forming parameters such as forging rates, die shapes and preform shapes are calculated using a novel two-scale sensitivity analysis. An averaging principle is then developed to compute sensitivity of stress and various material properties at the macroscopic level. These sensitivities are used within a gradient-based optimization framework for computational design of metal forming processes. Effectiveness of the developed finite element analysis and design techniques are demonstrated in this chapter using numerical examples involving control of Young's modulus and yield strength variability in finished products.

6.1 Total Lagrangian approach for modelling texture evolution

For accurately modeling the response of polycrystals undergoing deformation, one needs to be able to accurately represent polycrystals. The most common technique for representing polycrystals is based on the use of a collection of discrete grains/orientations. Such an approach needs the choice of the grain orientations to accurately represent the texture in the material. The emphasis in this chapter is on a continuum representation of polycrystals, based on the pioneering work of [30, 31, 91]. A brief summary of the continuum representation of polycrystals is provided for clarity of future developments. Consider a macroscopic material point and let it be associated with the underlying microstructure $\mathcal{M}$. Assume that the response of any crystal of the polycrystal is determined only by its orientation $\boldsymbol{R}$, which is the rotation relating the crystal lattice frame, $\hat{\boldsymbol{e}}_i$, to a sample reference frame $\boldsymbol{e}_i$ as $\boldsymbol{e}_i = \boldsymbol{R}\,\hat{\boldsymbol{e}}_i$. The orientation $\boldsymbol{R} \in \mathcal{O}^+$ is not unique because of crystal symmetries. This non-uniqueness has traditionally been resolved by restricting the choice of orientation to a fundamental region of $\mathcal{O}^+$. Thus for a particular choice of the fundamental region $\mathcal{R}$, the orientation of the crystal is uniquely represented by $\boldsymbol{r} \in \mathcal{R}$ where

$$\boldsymbol{R} = \mathcal{Q}(\boldsymbol{r}) \tag{6.1}$$

and $\mathcal{Q}$ maps the orientation space to the set of all proper orthogonal tensors. The notion of crystals being interchangeable with unique parameterized orientations is developed in [31]. This is then used to define texture as a map of crystals to orientations within the fundamental region. A microstructure, $\mathcal{M}$, is then associated with a collection of such mappings, $\boldsymbol{\Phi}$, so that each map, $\chi \in \boldsymbol{\Phi}$, is a one-to-one mapping of the microstructure $\mathcal{M}$ onto the fundamental region $\mathcal{R}$. Further, the

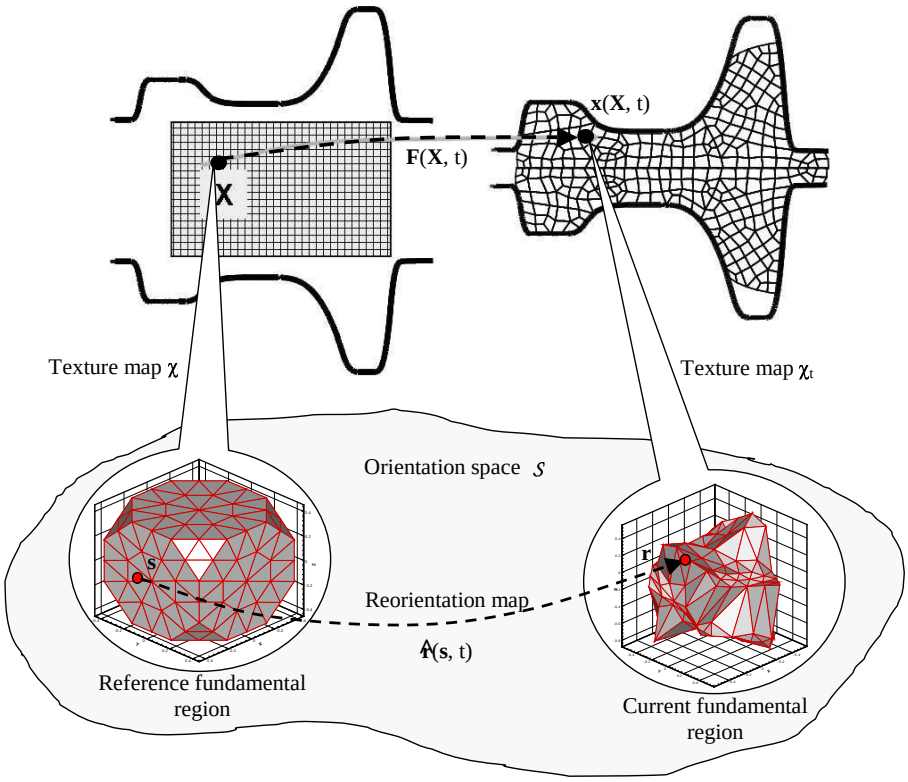

Figure 6.1: A Lagrangian framework describing the association of a polycrystal, at a material point $\boldsymbol{X}$, with unique parameters $\boldsymbol{s}$ and $\boldsymbol{r}$, drawn from the fundamental region. Also shown is the reorientation vector $\hat{\boldsymbol{r}}(\boldsymbol{s}, t)$.

orientation of a crystal, $\boldsymbol{r}$, is developed as

$$\boldsymbol{r} \;=\; \chi(\boldsymbol{p}) \tag{6.2}$$

where $\boldsymbol{p}$ represents the crystals associated with the microstructure $\mathcal{M}$. A graphical representation of this framework is shown in Figure 6.1. Through such a description, microstructure is treated as a continuum of crystals, that under the map χ occupies a fundamental region of the orientation space. The ODF, represented as $\mathcal{A}(\boldsymbol{r})$, describes the crystal density over the fundamental region. The ODF is defined so that the crystal volume fraction for any part $\mathcal{M}^* \subseteq \mathcal{M}$,

$$v_f(\mathcal{M}^*) \;=\; \int_{\chi(\mathcal{M}^*)} \mathcal{A}(\boldsymbol{r}) dv \tag{6.3}$$

is independent of the map χ. dv is the volume element on the reference fundamental region. $\mathcal{M}$ can also be associated with a family of maps χ_t which take a crystal to the fundamental region $\mathcal{R}_t$. Such a description helps in modeling time dependent texturing. Let χ be the reference map and correspondingly $\mathcal{R}$ is the reference fundamental region. The family of maps χ_t along with the reference map χ determine a family of mappings $\hat{\boldsymbol{r}}(\bullet, t) : \mathcal{R} \rightarrow \mathcal{R}_t$ referred to as the re-orientation, and given by (see Figure 6.1)

$$\hat{\boldsymbol{r}}(\boldsymbol{s}, t) = \chi_t(\chi^{-1}(\boldsymbol{s})) \tag{6.4}$$

The re-orientation vector, $\hat{\boldsymbol{r}}$, is associated with the one-parameter family of ODF's, $\mathcal{A}(\boldsymbol{r}, t) = \mathcal{A}_{\chi_t}(\boldsymbol{r}) = \mathcal{A}(\hat{\boldsymbol{r}}(\boldsymbol{s}, t), t) = \hat{\mathcal{A}}(\boldsymbol{s}, t)$. The representation of the ODF given by $\mathcal{A}(\boldsymbol{r}, t)$ is Eulerian and $\hat{\mathcal{A}}(\boldsymbol{s}, t)$ is Lagrangian.

Consider the integral conservation equation, Equation (6.3). Applying this conservation equation to arbitrary parts $\mathcal{M}^* \subseteq \mathcal{M}$ under maps χ and χ_t, followed by a transformation of variables to the reference fundamental region, results in the following

$$\int_{\chi(\mathcal{M}^*)} \Big(\hat{\mathcal{A}}(\boldsymbol{s}, t)\ J(\boldsymbol{s}, t) - \hat{\mathcal{A}}(\boldsymbol{s}, 0) \Big)\ dv = 0 \tag{6.5}$$

where $J(\boldsymbol{s}, t) = \det(\nabla \hat{\boldsymbol{r}}(\boldsymbol{s}, t))$ is the Jacobian determinant of the re-orientation of the crystals and $\hat{\mathcal{A}}(\boldsymbol{s}, 0) = \mathcal{A}_0(\boldsymbol{s})$ is the ODF associated with the reference map and can be thought of as the initial texturing of the material. The Lagrangian version of the conservation equation is then defined as [31]

$$\hat{\mathcal{A}}(\boldsymbol{s}, t)\ J(\boldsymbol{s}, t) = \hat{\mathcal{A}}(\boldsymbol{s}, 0) = \mathcal{A}_0(\boldsymbol{s}) \tag{6.6}$$

In such a Lagrangian framework, the re-orientation, $\hat{\boldsymbol{r}}$, has to be evaluated from the re-orientation velocity $\hat{\boldsymbol{v}}(\boldsymbol{s}, t) = \boldsymbol{v}(\hat{\boldsymbol{r}}(\boldsymbol{s}, t), t) = \boldsymbol{v}(\boldsymbol{r}, t)$ through the following relation

$$\frac{\partial \hat{\boldsymbol{r}}}{\partial t}(\boldsymbol{s}, t) = \hat{\boldsymbol{v}}(\boldsymbol{s}, t) \tag{6.7}$$

Texture evolution is thus modeled by an ODF at each of the material points of the macro-continuum (see Figure 6.1).

For completeness, the neo-Eulerian parametrization of $\boldsymbol{R}$ is also briefly described. The parametrization of $\boldsymbol{R}$ is derived from the natural invariants of $\boldsymbol{R}$: the axis of rotation $\boldsymbol{n}$ and the angle of rotation ξ. The angle-axis parametrization, $\boldsymbol{r}$, is obtained by scaling the axis $\boldsymbol{n}$ by a function of the angle ξ as $\boldsymbol{r} \;=\; \boldsymbol{n}\; f(\xi)$. In the particular case of Rodrigues' parametrization, the function is defined as $f(\xi) \;=\; \tan\left(\frac{\xi}{2}\right)$. In this case, the orientation $\boldsymbol{R}$ is related to the parametrization $\boldsymbol{r}$ as

$$\boldsymbol{R} \;=\; \mathcal{Q}(\boldsymbol{r}) \;=\; \frac{1}{(1+\boldsymbol{r}_{\bullet}\,\boldsymbol{r})}\left\{\boldsymbol{I}(1-\boldsymbol{r}_{\bullet}\,\boldsymbol{r})+2(\boldsymbol{r}\otimes\boldsymbol{r}\;+\;\boldsymbol{I}\times\boldsymbol{r})\right\} \tag{6.8}$$

where $\boldsymbol{I}$ is the second order identity tensor and $\otimes$ denotes the tensor product of the two quantities. The ODF, in the present work, is approximated with finite element polynomial functions defined over an explicit discretization of the orientation space based on Rodrigues' parametrizations. The Rodrigues' parametrization was chosen over pole figures or Euler angle spaces because of its several advantages, discussed in detail in [30]. In fact, if the initial texturing is known, and the re-orientation of the crystal orientations is computed during deformation, then the current mapping or the current Lagrangian ODF can be evaluated using Equation (6.6). The polycrystal average of an orientation dependent property, $\boldsymbol{\Upsilon}(\boldsymbol{r},t)$, is determined as:

$$\begin{aligned}\langle\boldsymbol{\Upsilon}\rangle \;&=\; \int_{\mathcal{R}_t}\boldsymbol{\Upsilon}(\boldsymbol{r},t)\;\mathcal{A}(\boldsymbol{r},t)\;dv_t \\ &=\; \int_{\mathcal{R}}\boldsymbol{\Upsilon}(\hat{\boldsymbol{r}}(\boldsymbol{s},t),t)\;\mathcal{A}_0(\boldsymbol{s})\;dv\end{aligned} \tag{6.9}$$

where dv_t is defined as the volume element on the current fundamental region. From Equation (6.9), one can conclude that if the re-orientation and the initial texture are known, then the average property for the polycrystal can be evaluated.

6.2 Rate independent constitutive problem

During a deformation process, crystallographic slip and re-orientation of crystals (lattice rotation) can be assumed to be the primary mechanisms of plastic deformation. The slip and re-orientation occur in an ordered manner such that a preferential orientation or texture develops. We follow the rate-independent constitutive model developed in [57] and build on it by developing compact representation of consistent tangent moduli for use in implicit large deformation formulation. Consider a point on the reference fundamental region and this corresponds to a particular crystal orientation. In an appropriate kinematic framework, such as the one introduced in Ref. [92] for large deformation inelastic analysis, the total deformation gradient is decomposed into plastic and elastic parts as follows (Figure 6.2):

$$\boldsymbol{F} = \boldsymbol{F}^e \ \boldsymbol{F}^p \tag{6.10}$$

where $\boldsymbol{F}^e$ is the elastic deformation gradient and $\boldsymbol{F}^p$, the plastic deformation gradient, with $\det\boldsymbol{F}^p = 1$. In this analysis, the Taylor hypothesis is utilized as the macro-micro linking assumption. As a result of this assumption, the crystal deformation gradient (in the sample reference frame) is taken to be the same as the macroscopic deformation gradient.

In the following scheme, all vector and tensorial quantities are expressed in the reference sample frame, i.e., the initial (macro-scale) configuration. Crystal specific properties like the stiffness and compliance are transformed to the sample reference frame for each crystal using the position $\boldsymbol{r}$ in the orientation space. In the constitutive equations to be defined below, the Green elastic strain measure is defined on the relaxed configuration (plastically deformed, unstressed configuration) $\bar{\mathcal{B}}$. It is represented as $\check{\boldsymbol{E}}^e = \frac{1}{2}\left(\boldsymbol{F}^{eT}\boldsymbol{F}^e - \boldsymbol{I}\right)$. The conjugate stress measure

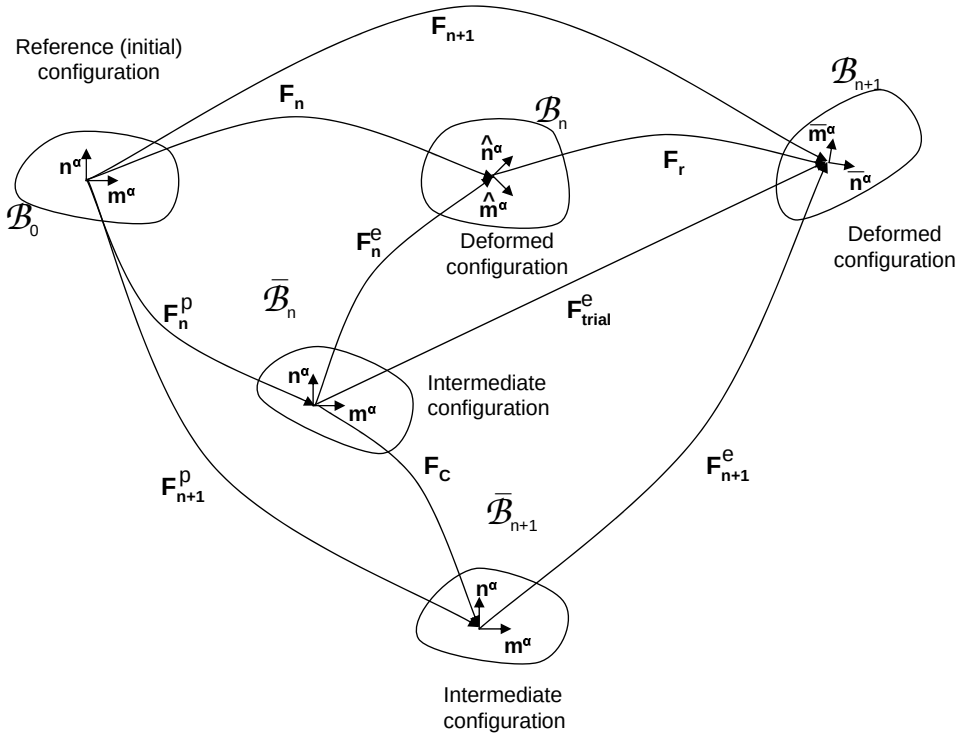

Figure 6.2: Schematic of the various material configurations, for a single crystal, used in the integration of the constitutive model. $\boldsymbol{m}^\alpha$ denotes the slip direction and $\boldsymbol{n}^\alpha$ denotes the slip normal. These together define the slip systems and are assumed to be known on the reference (initial) configuration. The Schmid tensor is evaluated as $\boldsymbol{S}_0^\alpha = \boldsymbol{m}^\alpha \otimes \boldsymbol{n}^\alpha$. $\hat{\boldsymbol{m}}^\alpha$, $\bar{\boldsymbol{m}}^\alpha$ are the slip directions in the deformed configurations (different from $\boldsymbol{m}^\alpha$ because of crystal re-orientation). Similarly, $\hat{\boldsymbol{n}}^\alpha$ and $\bar{\boldsymbol{n}}^\alpha$ are the slip normals in the deformed configurations $\mathcal{B}_n$ and $\mathcal{B}_{n+1}$, respectively. $\boldsymbol{F}_r$ is the relative deformation gradient from $\mathcal{B}_n$ to $\mathcal{B}_{n+1}$.

is then defined as $\bar{\boldsymbol{T}} = \det\boldsymbol{F}^e(\boldsymbol{F}^e)^{-1}\boldsymbol{T}(\boldsymbol{F}^e)^{-T}$ where $\boldsymbol{T}$ is the Cauchy stress for the crystal in the sample reference frame. It is assumed that deformation takes place through dislocation glide and the evolution of the plastic flow is given by

$$\boldsymbol{L}^p = \dot{\boldsymbol{F}}^p(\boldsymbol{F}^p)^{-1} = \sum_\alpha \dot{\gamma}^\alpha \boldsymbol{S}_0^\alpha sign(\tau^\alpha) \tag{6.11}$$

where $\boldsymbol{S}_0^\alpha = \boldsymbol{m}^\alpha \otimes \boldsymbol{n}^\alpha$ is the Schmid tensor and $\dot{\gamma}^\alpha$ is the plastic shearing rate on the α^{th} slip system. $\boldsymbol{m}^\alpha$ and $\boldsymbol{n}^\alpha$ are the slip direction and the slip plane normal,

respectively. Fig. 6.2 clearly describes the constitutive problem along with the slip systems in different configurations. An Euler-backward time integration procedure leads to the following approximation:

$$\boldsymbol{F}^p \;=\; \exp(\Delta t \sum_{\alpha} \dot{\gamma}^{\alpha} \boldsymbol{S}_0^{\alpha} sign(\tau^{\alpha}))\boldsymbol{F}_n^p \;\approx\; (\boldsymbol{I} + \sum_{\alpha} \Delta\gamma^{\alpha} \boldsymbol{S}_0^{\alpha} sign(\tau^{\alpha}))\boldsymbol{F}_n^p \quad (6.12)$$

Substituting Eq. (6.12) into Eq. (6.10) results in the following:

$$\boldsymbol{F}^e \;=\; \boldsymbol{F}_{trial}^e(\boldsymbol{I} - \sum_{\alpha} \Delta\gamma^{\alpha} \boldsymbol{S}_0^{\alpha} sign(\tau^{\alpha})) \quad (6.13)$$

where $\boldsymbol{F}_{trial}^e$ is the trial elastic deformation gradient and is given as $\boldsymbol{F}_{n+1}(\boldsymbol{F}_n^p)^{-1}$.

In the constitutive equations to be defined below, the Green elastic strain measure defined on the relaxed configuration (plastically deformed, unstressed configuration) $\bar{\mathcal{B}}$ is utilized. It is computed using Eq. (6.13) as

$$\begin{aligned} \check{\boldsymbol{E}}^e &= \frac{1}{2}\left(\boldsymbol{F}^{eT}\boldsymbol{F}^e - \boldsymbol{I}\right) \\ &= \check{\boldsymbol{E}}_{trial}^e - \frac{1}{2}\sum_{\alpha} sign(\tau^{\alpha})\Delta\gamma^{\alpha}\boldsymbol{B}^{\alpha} \end{aligned} \quad (6.14)$$

where $\check{\boldsymbol{E}}_{trial}^e \;=\; \frac{1}{2}\left((\boldsymbol{F}_{trial}^e)^T\boldsymbol{F}_{trial}^e - \boldsymbol{I}\right)$ and $\boldsymbol{B}^{\alpha} = (\boldsymbol{S}_0^{\alpha})^T(\boldsymbol{F}_{trial}^e)^T\boldsymbol{F}_{trial}^e + (\boldsymbol{F}_{trial}^e)^T\boldsymbol{F}_{trial}^e\boldsymbol{S}_0^{\alpha}$. The conjugate stress measure is then defined as

$$\bar{\boldsymbol{T}} \;=\; \det\boldsymbol{F}^e(\boldsymbol{F}^e)^{-1}\boldsymbol{T}(\boldsymbol{F}^e)^{-T} \quad (6.15)$$

where $\boldsymbol{T}$ is the Cauchy stress for the crystal in the sample reference frame. For future reference, it is stated that all vector and tensorial quantities are expressed in the reference sample frame, i.e., the initial (macro-scale) configuration $\mathcal{B}_0$. Furthermore, crystal specific properties like the stiffness and compliance have to be transformed to the sample reference frame using the crystal orientation $\boldsymbol{r}$. The constitutive relation, for stress, for small temperature changes about the initial temperature, θ_0, is given by

$$\bar{\boldsymbol{T}} \;=\; \boldsymbol{\mathcal{L}}^e\left[\check{\boldsymbol{E}}^e\right] \quad (6.16)$$

where $\boldsymbol{\mathcal{L}}^e$ is the fourth-order anisotropic elasticity tensor expressed in terms of the crystal stiffness parameters and the orientation $\boldsymbol{r}$. Eq. (6.16) further simplifies to the following

$$\bar{\boldsymbol{T}} \;=\; \bar{\boldsymbol{T}}_{trial} \quad - \quad \frac{1}{2}\sum_{\beta} \Delta\gamma^{\beta} \boldsymbol{\mathcal{L}}^e \left[\boldsymbol{B}^{\beta}\right] sign(\boldsymbol{\tau}^{\beta}_{trial}) \tag{6.17}$$

where $\bar{\boldsymbol{T}}_{trial} \;=\; \boldsymbol{\mathcal{L}}^e \left[\check{\boldsymbol{E}}^e_{trial}\right]$. The resolved shear stress $\boldsymbol{\tau}^{\alpha} = \bar{\boldsymbol{T}} \cdot \boldsymbol{S}^{\alpha}_0$ attains a critical value s^{α} on the systems where slip occurs with plastic shearing rate on the α^{th} slip system $\dot{\gamma}^{\alpha} > 0$. Further, the resolved shear stress does not exceed s^{α} on the inactive systems with $\dot{\gamma}^{\alpha} = 0$. A potentially active set $\mathcal{PA}$ of slip systems can be identified initially based on the trial resolved stress as the systems with $|\boldsymbol{\tau}^{\alpha}_{trial}| - s^{\alpha} > 0$.

The hardening law for the slip resistance s^{α} is given as,

$$\dot{s}^{\alpha}(i) = \sum_{\beta} h^{\alpha\beta}\dot{\gamma}^{\beta} \tag{6.18}$$

During plastic flow, the active systems are assumed to follow the consistency condition: $|\tau^{\alpha}| = s^{\alpha}$. Increment in shearing rates $\Delta\gamma^{\beta}$ at each time step is obtained by solving the following equation obtained by resolving Eq. 6.17 along slip directions:

$$|\tau^{\alpha}| = s^{\alpha} = |\tau^{\alpha}_{trial}| - \frac{1}{2}\sum_{\beta} sign(\tau^{\alpha}_{trial}) sign(\tau^{\beta}_{trial}) \Delta\gamma^{\beta} \boldsymbol{\mathcal{L}}^e \left[\boldsymbol{B}^{\beta}\right] \cdot \boldsymbol{S}^{\alpha}_0 \tag{6.19}$$

where, $\alpha, \beta \in \mathcal{PA}$. A system of equations is obtained of the following form,

$$\sum_{\beta \in \mathcal{PA}} A^{\alpha\beta} \Delta\gamma^{\beta} = b^{\alpha} \tag{6.20}$$

where,

$$A^{\alpha\beta} = h^{\alpha\beta} + \frac{1}{2} sign(\boldsymbol{\tau}^{\alpha}_{trial}) sign(\boldsymbol{\tau}^{\beta}_{trial}) \boldsymbol{\mathcal{L}}^e \left[\boldsymbol{B}^{\beta}\right] \cdot \boldsymbol{S}^{\alpha}_0$$
$$b^{\alpha} = |\tau^{\alpha}_{trial}| - s^{\alpha} \tag{6.21}$$

If for any system $\Delta\gamma^{\beta} \leq 0$, then this system is removed from the set of potentially active systems. The system is repeatedly solved until for all systems $\Delta\gamma^{\beta} > 0$. Following this step, the plastic and elastic parts of the deformation gradient are updated using Eq. 6.12 and Eq. 6.10 respectively. Conjugate stress measure, $\bar{\boldsymbol{T}}$ is then obtained from Eq. 6.17, followed by the update of cauchy stress as $\boldsymbol{T} = F^e[det(\boldsymbol{F}^e)]^{-1}\bar{\boldsymbol{T}}(F^e)^T$. The slip resistances are also updated at the end of the time step. Finally, the reorientation velocity is found as follows:

$$\boldsymbol{v} \;=\; \frac{\partial \boldsymbol{r}}{\partial t} \;=\; \frac{1}{2}\left(\boldsymbol{\omega} \;+\; (\boldsymbol{\omega}\cdot\boldsymbol{r})\boldsymbol{r} \;+\; \boldsymbol{\omega}\times\boldsymbol{r}\right) \tag{6.22}$$

where $\boldsymbol{r}$ is the orientation (Rodrigues' parametrization) and $\boldsymbol{\omega}$ represents the spin vector defined as $\boldsymbol{\omega} \;=\; \text{vect}\left(\dot{\boldsymbol{R}}^e\boldsymbol{R}^{eT}\right) \;=\; \text{vect}\left(\boldsymbol{\Omega}\right)$ where $\boldsymbol{R^e}$ is evaluated through the polar decomposition of the elastic deformation gradient $\boldsymbol{F}^e$ as $\boldsymbol{F}^e \;=\; \boldsymbol{R}^e\boldsymbol{U}^e$. Considering the Euler-backward time integration of $\dot{\boldsymbol{R}}^e\boldsymbol{R}^{eT} \;=\; \boldsymbol{\Omega}$, where $\boldsymbol{\Omega}$ is the spin tensor, leads to the following:

$$\boldsymbol{R}^e_{n+1} \;=\; \exp(\Delta t\boldsymbol{\Omega}_{n+1})\boldsymbol{R}^e_n \tag{6.23}$$

and

$$\boldsymbol{\Omega}_{n+1} \;=\; \frac{1}{\Delta t}\ln\left\{\boldsymbol{R}^e_{n+1}\boldsymbol{R}^{eT}_{\;n}\right\} \tag{6.24}$$

From the elastic deformation gradients, $\boldsymbol{R}^e_{n+1}$ and $\boldsymbol{R}^e_n$ are evaluated and one can evaluate the spin tensor $\boldsymbol{\Omega}_{n+1}$ using Equation (6.24) and then the re-orientation velocity from Equation (6.22). Further, post-processing involves computing the average Cauchy stress from

$$\langle\boldsymbol{T}\rangle \;=\; \int_{\mathcal{R}} \boldsymbol{T}(\hat{\boldsymbol{r}}(\boldsymbol{s},t),t)\;\mathcal{A}_0(\boldsymbol{s})\;dv \tag{6.25}$$

From the above equation, it is seen that if the initial texturing is known, and the re-orientation of the crystal orientations is computed during deformation, then the average Cauchy stress can be computed.

6.3 Solution of the kinematic problem

A total Lagrangian framework is adopted for the kinematic problem. The equilibrium equation is expressed on the reference configuration, based on the polycrystal plasticity approach highlighted earlier, as:

$$\nabla_{0\bullet} \langle \boldsymbol{P} \rangle + \boldsymbol{f} = \boldsymbol{0} \tag{6.26}$$

where $\nabla_{0\bullet}$ represents the divergence in the reference/initial configuration (total Lagrangian approach). The polycrystal average Piola-Kirchhoff-I stress, $\langle \boldsymbol{P} \rangle$ is expressed as

$$\begin{aligned} \langle \boldsymbol{P} \rangle &= \langle \det \boldsymbol{F}\ \boldsymbol{T}\ \boldsymbol{F}^{-T} \rangle \\ &= \det \boldsymbol{F}\ \langle \boldsymbol{T} \rangle\ \boldsymbol{F}^{-T} \end{aligned} \tag{6.27}$$

using the Taylor hypothesis for the macro-micro linking assumption. The incremental quasi-static problem is to determine the displacement field or the incremental displacement field that satisfies Equation (6.26). The weak form of this equation, for any kinematically admissible test function $\tilde{\boldsymbol{u}}$, is written as

$$\mathcal{G}(\boldsymbol{u}_{n+1}, \tilde{\boldsymbol{u}}) \equiv \int_{\mathcal{B}_0} \langle \boldsymbol{P} \rangle \bullet \nabla_0 \tilde{\boldsymbol{u}} dV - \int_{\partial \mathcal{B}_0} \boldsymbol{\lambda} \bullet \tilde{\boldsymbol{u}} dA - \int_{\mathcal{B}_0} \boldsymbol{f} \bullet \tilde{\boldsymbol{u}} dV = 0 \tag{6.28}$$

where the applied surface traction $\boldsymbol{\lambda}$ and body forces $\boldsymbol{f}$ are given. It is further assumed that the contact problem is independent of the nature of the underlying microstructure, and that texture plays a role in this equation only through the stress response. To solve this non-linear equation, a Newton-Raphson iterative scheme along with a line search procedure is employed. The linearization process of the micro-averaged PK-I stress is given by:

$$\delta \langle \boldsymbol{P} \rangle = \det \boldsymbol{F} \left(\mathrm{tr}(\delta \boldsymbol{F} \boldsymbol{F}^{-1}) \langle \boldsymbol{T} \rangle - \langle \boldsymbol{T} \rangle \left(\delta \boldsymbol{F} \boldsymbol{F}^{-1} \right)^T + \langle \delta \boldsymbol{T} \rangle \right) \boldsymbol{F}^{-T} \tag{6.29}$$

where $\delta \boldsymbol{T} = \delta(\frac{1}{\det \boldsymbol{F}^e} \boldsymbol{F}^e \bar{\boldsymbol{T}} (\boldsymbol{F}^e)^T)$ requires the evaluation of $\delta \boldsymbol{F}^e$ and $\delta \bar{\boldsymbol{T}}$ using the constitutive model. In order to obtain $\delta \bar{\boldsymbol{T}}$, consider the linearization of Equation (6.17), one obtains:

$$\begin{aligned} \delta \bar{\boldsymbol{T}} &= \boldsymbol{\mathcal{L}}^e \left[\delta \check{\boldsymbol{E}}^e_{trial} \right] - \frac{1}{2} \sum_\beta \operatorname{sgn}(\tau^\beta_{trial}) \delta(\Delta \gamma^\beta) \boldsymbol{\mathcal{L}}^e \left[\boldsymbol{B}^\beta \right] \\ &\quad - \sum_\beta \operatorname{sgn}(\tau^\beta_{trial}) \Delta \gamma^\beta \boldsymbol{\mathcal{L}}^e \left[\boldsymbol{S}_0^{\beta T} \delta \check{\boldsymbol{E}}^e_{trial} + \delta \check{\boldsymbol{E}}^e_{trial} \boldsymbol{S}_0^\beta \right] \end{aligned} \tag{6.30}$$

This computation of $\delta \bar{\boldsymbol{T}}$ requires the evaluation of $\delta(\Delta \gamma^\beta)$, obtained by linearization given by:

$$\delta(\Delta \gamma^\beta) = (A^{\alpha\beta})^{-1} (\delta b^\alpha - \delta A^{\alpha\beta} \Delta \gamma^\beta) \tag{6.31}$$

$$\delta b^\alpha = \operatorname{sgn}(\tau^\alpha_{trial}) \boldsymbol{\mathcal{L}}^e \left[\delta \check{\boldsymbol{E}}^e_{trial} \right] \cdot \boldsymbol{S}_0^\alpha \tag{6.32}$$

$$\delta A^{\alpha\beta} = \operatorname{sgn}(\tau^\alpha_{trial}) \operatorname{sgn}(\tau^\beta_{trial}) \boldsymbol{S}_0^\alpha \cdot \boldsymbol{\mathcal{L}}^e \left[\boldsymbol{S}_0^{\beta T} \delta \check{\boldsymbol{E}}^e_{trial} + \delta \check{\boldsymbol{E}}^e_{trial} \boldsymbol{S}_0^\beta \right] \tag{6.33}$$

Using the definition of $\delta \check{\boldsymbol{E}}^e_{trial} = \operatorname{sym}(\boldsymbol{F}^{eT}_{trial} \delta \boldsymbol{F} \boldsymbol{F}^{p-1}_n)$, the above set of equation yield an implicit form $\delta(\Delta \gamma^\beta) = \boldsymbol{m}^\beta \cdot \delta \boldsymbol{F}$ for use in Eq. 6.30. Next, $\delta \boldsymbol{F}^e$ is obtained from:

$$\delta(\boldsymbol{F}^e) = \delta \boldsymbol{F} (\boldsymbol{F}^p)^{-1} - \boldsymbol{F}^e_{trial} \sum_\beta \operatorname{sgn}(\tau^\beta_{trial}) \delta(\Delta \gamma^\beta) \boldsymbol{S}_0^\beta \tag{6.34}$$

In all of the above analysis, the standard tensorial notation developed in [81] is followed.

6.4 Definition of shape sensitivities

In this section, the shape sensitivities of a field Φ, expressed in an updated Lagrangian (UL) framework, are briefly described. Sensitivities of the deformation and material state are quantitative measures of changes in the deformation and

material state, respectively, as a result of infinitesimal perturbations to variables that define the initial preform shape $\boldsymbol{\beta}_s$ (shape sensitivity) [86]. Typical process parameters include the ram speed history, the die surface and the initial material state among others. Figure 6.3 presents a schematic that shows the variation of various fields induced by a variation in a shape parameter. Even though an updated Lagrangian analysis is considered here, a similar representation can be introduced for the total Lagrangian (TL) formulation with $\mathcal{B}_0$ as the corresponding reference configuration. The variables $\mathbf{Q}$, shown in Figure 6.3, denote the set of material state variables necessary to define the material state and plastic deformation of the workpiece (e.g. $\mathbf{Q} = \{\boldsymbol{F}^e, s, f, \boldsymbol{T}\}$).

A design independent reference material configuration $\mathcal{B}_R$ is introduced and a smooth one-to-one design dependent geometric mapping defined on $\mathcal{B}_R$ results in an initial configuration $\mathcal{B}_0$. The geometric mapping which defines $\mathcal{B}_0$ is described as

$$\boldsymbol{X} \;=\; \bar{\boldsymbol{X}}(\boldsymbol{Y}; \boldsymbol{\beta}_s) \qquad\qquad \forall\; \boldsymbol{Y} \in \mathcal{B}_R \tag{6.35}$$

Note that the initial configuration $\mathcal{B}_0$ varies with the perturbations $\Delta\boldsymbol{\beta}_s$. Therefore one needs to follow the variation of the field for each given particle $\mathbf{Y}$ defined in the configuration $\mathcal{B}_R$, before evaluating the shape derivatives of a field. It is from this configuration that all preforms are obtained via the deformation gradient $\boldsymbol{F}_R$. The dependence of the field $\Phi = \hat{\Phi}(\boldsymbol{x}_n, t)$ on $\boldsymbol{\beta}_s$ can thus be expressed as:

$$\Phi \;=\; \hat{\Phi}(\boldsymbol{x}_n, t; \boldsymbol{\beta}_s) \;=\; \tilde{\Phi}(\boldsymbol{X}, t; \boldsymbol{\beta}_s) \;=\; \bar{\Phi}(\boldsymbol{Y}, t; \boldsymbol{\beta}_s) \tag{6.36}$$

The shape sensitivity $\overset{\circ}{\Phi} = \hat{\overset{\circ}{\Phi}}(\boldsymbol{x}_n, t; \boldsymbol{\beta}_s, \Delta\boldsymbol{\beta}_s)$ is then defined as the total Gateaux differential of $\Phi = \hat{\Phi}(\boldsymbol{x}_n, t; \boldsymbol{\beta}_s)$ in the direction $\Delta\boldsymbol{\beta}_s$ computed at $\boldsymbol{\beta}_s$

$$\begin{aligned} \hat{\overset{\circ}{\Phi}}(\boldsymbol{x}_n, t; \boldsymbol{\beta}_s, \Delta\boldsymbol{\beta}_s) \;=\; \tilde{\overset{\circ}{\Phi}}(\boldsymbol{X}, t; \boldsymbol{\beta}_s, \Delta\boldsymbol{\beta}_s) \quad &= \quad \bar{\overset{\circ}{\Phi}}(\boldsymbol{Y}, t; \boldsymbol{\beta}_s, \Delta\boldsymbol{\beta}_s) \\ &= \quad \frac{d}{d\lambda}\, \bar{\Phi}(\boldsymbol{Y}, t; \boldsymbol{\beta}_s + \lambda\Delta\boldsymbol{\beta}_s)\Big|_{\lambda=0} \end{aligned} \tag{6.37}$$

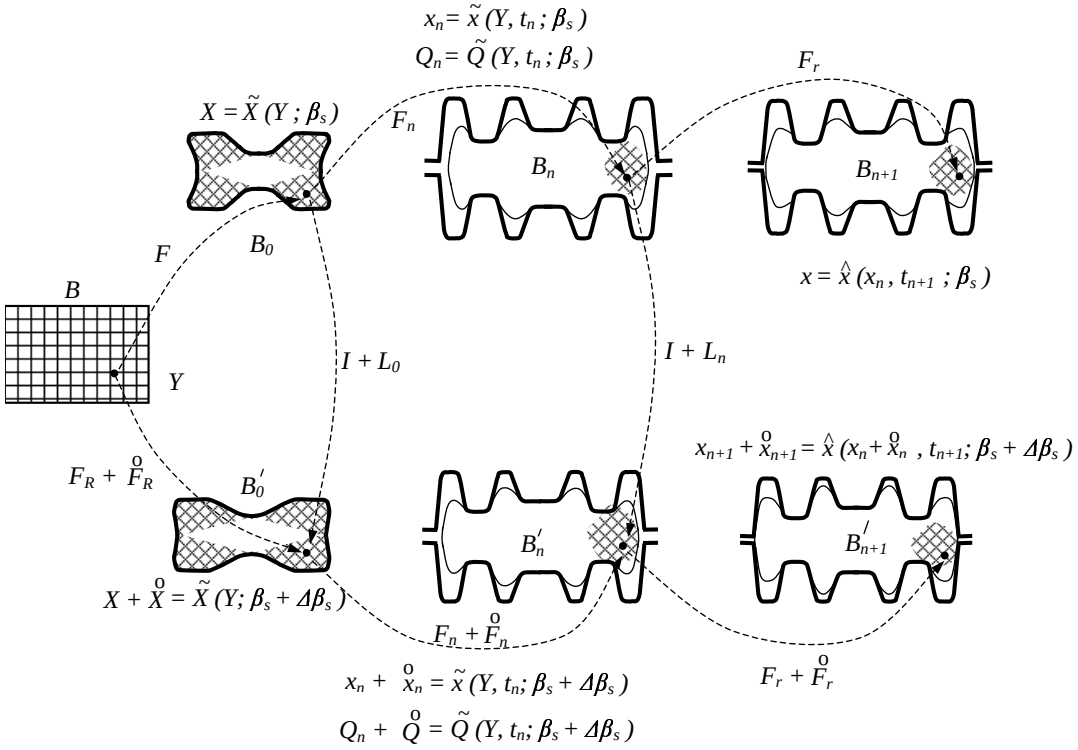

Figure 6.3: Schematic definition of the shape sensitivities in the time increment $[t_n, t_{n+1}]$ using an UL sensitivity formulation. $\mathcal{B}_n,\ n = 1, 2, \ldots$, refer to the configurations that the workpiece occupies at various times in a given deformation process for a preform $\mathcal{B}_0$ defined by the shape parameters set to the value β_s (reference problem), whereas $\mathcal{B}'_n,\ n = 1, 2, \ldots$, refer to the perturbed configurations resulting from the same deformation process but with a preform $\mathcal{B}'_0$ defined by the shape parameters $\beta_s + \Delta\beta_s$ (perturbed problem). The process parameters (die surface, ram speed, etc.) remain the same in both reference and perturbed problems.

Now the shape sensitivity $\overset{\circ}{\Phi}$ can also be approximated as the difference between two values of the field Φ, that result due to two different initial configurations defined by the shape parameters $\boldsymbol{\beta}_s + \Delta\boldsymbol{\beta}_s$ and $\boldsymbol{\beta}_s$, i.e.

$$\hat{\overset{\circ}{\Phi}}(\boldsymbol{x}_n, t; \boldsymbol{\beta}_s, \Delta\boldsymbol{\beta}_s) =$$

$$\hat{\Phi}(\tilde{\boldsymbol{x}}(\boldsymbol{X}, t_n; \boldsymbol{\beta}_s + \Delta\boldsymbol{\beta}_s), t; \boldsymbol{\beta}_s + \Delta\boldsymbol{\beta}_s) - \hat{\Phi}(\tilde{\boldsymbol{x}}(\boldsymbol{X}, t_n; \boldsymbol{\beta}_s), t; \boldsymbol{\beta}_s) + O\left(\|\Delta\boldsymbol{\beta}_s\|^2\right) =$$

$$\tilde{\Phi}(\bar{\boldsymbol{X}}(\boldsymbol{Y}; \boldsymbol{\beta}_s + \Delta\boldsymbol{\beta}_s), t; \boldsymbol{\beta}_s + \Delta\boldsymbol{\beta}_s) - \tilde{\Phi}(\bar{\boldsymbol{X}}(\boldsymbol{Y}; \boldsymbol{\beta}_s), t; \boldsymbol{\beta}_s) =$$

$$\bar{\Phi}(\boldsymbol{Y}, t; \boldsymbol{\beta}_s + \Delta\boldsymbol{\beta}_s) - \bar{\Phi}(\boldsymbol{Y}, t; \boldsymbol{\beta}_s) \tag{6.38}$$

Note that once the shape differentiation in Equation (6.38) has been performed, one can set $\boldsymbol{F}_R = \boldsymbol{I}$. It is then the perturbation $\overset{\circ}{\boldsymbol{F}}_R$ (or equivalently the velocity design gradient $\mathbf{L}_0 \equiv \overset{\circ}{\boldsymbol{F}}_R \ \boldsymbol{F}_R^{-1}$) that drives the subsequent calculation of shape sensitivities. The above definitions can be applied to both total and updated Lagrangian framework with the appropriate choice of the reference configuration. At this point, the interested reader is referred to [55] for additional details on the TL, UL sensitivity formulations and the sensitivity analysis in the context of multi-stage processing.

6.5 Deformation sensitivity problem

The definitions for sensitivity fields, discussed in the previous section, are extended towards a multi-length scale framework. The process of evaluating the sensitivities of fields on the micro-scale due to perturbations on the macro-scale is shown schematically in Figure 6.4. This requires a macro-sensitivity problem where the interest is to compute how perturbations on the macro-design variables $\boldsymbol{\beta}$ affect the continuum fields - the deformation gradient $\boldsymbol{F}$ and the velocity gradient $\boldsymbol{L}$. The dependence of the deformation gradient $\boldsymbol{F}$ on $\boldsymbol{\beta}$, in a total Lagrangian framework, can be expressed as $\boldsymbol{F} = \boldsymbol{F}(\boldsymbol{X}, t; \boldsymbol{\beta})$. The parameter sensitivity $\overset{\circ}{\boldsymbol{F}} = \overset{\circ}{\boldsymbol{F}}(\boldsymbol{X}, t; \boldsymbol{\beta}, \Delta\boldsymbol{\beta})$ is defined as the total Gateaux differential of the deformation gradient in the direction $\Delta\boldsymbol{\beta}$ computed at $\boldsymbol{\beta}$:

$$\overset{\circ}{\boldsymbol{F}}(\boldsymbol{X}, t; \boldsymbol{\beta}, \Delta\boldsymbol{\beta}) = \frac{d}{d\lambda}\boldsymbol{F}(\boldsymbol{X}, t; \boldsymbol{\beta} + \lambda\Delta\boldsymbol{\beta})\bigg|_{\lambda=0} \tag{6.39}$$

The micro-sensitivity problem, also defined in Figure 6.4, computes the resulting variation of the ODF and other microstructural properties from the perturbation

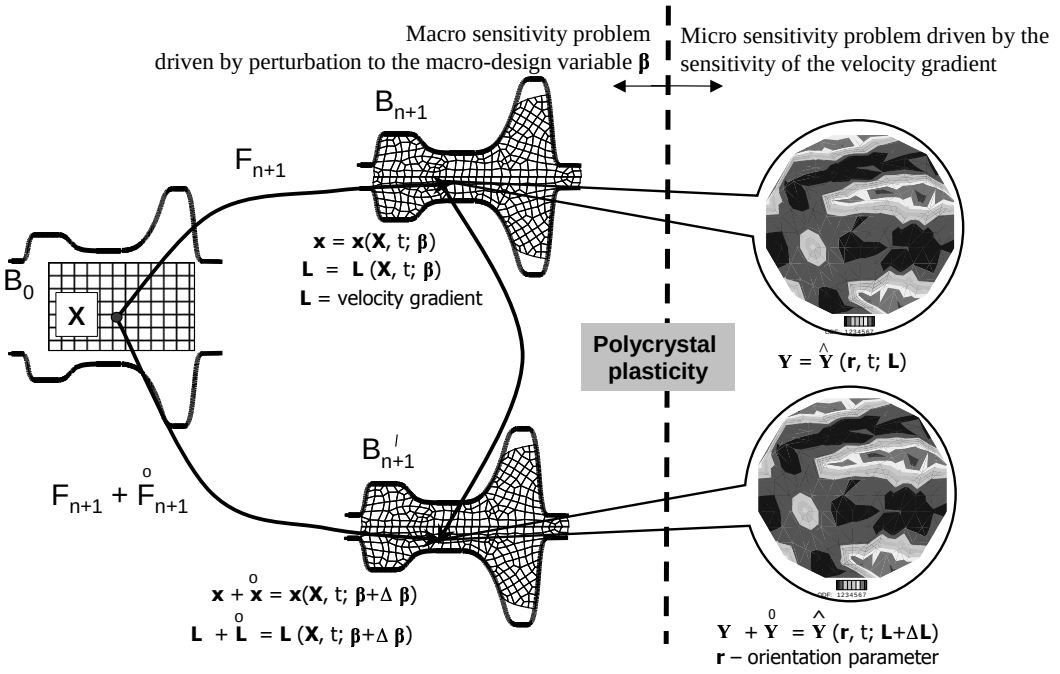

Figure 6.4: Pictorial of the two-length scale sensitivity analysis. On the left, the macro-sensitivity problem (following a Lagrangian approach) computes the sensitivities of continuum fields (e.g. of the velocity gradient) with respect to macro-design variables (here the die surface). On the right, the micro-sensitivity problem (following an Eulerian approach) computes the sensitivity of the ODF and properties related to the ODF.

$\Delta \boldsymbol{F}$ of $\boldsymbol{F}$ (or $\Delta \boldsymbol{L}$ of the velocity gradient $\boldsymbol{L}$). In extending the direct analysis in earlier sections, which was based on the Taylor hypothesis, a similar hypothesis for the sensitivity problem is developed. In particular, this is defined as follows: the sensitivity of the deformation gradient at a material point is taken to be the same as the sensitivity of the deformation gradient of the underlying crystals, in the sample reference frame.

This is used extensively in developing the constitutive sensitivity analysis for a single crystal. For the material point simulator developed here, a design vector $\boldsymbol{\beta}$ on the micro-scale is defined such that it has a one-to-one relation with $\boldsymbol{F}$. The

salient feature of such an approach is that equations governing the sensitivity fields are computed at the continuum level in all length scales. The equilibrium equation is considered and design differentiated. This continuum, differential, sensitivity equilibrium equation is then posed in a weak form so as to establish a principle of virtual work like equation for the calculation of the sensitivity of deformation fields. Consistent with this mode of analysis, the sensitivity constitutive and sensitivity thermal are derived from their corresponding continuum equations rather than their numerically integrated counterparts.

Before the sensitivity problems are discussed, the polycrystal average of sensitivity fields needs to be defined. Based on our earlier definition, the polycrystal average of the corresponding sensitivity field is determined as follows

$$\begin{aligned} \langle \overset{\circ}{\boldsymbol{\Upsilon}} \rangle &= \overset{\circ}{\int_{\mathcal{R}_t} \boldsymbol{\Upsilon}(\boldsymbol{r}, t; \boldsymbol{\beta})\ \mathcal{A}(\boldsymbol{r}, t; \boldsymbol{\beta})\ dv_t} \\ &= \int_{\mathcal{R}} \hat{\overset{\circ}{\boldsymbol{\Upsilon}}}(\boldsymbol{s}, t; \boldsymbol{\beta})\ \mathcal{A}_0(\boldsymbol{s})\ dv \end{aligned} \tag{6.40}$$

where dv_t is defined as the volume element on the current fundamental region and it is assumed that the initial texture is fixed (i.e. $\overset{\circ}{\mathcal{A}}_0 = 0$). From Equation (6.40), one can conclude that at no point in the analysis, the sensitivity of the ODF is needed to compute the polycrystal average of different properties. Examples discussed later in this Chapter, however, do report the sensitivity of the ODF as a post-processing step for validating the developed analysis.

Described below is the analysis for the development of a total Lagrangian sensitivity formulation for the kinematic problem. Let the reference configuration be $\mathcal{B}_0$. The design differentiation of the equilibrium equation (Equation 6.26) results in:

$$\overset{\circ}{\overline{\nabla_{0\bullet} \langle \boldsymbol{P} \rangle}} + \overset{\circ}{\boldsymbol{f}} = \boldsymbol{0} \tag{6.41}$$

where $\langle \boldsymbol{P} \rangle$ is the polycrystal averaged PK-I stress defined in earlier chapters. A variational form for the sensitivity equilibrium equation (for parameter sensitivity) can be posed as follows: Evaluate $\overset{\circ}{\boldsymbol{x}} = \hat{\overset{\circ}{\boldsymbol{x}}}(\boldsymbol{X}, t; \boldsymbol{\beta}, \Delta\boldsymbol{\beta})$ such that

$$\int_{\mathcal{B}_0} \langle \overset{\circ}{\boldsymbol{P}} \rangle \cdot \nabla_0 \tilde{\boldsymbol{\eta}} dV_0 = \int_{\partial\mathcal{B}_0} \overset{\circ}{\boldsymbol{\lambda}} \cdot \tilde{\boldsymbol{\eta}} \; dA_0 \tag{6.42}$$

for every $\tilde{\boldsymbol{\eta}}$, a kinematically admissible sensitivity deformation field expressed over the reference configuration $\mathcal{B}_0$. In order to solve the weak form, defined by Equation (6.42), relationships between (a) $\overset{\circ}{\boldsymbol{F}}$ and $\overset{\circ}{\boldsymbol{x}}$ (b) $\langle \overset{\circ}{\boldsymbol{P}} \rangle$ and $[\overset{\circ}{\boldsymbol{F}}, \overset{\circ}{\theta}]$ and (c) $\overset{\circ}{\boldsymbol{\lambda}}$ and $\overset{\circ}{\boldsymbol{x}}$ need to be developed. The relationship between $\overset{\circ}{\boldsymbol{F}}$ and $\overset{\circ}{\boldsymbol{x}}$ is purely kinematic and has been described in Chapter 3. The relationship between $\langle \overset{\circ}{\boldsymbol{P}} \rangle$ and $[\, \overset{\circ}{\boldsymbol{F}}, \, \overset{\circ}{\theta} \,]$ is obtained from the sensitivity constitutive problem to be discussed in Section 6.6 and takes the form:

$$\langle \overset{\circ}{\boldsymbol{P}} \rangle = \boldsymbol{\mathcal{B}} \, [\, \overset{\circ}{\boldsymbol{F}} \,] \; + \; \boldsymbol{A} \, \overset{\circ}{\theta} \; + \boldsymbol{B} \tag{6.43}$$

where $\boldsymbol{\mathcal{B}}$ is a fourth order tensor and $\boldsymbol{A}, \boldsymbol{B}$ are second order tensors. These tensors are constants defined from known direct and sensitivity fields at the previous time step, and are obtained by considering the polycrystal average of each crystal response (see Section 6.6). The relationship between $\overset{\circ}{\boldsymbol{\lambda}}$ and $\overset{\circ}{\boldsymbol{x}}$ is obtained from the sensitivity contact problem as $\overset{\circ}{\boldsymbol{\lambda}} = \boldsymbol{H}[\overset{\circ}{\boldsymbol{x}}] + \boldsymbol{d}$, where $\boldsymbol{H}$ is a second order tensor and $\boldsymbol{d}$ a vector. The non-trivial derivation of these tensors resulting by design-differentiation of a regularized contact problem can be found in [13].

6.6 Sensitivity constitutive problem

Through the crystal sensitivity constitutive sub-problem, the relationship between the polycrystal average, $\langle \overset{\circ}{\boldsymbol{T}} \rangle$ and $\left\{ \overset{\circ}{\boldsymbol{F}} \right\}$ is computed. As part of the update procedure, one computes the set $\left\{ \overset{\circ}{\boldsymbol{T}}, \; \overset{\circ}{s}, \; \overset{\circ}{\boldsymbol{F}}^e, \; \overset{\circ}{\boldsymbol{F}}^p \right\}$ for each crystal orientation at the

end of the time increment t_{n+1}, where the sensitivity of the total deformation gradient $\overset{\circ}{\boldsymbol{F}}_{n+1}$ are assumed known. The solution of the direct deformation problem is known at time t_{n+1}, the body configuration $\mathcal{B}_{n+1}$ is known at t_{n+1}. The constitutive sensitivity problem for a crystal orientation is history dependent and the solution of the sensitivity problem at time t_n is assumed known for each crystal orientation, yielding the variables $\left\{\overset{\circ}{s}_n,\ \overset{\circ}{\boldsymbol{F}^e}_n,\ \overset{\circ}{\boldsymbol{F}^p}_n\right\}$ at the beginning of each time increment. Following steps are followed to update the sensitivities at the end of each time step.

As the first step in the sensitivity constitutive problem, the trial sensitivities $\overset{\circ}{\boldsymbol{F}^e}_{trial}$ and $\overset{\circ}{\check{\boldsymbol{E}}^e}_{trial}$ are obtained as:

$$\begin{aligned}\overset{\circ}{\boldsymbol{F}^e}_{trial} &= \overset{\circ}{\boldsymbol{F}}\ \boldsymbol{F}^{p-1}_n - \boldsymbol{F}^e_{trial}\ \overset{\circ}{\boldsymbol{F}^p}_n\ \boldsymbol{F}^{p-1}_n \\ \overset{\circ}{\check{\boldsymbol{E}}^e}_{trial} &= sym(\boldsymbol{F}^{eT}_{trial}\ \overset{\circ}{\boldsymbol{F}^e}_{trial})\end{aligned} \tag{6.44}$$

Consider sensitivity of Eq. 6.20 to perturbations in $\boldsymbol{F}$ given by:

$$\begin{aligned}\overset{\circ}{\Delta\gamma}^\beta &= (A^{\alpha\beta})^{-1}(\overset{\circ}{b}^\alpha - \overset{\circ}{A}^{\alpha\beta}\ \Delta\gamma^\beta) \\ \overset{\circ}{b}^\alpha &= \mathrm{sgn}(\tau^\alpha_{trial})\boldsymbol{\mathcal{L}}^e\left[\overset{\circ}{\check{\boldsymbol{E}}^e}_{trial}\right]\cdot\boldsymbol{S}^\alpha_0 - \overset{\circ}{s}^\alpha_n \\ \delta A^{\alpha\beta} &= \overset{\circ}{h}^{\alpha\beta} + \mathrm{sgn}(\tau^\alpha_{trial})\mathrm{sgn}(\tau^\beta_{trial})\boldsymbol{S}^\alpha_0\cdot\boldsymbol{\mathcal{L}}^e\left[\boldsymbol{S}^{\beta T}_0\ \overset{\circ}{\check{\boldsymbol{E}}^e}_{trial} + \overset{\circ}{\check{\boldsymbol{E}}^e}_{trial}\ \boldsymbol{S}^\beta_0\right]\end{aligned} \tag{6.45}$$

Remark: Here, $\alpha, \beta \in \mathcal{PA}$ are the active systems identified in the direct problem. This assumes that slip systems activated under a perturbed deformation gradient $(\boldsymbol{F} + \overset{\circ}{\boldsymbol{F}})$ are the same as when a deformation gradient of $\boldsymbol{F}$ is acting on the crystal. This is a valid assumption since the applied perturbations to the design variables are small ($\sim 1E-7$) and hence, no new slip systems are activated.

The above set of equations along with Eq. 6.44 yield an linear relation $\overset{\circ}{\Delta\gamma}^\beta = \boldsymbol{n}^\beta\cdot\overset{\circ}{\boldsymbol{F}} + n^\beta_o$. This relation is then used to compute the linear relationship of $\overset{\circ}{\boldsymbol{F}^p}$

and $\overset{\circ}{\boldsymbol{F}}^e$ with $\overset{\circ}{\boldsymbol{F}}$ using the equations:

$$\overset{\circ}{\boldsymbol{F}}^p = \boldsymbol{F}^p \boldsymbol{F}^{p-1}_n \overset{\circ}{\boldsymbol{F}}^p{}_n + (\sum_\beta \mathrm{sgn}(\tau^\beta_{trial}) \overset{\circ}{\Delta\gamma}{}^\beta \boldsymbol{S}^\beta_0) \boldsymbol{F}^p_n$$

$$\overset{\circ}{\boldsymbol{F}}^e = \overset{\circ}{\boldsymbol{F}} \boldsymbol{F}^{p-1} - \boldsymbol{F}^e \overset{\circ}{\boldsymbol{F}}^p \boldsymbol{F}^{p-1} \tag{6.46}$$

Following this step, a linear equation relating $\overset{\circ}{\boldsymbol{F}}$ and $\overset{\circ}{\bar{\boldsymbol{T}}}$ is obtained using the relation $\overset{\circ}{\bar{\boldsymbol{T}}} = \boldsymbol{\mathcal{L}}^e \left[sym(\boldsymbol{F}^{eT} \overset{\circ}{\boldsymbol{F}}^e) \right]$. The dependency between $\overset{\circ}{\boldsymbol{T}}$ and $\overset{\circ}{\boldsymbol{F}}$ is then obtained by design differentiating Equation (6.15). Sensitivities of slip system resistance (s^α) are updated and stored for use in the next time step.

The above analysis dealt with finding linear relations between various sensitivity terms for a given crystal orientation. This analysis has to be performed at all orientations to compute the polycrystal average. Consider, for example, the sensitivity of PK-I stress:

$$\begin{aligned}
\langle \overset{\circ}{\boldsymbol{P}} \rangle &= \langle \left[\mathrm{tr} \left(\overset{\circ}{\boldsymbol{F}} \boldsymbol{F}^{-1} \right) \det\boldsymbol{F} \boldsymbol{T} \boldsymbol{F}^{-T} + \det\boldsymbol{F} \overset{\circ}{\boldsymbol{T}} \boldsymbol{F}^{-T} - \det\boldsymbol{F} \boldsymbol{T} \boldsymbol{F}^{-T} \overset{\circ}{\boldsymbol{F}}{}^T \boldsymbol{F}^{-T} \right] \rangle \\
&= \mathrm{tr} \left(\overset{\circ}{\boldsymbol{F}} \boldsymbol{F}^{-1} \right) \det\boldsymbol{F} \langle \boldsymbol{T} \rangle \boldsymbol{F}^{-T} + \det\boldsymbol{F} \langle \overset{\circ}{\boldsymbol{T}} \rangle \boldsymbol{F}^{-T} \\
&- \det\boldsymbol{F} \langle \boldsymbol{T} \rangle \boldsymbol{F}^{-T} \overset{\circ}{\boldsymbol{F}}{}^T \boldsymbol{F}^{-T}
\end{aligned} \tag{6.47}$$

where $\langle \overset{\circ}{\boldsymbol{T}} \rangle = \int_{\mathcal{R}_0} \overset{\circ}{\boldsymbol{T}} \mathcal{A}_0 dv$ and $\overset{\circ}{\boldsymbol{T}}$ is described by the relations developed earlier. From these equations, one can generate the constants in Equation (6.43) and use this in the solution of the sensitivity kinematic problem.

6.6.1 Sensitivity of the spin vector

Once $\overset{\circ}{\boldsymbol{F}}{}^e{}_{n+1}$ has been evaluated from the previous sub-sections, $\overset{\circ}{\boldsymbol{R}}{}^e{}_{n+1}$ can be obtained as [87] (subscript $n+1$ is dropped in this Equation):

$$\overset{\circ}{\boldsymbol{R}}{}^e = \overset{\circ}{\boldsymbol{F}}{}^e \boldsymbol{F}^{e-1} \boldsymbol{R}^e - \boldsymbol{R}^e \mathrm{sym} \left\{ \boldsymbol{U}^{e-1} \mathrm{sym} \left(\boldsymbol{F}^{eT} \overset{\circ}{\boldsymbol{F}}{}^e \right) \right\} \boldsymbol{F}^{e-1} \boldsymbol{R}^e \tag{6.48}$$

Sensitivities of spin vector and the spin tensor are obtained as:

$$\overset{\circ}{\boldsymbol{\omega}} = \text{vect}\left(\overset{\circ}{\boldsymbol{\Omega}}\right) \tag{6.49}$$

$$\overset{\circ}{\boldsymbol{\Omega}} = \dot{\overset{\circ}{\boldsymbol{R}}}^{e}\boldsymbol{R}^{eT} - \boldsymbol{\Omega}\overset{\circ}{\boldsymbol{R}}^{e}\boldsymbol{R}^{eT} \tag{6.50}$$

where $\overline{\overset{\circ}{\boldsymbol{R}^{eT}}} = -\boldsymbol{R}^{eT}\,\overset{\circ}{\boldsymbol{R}}^{e}\,\boldsymbol{R}^{eT}$. Euler-backward integration of Equation 6.50 results in:

$$\overset{\circ}{\boldsymbol{\Omega}} = \frac{1}{\Delta t}\left[\overset{\circ}{\boldsymbol{R}}^{e}\,\boldsymbol{R}^{eT} - \boldsymbol{R}^{e}\boldsymbol{R}^{eT}_{n}\,\overset{\circ}{\boldsymbol{R}}^{e}_{n}\,\boldsymbol{R}^{eT}\right] \tag{6.51}$$

where the subscript $(n+1)$ has been dropped for convenience and $\overset{\circ}{\boldsymbol{R}}^{e}$ was evaluated in Equation (6.48). Further, $\overset{\circ}{\boldsymbol{\omega}}$ can be evaluated from Equation (6.49).

6.7 Sensitivity analysis of the orientation distribution function

Consider the re-orientation velocity defined in Equation (6.22). The design-differentiation of this equation results in the sensitivity of the re-orientation velocity:

$$\overset{\circ}{\boldsymbol{v}} = \frac{\partial\,\overset{\circ}{\boldsymbol{r}}}{\partial t} = \frac{1}{2}\left[\overset{\circ}{\boldsymbol{\omega}} + (\overset{\circ}{\boldsymbol{\omega}}\cdot\boldsymbol{r})\boldsymbol{r} + \overset{\circ}{\boldsymbol{\omega}}\times\boldsymbol{r}\right] + \frac{1}{2}\left[\boldsymbol{\omega}\otimes\boldsymbol{r} + (\boldsymbol{\omega}\cdot\boldsymbol{r})\boldsymbol{I} + \boldsymbol{\Omega}\right]\overset{\circ}{\boldsymbol{r}} \tag{6.52}$$

which can further be written as

$$\frac{\partial\,\overset{\circ}{\boldsymbol{r}}}{\partial t} - \boldsymbol{M}_2\,\overset{\circ}{\boldsymbol{r}} = \frac{1}{2}\left(\overset{\circ}{\boldsymbol{\omega}} + (\overset{\circ}{\boldsymbol{\omega}}\cdot\boldsymbol{r})\boldsymbol{r} + \overset{\circ}{\boldsymbol{\omega}}\times\boldsymbol{r}\right) \tag{6.53}$$

where $\boldsymbol{M}_2 = \frac{1}{2}\left\{\boldsymbol{\omega}\otimes\boldsymbol{r} + (\boldsymbol{\omega}\cdot\boldsymbol{r})\boldsymbol{I} + \boldsymbol{\Omega}\right\}$ and $\overset{\circ}{\boldsymbol{\omega}}$ was defined in the previous section. Assuming small time steps and applying an Euler-backward time integration scheme, leads to the following linear system:

$$\overset{\circ}{\boldsymbol{r}}_{n+1} = \left\{\boldsymbol{I} + \frac{\Delta t}{2}\left\{\boldsymbol{\omega}_{n+1}\otimes\boldsymbol{r}_{n+1} + (\boldsymbol{\omega}_{n+1}\cdot\boldsymbol{r}_{n+1})\boldsymbol{I} + \boldsymbol{\Omega}_{n+1}\right\}\right\}\overset{\circ}{\boldsymbol{r}}_{n} +$$

$$\frac{\Delta t}{2}\left[\overset{\circ}{\boldsymbol{\omega}}_{n+1} + (\overset{\circ}{\boldsymbol{\omega}}_{n+1}\cdot\boldsymbol{r}_{n+1})\boldsymbol{r}_{n+1} + \overset{\circ}{\boldsymbol{\omega}}_{n+1}\times\boldsymbol{r}_{n+1}\right] \tag{6.54}$$

which can be solved for $\overset{\circ}{\boldsymbol{r}}_{n+1}$ to compute sensitivity of the current fundamental region.

Now consider the Lagrangian version of the ODF conservation equation (Equation (6.6)). Design differentiation of this equation, assuming that the initial texture is independent of the design parameters, leads to the following:

$$\overset{\circ}{\hat{\mathcal{A}}}\,(\boldsymbol{s},t;\boldsymbol{\beta},\Delta\boldsymbol{\beta})\;J(\boldsymbol{s},t;\boldsymbol{\beta}) \;=\; -\hat{\mathcal{A}}(\boldsymbol{s},t;\boldsymbol{\beta})\;\;\overset{\circ}{J}\,(\boldsymbol{s},t;\boldsymbol{\beta},\Delta\boldsymbol{\beta}) \tag{6.55}$$

where $\overset{\circ}{J}\;(\boldsymbol{s},t;\boldsymbol{\beta},\Delta\boldsymbol{\beta}) \;=\; \overset{\circ}{\det(\nabla\hat{\boldsymbol{r}}(\boldsymbol{s},t;\boldsymbol{\beta},\Delta\boldsymbol{\beta}))} = \;\; J(\boldsymbol{s},t;\boldsymbol{\beta})\left[\nabla_{\bullet}\;\overset{\circ}{\boldsymbol{r}}\;(\boldsymbol{s},t;\boldsymbol{\beta},\Delta\boldsymbol{\beta})\right]$ and $\overset{\circ}{\boldsymbol{r}}$ has been evaluated in Equation (6.54).

6.8 Numerical examples

The slip system hardening model used in the examples is given as:

$$h^{\alpha\beta} = [q + (1-q)\delta^{\alpha\beta}]h^{\beta}(\text{no sum on }\beta) \tag{6.56}$$

where h^{β} is a single slip hardening rate, and q is the latent-hardening ratio. The parameter q is taken to be 1.0 for coplanar slip systems and 1.4 for non-coplanar slip systems. For the single slip hardening rate, the following specific form is adopted:

$$h^{\beta} = h_o(1 - \frac{s^{\beta}}{s_s})^a \tag{6.57}$$

where h_o,a, and s_s are slip hardening parameters taken to be identical for all slip systems, with values $h_o = 180$ MPa, $s_s = 148$ MPa and $a = 2.25$ for f.c.c copper single crystals. The initial value of slip system resistance is taken as $s_o = 16MPa$ [57]. Values of elastic parameters for copper crystal are taken as

$C_{11} = 170$ GPa, $C_{12} = 124$ GPa, $C_{44} = 75$ GPa. Slip is assumed to occur in the 12 $\{111\} < 110 >$ slip systems in the FCC crystal. As a validation of the micro-scale texture evolution model, results are compared with the numerical example of [57]. The experiment corresponds to an x-axis compression with a strain rate of 0.001 $/s$ of FCC copper polycrystal. The initial texturing of the material is assumed to be random, and this corresponds to a constant Lagrangian ODF of 2.435. The reference fundamental region is discretized into 448 tetrahedral elements with cubic symmetry enforced in the solution procedure. Comparison of results of [57] with the present ODF-Taylor model is shown in Figure. 6.5.

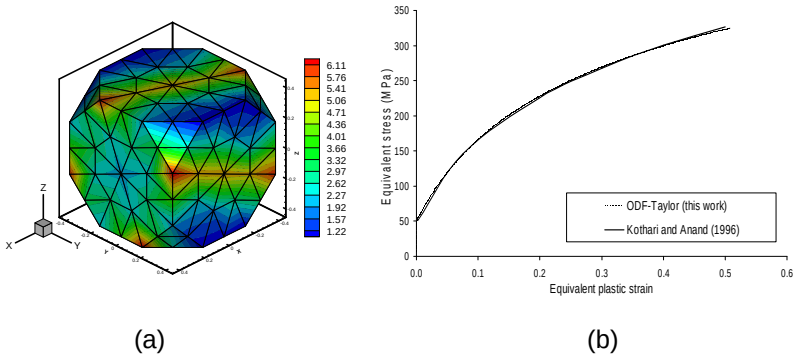

Figure 6.5: (a) Texture obtained using the Taylor model after 135 sec of simple compression of a copper polycrystal at the rate of $1e-3s^{-1}$. (b) Comparison of equivalent stress-strain response with results from [57].

To validate the continuum sensitivity algorithm we consider the problem of simple plane strain compression of a block and compare the sensitivities obtained using finite difference approximation (FDM) which is the difference in solutions of two non-linear direct problems with compression rates α and $\alpha + \delta\alpha$ and the continuum sensitivity method(CSM) (obtained through solution of one non-linear direct problem and a linear sensitivity problem). The initial block size is taken as 1.0 mm by 1.0 mm. The straining rate is fixed at $10^{-2}s^{-1}$, and simulation is

for a total time of 3.2 sec. Parameter sensitivities are computed with respect to a perturbation of $1e-7$ mm/s to the compression rate. Fig. 6.6 shows comparison of texture sensitivity of the two techniques in the two-scale problem where it is seen that CSM produces exactly the same sensitivity results with much less computational effort.

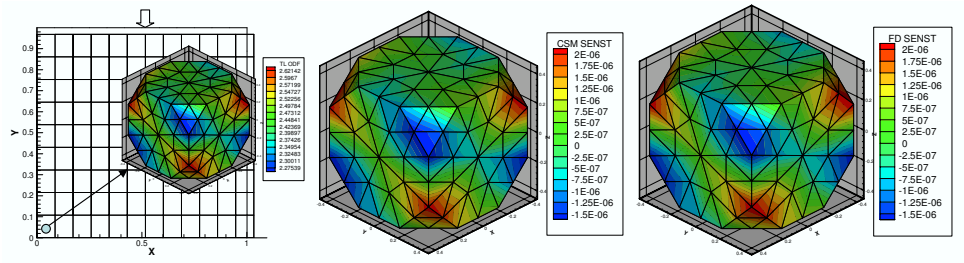

(a) (b) (c)

Figure 6.6: (a) Multi-scale plane strain compression of a block, final texture at the bottom left corner element is shown. (b) Sensitivity of this texture calculated using the CSM technique is compared with (c) sensitivities obtained using the finite difference technique.

The parameter sensitivities in the design problem, as discussed later, are computed with respect to a perturbation of $1e-7$ units to the design parameters. First two examples involve control of properties in axi-symmetric extrusion and closed die forging processes, simulated without remeshing. The last two examples relates to control of strength and magnetic hysteresis losses in complex forging processes in the presence of remeshing and data transfer. In all examples, an assumed strain analysis scheme is used to treat the effect of near-incompressibility based on the work in [13]. To aid in speeding up the solution process for complex forging processes, the design simulator was parallelized using MPI. The simulator was developed using object oriented programming and dynamically linked to the parallel toolbox PetSc for parallel assembly and solution of linear systems. In particular, for solution of linear systems a GMRES solver along with block Jacobi and ILU preconditioning from the PetSc toolbox was employed.

6.8.1 Example 1. Design of Youngs modulus distribution during extrusion

In this example, we study the feasibility of controlling Young's Modulus distribution in the finished product through control of extrusion die shape. An axisymmetric extrusion process is considered with a fixed reduction in cross-section over a fixed length. During extrusion process, texturing and material state strongly varies over the final cross-section due to the loading conditions. Through control of loading conditions, in particular, the die shape, it is possible to minimize variations in properties in the finished product. The objective is to design the die shape such that the Young's modulus distribution at the exit is as uniform as possible. The objective function for the design problems is defined as follows:

$$\min_{\boldsymbol{\alpha}} \boldsymbol{F}(\boldsymbol{\alpha}) = \sum_{i=1}^{N} \left((E_i(\boldsymbol{\alpha}) - \bar{E}(\boldsymbol{\alpha}))^2 \right) \tag{6.58}$$

where $E_i (i = 1..N)$ is the Youngs modulus at the N nodal points in the exit cross section and $\bar{E}$ is the mean property over those points defined as $\bar{E} = \frac{1}{N} \sum_{i=1}^{N} E_i$. The Young's Modulus for loading along a particular direction at each material point is found using the polycrystal stiffness, $\langle \boldsymbol{C} \rangle$, computed through a weighted average (over $\mathcal{A}$) of the stiffness of individual crystals expressed in the sample reference frame. Young's modulus for the polycrystal is then computed through the averaged stiffness matrix as:

$$\boldsymbol{E} \;=\; \frac{1.0}{(\langle \boldsymbol{C} \rangle)^{-1}_{(11)}} \tag{6.59}$$

Initial texturing of preform is assumed to be random, and this corresponds to a constant Lagrangian ODF of 2.435. The reference fundamental region with cubic symmetry is discretized into 61 tetrahedral elements. We design an extrusion process with a die of area reduction of 13.5% over a length of 0.5 mm. Initial radius of

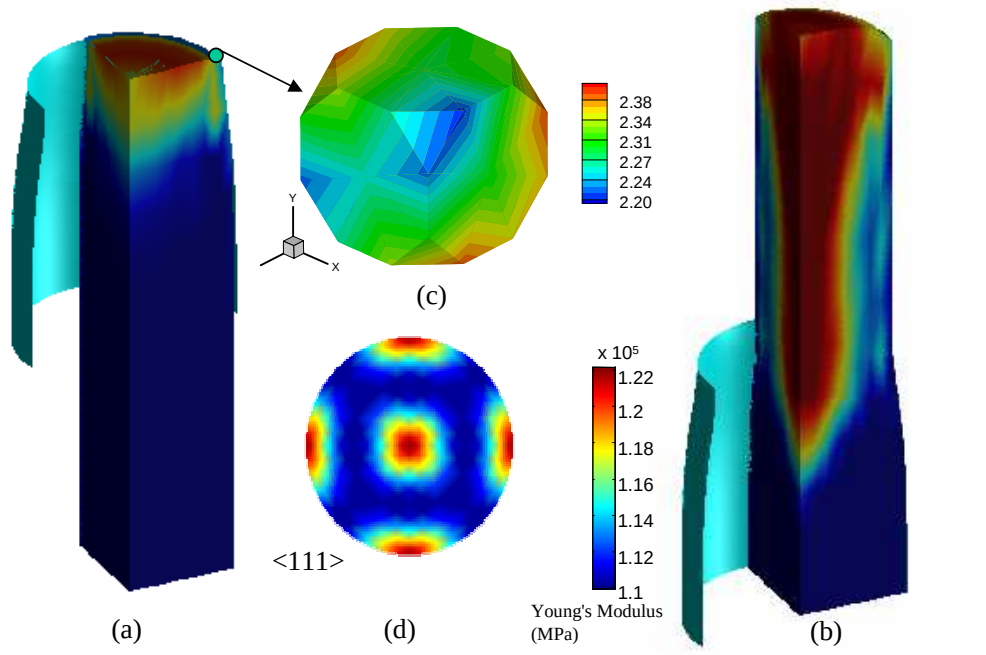

Figure 6.7: (a) The distribution of Youngs Modulus when the exit cross section just leaves the extrusion die (b) Youngs Modulus distribution in the final time step (c) ODF at a repreentative material point close to the die surface. (d) The $< 111 >$ pole figure of the ODF.

the workpiece is 0.5 mm and the initial height is 1.0 mm. It was extruded with a nominal displacement rate of 0.1 s^{-1}. A total of 400 time steps up to $t = 10s$ were performed to reach steady-state conditions at the exit. Die-workpiece interface friction coefficient is taken as 0.01. The die surface is represented by a degree 7 Bezier curve as follows:

$$r(\beta) = \sum_{i=1}^{7} C_i \phi_i(\beta), z = \frac{\beta}{2} \text{ in mm}, 0 \leq \beta \leq 1, \tag{6.60}$$

where $C_i, i = [1, ..., 7]$, are the algebraic control parameters. The Bernstein functions $\phi_i(\beta)$ are given as

$$\phi_1 = (1.0 - \beta)^6,$$

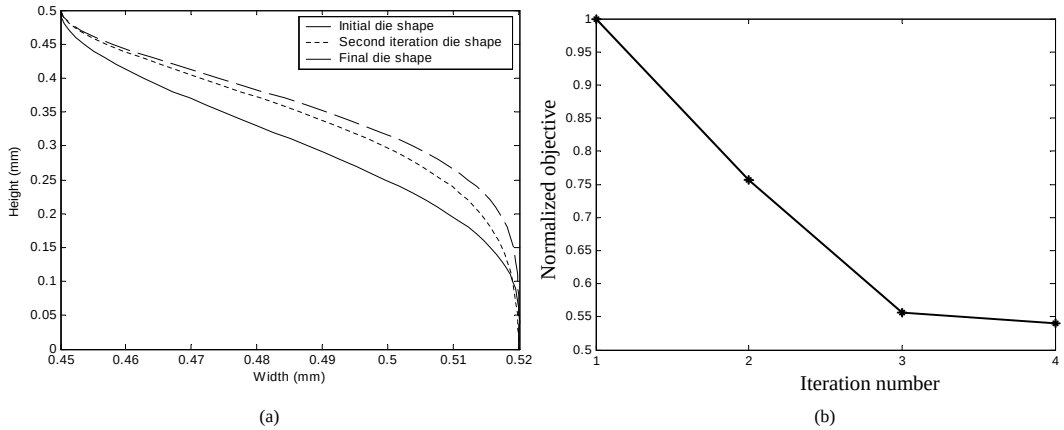

Figure 6.8: (a) The extrusion die profile at the initial, intermediate and final iteration (b) The decrease in cost function at successive iterations

$$\begin{aligned}
\phi_2 &= 6.0(1.0-\beta)^5\beta \\
\phi_3 &= 15.0(1.0-\beta)^4\beta^2, \\
\phi_4 &= 20.0(1.0-\beta)^3\beta^3, \\
\phi_5 &= 15.0(1.0-\beta)^2\beta^4, \\
\phi_6 &= 6.0(1.0-\beta)\beta^5, \\
\phi_7 &= \beta^6,
\end{aligned} \tag{6.61}$$

We apply the constraints (in order to obtain the same reduction for different die design parameters) that the radius and slope (with respect to the z-axis) at the inlet and exit are fixed with $C_2 = C_1 = 0.52$ mm, $C_6 = C_7 = 0.45$ mm. With this selection of parameters, there are three design parameters $\boldsymbol{\alpha} = (C_3, C_4, C_5)$ for the control problem. An initial guess of $C_3 = 0.52, C_4 = 0.52, C_5 = 0.52$ mm was employed. The energy and displacement error norms for the finite element solution are taken to be 10^{-4}.

Fig. 6.7 shows the intermediate configuration (at 0.5 mm stroke) and the final

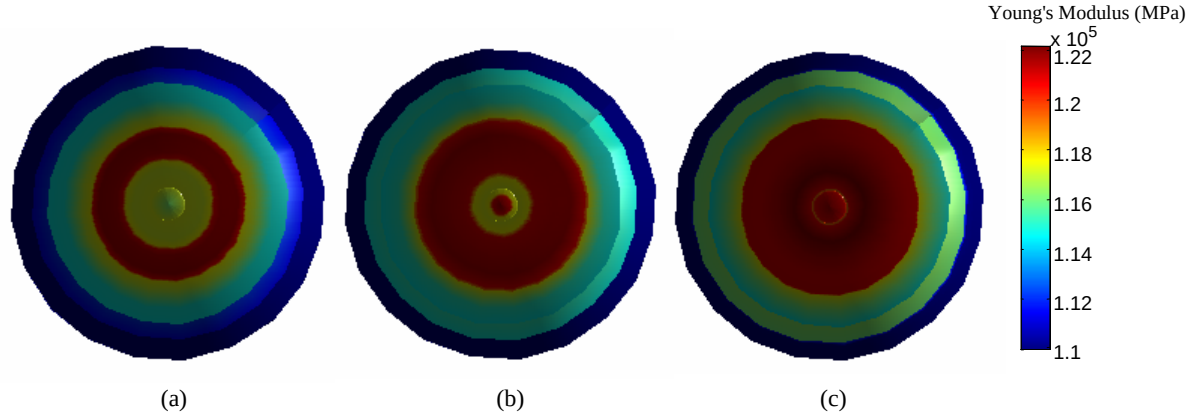

Figure 6.9: Young's modulus distribution on the exit cross section at the end of extrusion in the (a) first iteration (b) second iteration (c) final iteration

configuration (at 1 mm stroke) of the extrusion process along with a representative ODF (Fig. 6.7(c)) obtained at a point on the circumference of the exit cross section at 0.5 mm stroke. The ODF, as expected for an extrusion process, can be seen to arise from a predominantly x-y axis shear deformation, as evidenced by the strong x-axis $< 111 >$ fiber in the $< 111 >$ pole figure (Fig. 6.7(e)). Observe that due to the natural symmetry of Rodrigues space, axes of the space relate directly to sample axes. The x-axis $< 111 >$ fibers lie near boundaries of the fundamental region and are seen across the z- face of the ODF. Note that in Rodrigues-Frank space, ideal orientations lie on boundaries of the fundamental region which allows the structure of the textures to be reflected adequately by the boundary ODF.

The die shape identified at various iterations of the design problem and variation of the objective function over all iterations are shown in Fig.6.8. The optimal die shape corresponds to Bezier coefficients $C_3 = 0.5229, C_4 = 0.5099, C_5 = 0.4765$. The Youngs' modulus distribution on the curved surface at the end of forging at the first, second and final iteration are shown in Fig.6.9. In the first iteration, the Youngs' modulus distribution is highly non-uniform with variation from 116

GPa at the center to a maximum of 123 GPa halfway from the center. In the final iteration, the deviation reduces to just 1 GPa from the center to about two-thirds of the exit cross section. The optimal solution for the design problem is attained in just 4 iterations showcasing the efficiency of the design algorithm.

6.8.2 Example 2. Design of yield strength variation during closed die forging

In this problem, the forging of a circular disc is considered. The primary objective is to design the preform for a final forged product (with fixed stroke) such that the die cavity is fully filled. The secondary objective in this problem is to minimize the variation of strength on the curved surface of the final product. One way to ensure that the die cavity is filled is to consider a preform of a much larger volume than that needed. In this case, the die cavity is filled up but there will be considerable material wastage due to flash. Further, our secondary objective of minimizing yield strength variation might not be satisfied. The objective function for the design problem is defined so as to fulfill both objectives:

$$\begin{aligned} \min_{\boldsymbol{\alpha}} \boldsymbol{F}(\boldsymbol{\alpha}) &= \frac{1}{N}\sum_{i=1}^{N}\left((Y_i(\boldsymbol{\alpha}) - \bar{Y}(\boldsymbol{\alpha}))^2\right) \\ + \quad &\sum_{i=1}^{N^*}\left((r_i(\boldsymbol{\alpha}) - r_i^{desired})^2 + (z_i(\boldsymbol{\alpha}) - z_i^{desired})^2\right) \end{aligned} \tag{6.62}$$

where $Y_i (i = 1..N)$ are the yield strength values on the curved surface in the final product and $\bar{Y}$ is the mean property over those points defined as $\bar{Y} = \frac{1}{N}\sum_{i=1}^{N} Y_i$. $r_i^{desired}$ and $z_i^{desired}$ are the closest point projections of the points $r_i(\boldsymbol{\alpha})$ and $z_i(\boldsymbol{\alpha})$ on the die and N^* denotes the number of points on the contact (top and curved) surface. Crystal plasticity model described previously is used to calculate yield

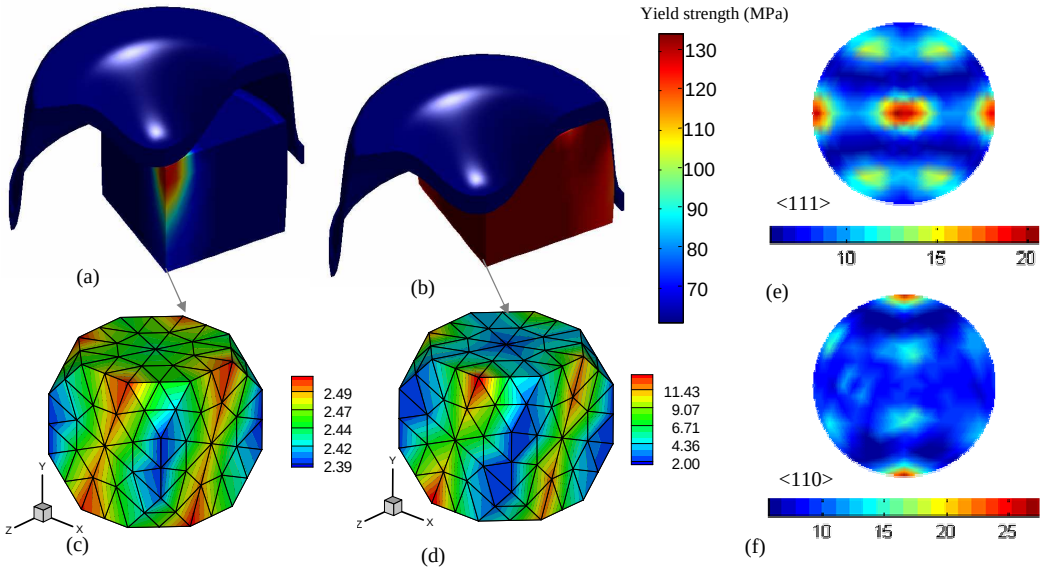

Figure 6.10: (a) Yield strength distribution at 0.02 mm stroke (b) Yield strength distribution at 0.3 mm stroke (c,d) ODF at a point close to the bottom corner of the preform at 0.02 and 0.3 mm stroke. (e,f) The $< 111 >$ and $< 110 >$ pole figures of the ODF in (d).

strength at all Gauss points using the ODF and slip system resistances at each time step. In this method, polycrystal at each integration point in the macro-scale mesh is separately subject to uniaxial (y- axis) tension conditions up to a strain of 0.2% to obtain the corresponding 0.2% offset yield strength at each integration point.

Initial surface of the preform ($R_\alpha(\beta)$) is represented with a degree 6 Bezier curve. Using the restriction $R'_\alpha(0) = 0$, the representation of R_α can be defined with 6 independent design variables α_i, $i = [1...6]$ as follows:

$$R_\alpha(\beta) = \sum_{i=1}^{6} \alpha_i \phi_i(\beta), 0 \leq \beta \leq 1, \tag{6.63}$$

Where $\beta = \frac{z}{H}$ represents the z-coordinate normalized with the height of the

preform. Basis functions are given as:

$$\begin{aligned}
\phi_1 &= (1.0-\beta)^6 + 6\beta(1-\beta)^5, \\
\phi_2 &= 15.0(1.0-\beta)^4\beta^2, \\
\phi_3 &= 20.0(1.0-\beta)^3\beta^3, \\
\phi_4 &= 15.0(1.0-\beta)^2\beta^4, \\
\phi_5 &= 6.0(1.0-\beta)\beta^5, \\
\phi_6 &= \beta^6, \qquad (6.64)
\end{aligned}$$

The optimization iterations start with a preform of lesser volume than the die cavity and the design iterations try to attain the optimum shape of the final preform that satisfies the objectives. The specified forging velocity is taken as 0.01 mm/s and the shape parameters in the reference preform are $\alpha_i = 1.0$ for all i. This corresponds to a cylindrical preform of radius 1.0 mm. The objective is to design the free surface (represented by the degree 6 Bezier curve) of the preform of fixed height $H = 0.60$ mm that when forged using the closed forming die results in a fully filled die cavity and uniform distribution of yield strength on the external surface after a specified stroke of 0.3 mm. The die is described as follows,

$$\begin{aligned}
& r(\eta) = 1.3(1-\eta), \\
& z(\eta) = 548.357\eta^3 + 1.35, \eta \in [0, 0.07692], \\
& z(\eta) = 378.373(\eta - 0.16952)^3 + 1.9, \eta \in [0.07692, 0.16952], \\
& z(\eta) = 1.9, \eta \in [0.16952, 0.36663], \\
& z(\eta) = 0.15(15.0463 - 79.3599\eta + 295.8557\eta^2 - 511.8711\eta^3 \\
+ \quad & 403.3830\eta^4 - 118.0541\eta^5) + 0.85, \eta > 0.36663.
\end{aligned}$$

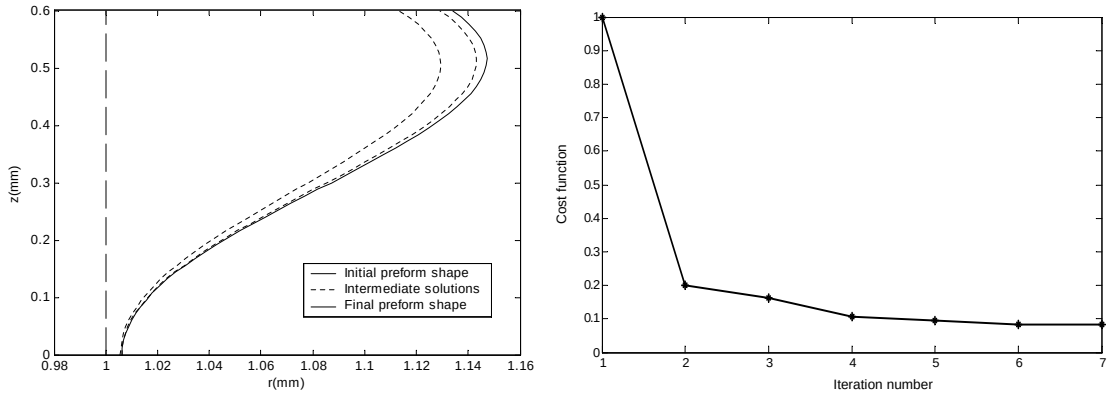

Figure 6.11: (a) Profile of the curved surface of the preform at the initial, intermediate and final iterations of the design problem (b) Decrease in cost function at successive iterations

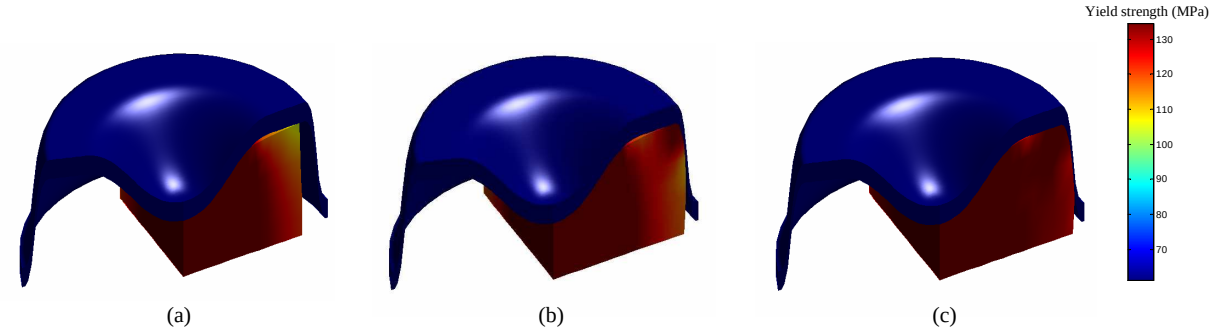

Figure 6.12: Final configuration at the end of forging in the (a) first iteration (b) second iteration (c) final iteration

(6.65)

The workpiece is assumed to be isothermal. The initial temperature of the billet is assumed to be uniform and equal to $300K$. The forging die is modelled as a rigid surface and to simulate sticking friction between the die and workpiece, a coefficient of friction of 0.1 is applied. The energy and displacement error norms for the finite element solution are taken to be 10^{-4}.

Fig. 6.10 shows an intermediate step (at 0.02 mm stroke) and the final forged

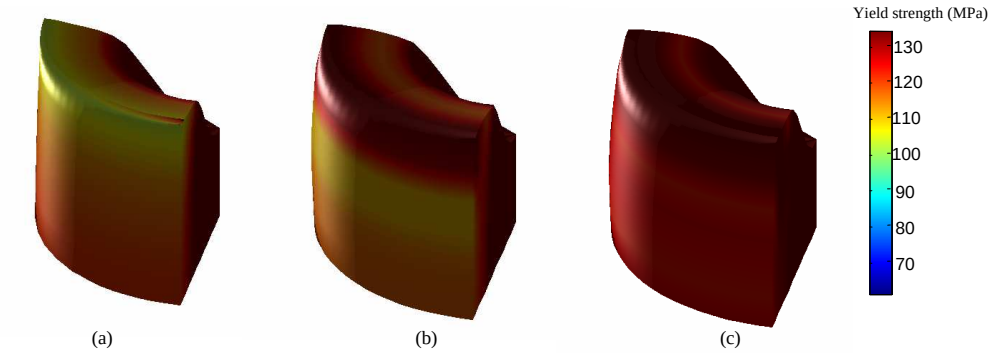

Figure 6.13: Yield strength distribution on the curved surface at the end of forging at the (a) first iteration (b) second iteration (c) final iteration

product (at 0.3 mm stroke) at the optimal preform shape along with a representative ODF calculated at the material point marked in the figure. The development of y-axis compression texture is clearly captured in the simulation. FCC metals are typically associated with texturing to $< 110 >$ fibers under compression. At lower strain (0.02 mm stroke, Fig. 6.10c), intensities can be seen to develop uniformly along the compression (y-) axis $< 110 >$ fibers that are seen across the z- and x-faces of the ODF. At higher strains (0.3 mm stroke, Fig. 6.10d), the ODF within the attracting regions about the $< 110 >$ fibers intensifies and sharpens. Also, note the boundary symmetry of the space that implies that structures associated with fibers on opposing faces comprise a single feature. While the $< 110 >$ fibers correspond to regions attracting crystal flow, the $< 100 >$ and $< 111 >$ fibers define regions that repel crystal flow. This is seen from the pole figures in Fig. 6.10(e), where compression axis $< 110 >$ fiber develops high intensities.

The preform shape identified at various iterations of the design problem and the objective function over 7 iterations are shown in Fig.6.11. The optimal solution for the design problem is attained in the sixth iteration. The optimal preform shape corresponds to Bezier coefficients $\boldsymbol{\alpha} = \{1.00639, 1.02940, 1.08443,$

1.15127, 1.16593, 1.13392}. The preform shape at the final time step of the optimization problem for the first, second and final iteration of the design problem is shown in Fig.6.12. The yield strength distribution on the curved surface at the end of forging at the first, second and final iteration are shown in Fig.6.13. In the first iteration (Fig.6.12(a)), the preform does not completely fill the die upon forging. Almost complete fill is obtained in as early as the second iteration (Fig.6.12(b)) showcasing the efficiency of the design algorithm. However, in this iteration, the requirement of uniform yield strength is not met and as much as 30 MPa variation is seen on the curved surface in Fig.6.13(b). In the converged solution shown in Fig.6.13(c), both requirements are met and the variation in yield strength reduces to about 3 MPa on the curved surface.

6.8.3 Example 3. Design of yield strength distribution in complex forging operations using remeshing schemes

Complex metal forming simulations often lead to severe distortions in the initial mesh. Unless the distorted mesh is replaced periodically with a new mesh, the simulation may terminate prematurely as a result of the severe mesh distortions. As a result, periodic remeshing operations need to be carried out to ensure good element quality throughout the simulation. In this work automatic hexahedral remeshing was implemented. In this approach, an unstructured hexahedral mesh is generated by first meshing the workpiece with a tetrahedral mesh following by division of each tetrahedron into four hexes. Once the remeshing is completed, all history dependent variables are transferred to the new mesh. For the integration point data, a local smoothing operation is carried out in the old mesh first to transfer the field values at the integration points to the nodes. Nodal data from

the old mesh to the new mesh are transferred by direct interpolation. The field values at the integration points of the new mesh are then obtained by interpolation of the nodal data. In the multi-scale problem, micro-scale quantities are interpolated using the macro-scale interpolation scheme. The quantities that need to be transferred at the micro-scale include the deformed ODF grid, $\boldsymbol{s}$, $\bar{\boldsymbol{T}}$, $\boldsymbol{\omega}$ and $\boldsymbol{F}^e$. $\boldsymbol{F}^p$ at each integration point on the ODF is updated after remeshing using the recomputed macro- deformation gradient $\boldsymbol{F}$. The sensitivity counterparts of these quantities are also transferred in the same manner. Details of the remeshing scheme for the direct and sensitivity problem are explained in [13].

In this problem, the forging of a spheroidal preform to form a cross-shaft is considered. The primary objective is to design the preform for a final forged product (with fixed stroke) such that the required shape is obtained. The secondary objective is same as the previous problem, i.e. to minimize the variation of strength on the curved surface of the final product. The objective function for the design problem is same as in the previous example. However, the objective function is only computed with a radius of 0.75 mm which is the required dimension of the cross-shaft as indicated in Fig. 6.10(a).

For the design problem the free surface of the sphere is discretized using Bezier curves in a similar fashion as the earlier preform design examples leading to a total of 6 design variables. The forging velocity was assumed to be 0.01 mm/s while the stroke was fixed at 0.1 mm. The shape parameters in the initial preform are $\alpha_i = 0.7$ for all i. This corresponds to a spherical preform of radius 0.7 mm. The objective is to design the free surface (represented by the degree 6 Bezier curve) of the preform of fixed height $H = 0.70$ mm that when forged using the closed forming die results in the desired dimensions (contact radius of 0.75 mm)

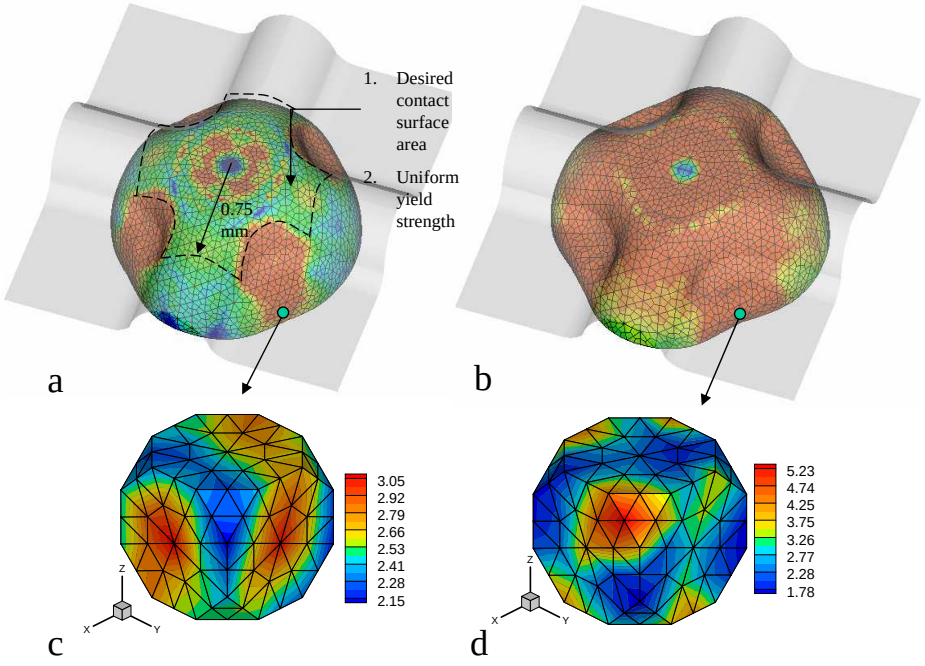

Figure 6.14: Texturing at a representative material point during an (a) intermediate and (b) final time step of the closed die forging problem. The objective function is described in (a).

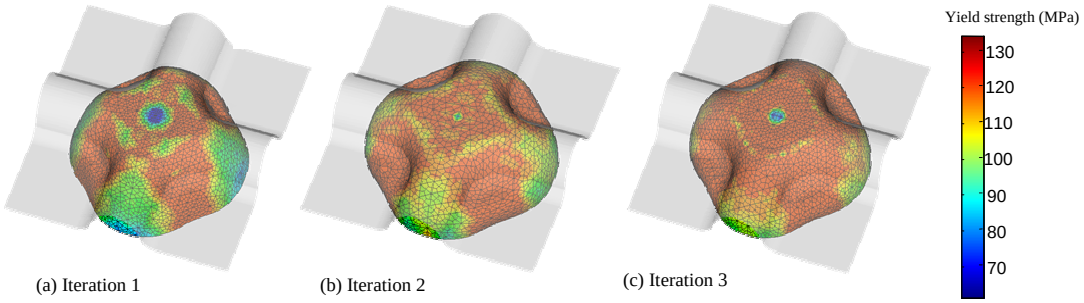

Figure 6.15: Final configuration at the end of forging for various iterations of the design problem.

and uniform distribution of yield strength on the external surface after a specified stroke of 0.1 mm. The forging die is modelled as a rigid surface and sticking friction between the die and workpiece is applied.

Fig. 6.14 shows an intermediate step (at 0.05 mm stroke) and the final forged

product (at 0.1 mm stroke) at the optimal preform shape along with a representative ODF calculated at the material point marked in the figure. The ODF at the material point is a result of the action of a variety of deformation modes over the course of the complex forging process. The ODF in Fig. 6.14(c) indicates predominantly z-axis plane strain compression mode on z-y plane as evidenced by the strong α fiber on the y- face of the ODF, while at the final time step the ODF (Fig. 6.14(d)) indicates predominantly a z- axis compression mode as seen from the strong z- axis $< 110 >$ fibers on the x- and y- face of the ODF. The preform shape and yield strength distribution at the final time step of the optimization problem for the first, second and final iteration of the design problem is shown in Fig.6.15. The figure clearly shows the decrease in variability of yield strength in successive design iterations.

6.8.4 Example 4. Design of magnetic hysteresis losses in closed die forging process

When a ferromagnetic material is taken through a cycle of magnetization and demagnetization in an alternating current field, energy is spent in aligning the magnetization vectors of the individual crystals along the direction of the external applied field. This alternating magnetization and demagnetization leads to a power loss in the material defined as hysteresis loss. Power losses also occur due to eddy currents. The total power loss can be expressed as a function of the external magnetization direction $\boldsymbol{h}$ by the expression [60]:

$$P(\boldsymbol{h}) = A_0 + A_1(l^2m^2 + m^2n^2 + l^2n^2) + A_2l^2m^2n^2 \tag{6.66}$$

where P is expressed in W/kg and l, m and n are the direction cosines of $\boldsymbol{h}$ as represented in the crystal coordinate frame.

The coefficients A_0 and A_1 are different for the total power loss and the hysteresis loss and also depend on the frequency of magnetization. The coefficient A_2 is small and is generally ignored. FCC Nickel is used as the deforming material with constitutive model parameters $h_o = 283$ MPa, $s_s = 240$ MPa, $a = 3.0$, $s_o = 16$ MPa. Elastic parameters of Nickel used are $C_{11} = 247$ GPa, $C_{12} = 147$ GPa, $C_{44} = 125$ GPa. For computation of magnetic hysteresis loss, the values $A_0 = 0$ and $A_1 = 10.0$ W/kg are used for computing the hysteresis loss of nickel at a frequency of 30 Hz [60]. The corresponding polycrystal quantities can then be obtained by averaging over the ODF as in Eq. (6.9). The external magnetization direction in the sample coordinate system is taken as $(1/\sqrt{2}, 1/\sqrt{2}, 0)$.

The particular process involved is a closed die forging of a circular disc. The primary objective is to design the preform for a final forged product such that the die cavity is fully filled with minimal flash after a stroke of 4.8 mm. The secondary objective in this problem is to minimize the hysteresis loss on the curved surface (along the perimeter) of the final product. The objective function for the design problem is thus defined as:

$$\begin{aligned} \min_{\boldsymbol{\alpha}} \boldsymbol{F}(\boldsymbol{\alpha}) &= \frac{1}{N} \sum_{i=1}^{N} \left((< P >_i (\boldsymbol{\alpha}))^2 \right) \\ + \quad & \sum_{i=1}^{N^*} \left((r_i(\boldsymbol{\alpha}) - r_i^{desired})^2 + (z_i(\boldsymbol{\alpha}) - z_i^{desired})^2 \right) \end{aligned} \tag{6.67}$$

This example presents a forging process design for producing an axi-symmetric ribbed disk. The initial billet is a right cylinder of 0.6 mm height and 1.15 mm radius. The forging velocity is taken as 0.01 mm/s. The finishing die is defined as follows:

$$
\begin{aligned}
r(\eta) &= 1.6(1-\eta), \eta \in [0.0, 1.0] \\
z(\eta) &= 0.8, \eta \in [0.0, 0.125], \\
z(\eta) &= 1111.1(\eta - 0.125)^3 + 0.80, \eta \in [0.125, 0.1875], \\
z(\eta) &= 946.75(\eta - 0.25)^3 + 1.25, \eta \in [0.1875, 0.25], \\
z(\eta) &= 1.25, \eta \in [0.25, 0.3125], \\
z(\eta) &= -3.75 + 32.0\eta - 51.20\eta^2, \eta \in [0.3125, 0.375], \\
z(\eta) &= 10.70 - 44.80\eta + 51.20\eta^2, \eta \in [0.375, 0.4375], \\
z(\eta) &= 0.90, \eta \in [0.4375, 0.5625], \\
z(\eta) &= 17.10 - 57.60\eta + 51.20\eta^2, \eta \in [0.5625, 0.625], \\
z(\eta) &= -22.90 - 70.40\eta + 51.20\eta^2, \eta \in [0.625, 0.6875], \\
z(\eta) &= 1.30, \eta \in [0.6875, 0.75], \\
z(\eta) &= -402 + 1536\eta - 1945\eta^2 + 819\eta^3, \eta \in [0.75, 0.8125], \\
z(\eta) &= 20.60 - 44.80\eta + 25.60\eta^2, \eta \in [0.8125, 0.875], \\
z(\eta) &= 1.00, \eta \in [0.875, 1.00],
\end{aligned}
\tag{6.68}
$$

This example involves four remeshing operations at times 10, 20, 30 and 40 seconds. The ODF grids are also transferred to integration points of the new mesh through smoothing and data transfer operations. The details of the remeshing procedure is same as example 3. The Bezier curve representation of the preform is given by Eqns. 6.60 and 6.63. Fig. 6.16 shows an intermediate steps (at 0.22 mm and 0.44 mm stroke) of the preform shape in the second iteration along with a representative ODF calculated at the material point marked in the figure. At 0.22 mm stroke, the ODF shown closely represents ODFs obtained from plane strain

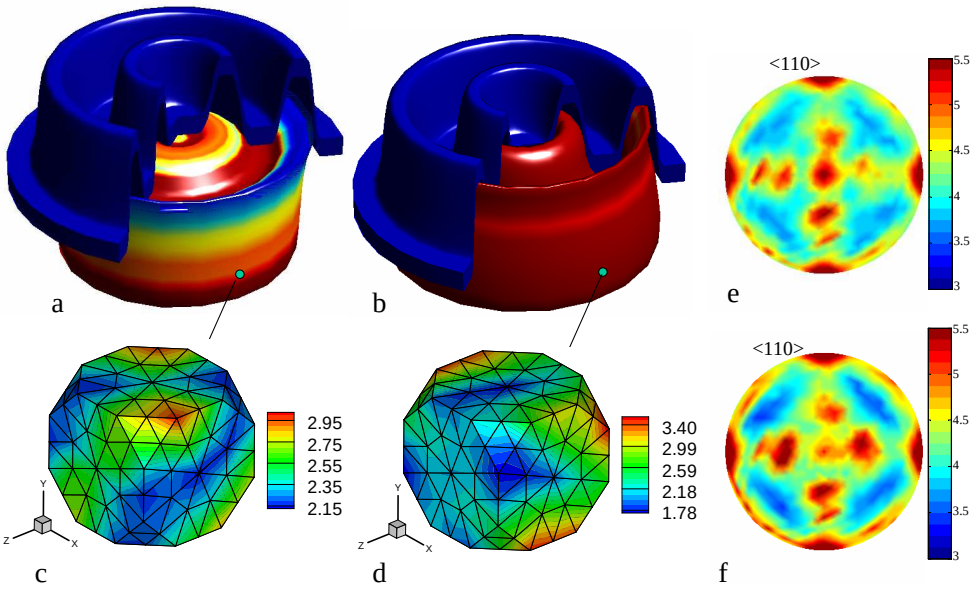

Figure 6.16: (a,b) Yield strength distribution at 0.22 mm and 0.44 mm stroke (c,d) ODF at a point close to the bottom perimeter of the preform at 0.22 and 0.44 mm stroke. (e and f) The $< 110 >$ pole figures of the ODF at 0.22 and 0.44 mm stroke respectively.

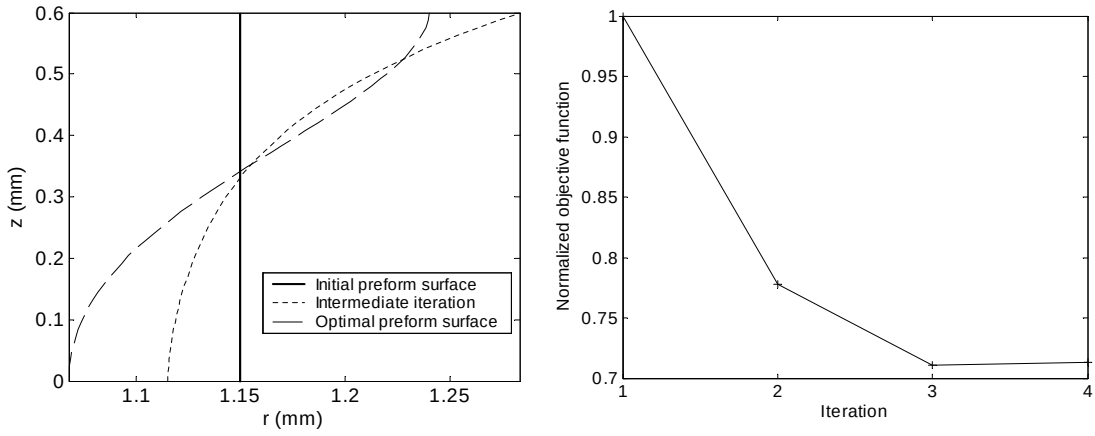

Figure 6.17: (a) Profile of the curved surface of the preform at the initial, intermediate and final iterations of the design problem (b) Decrease in cost function at successive iterations

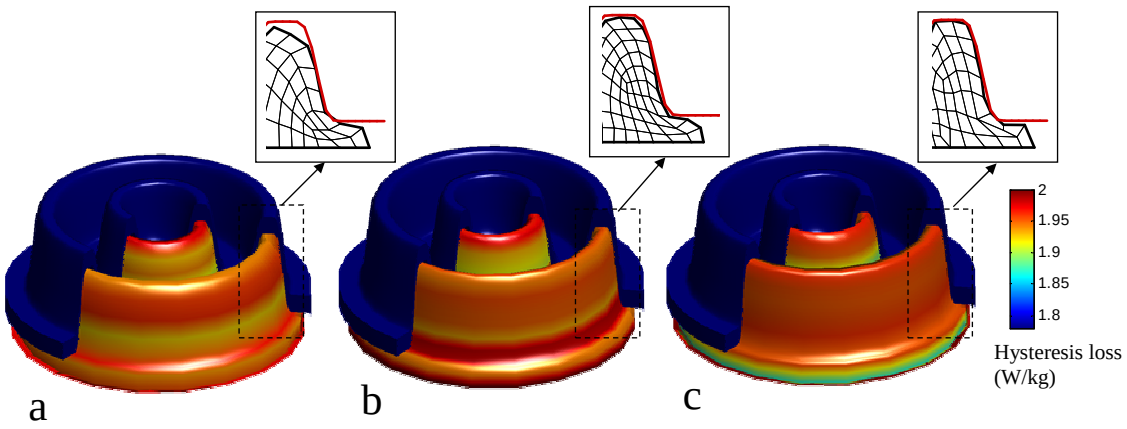

Figure 6.18: Hysteresis loss distribution and the die cavity fill is illustrated in the (a) first iteration (b) second iteration (c) final iteration

compression along y- direction in the z-y plane. The texture is predominated by the α fiber connecting the ideal Goss and brass orientations on the x- face of the ODF. At 0.44 mm stroke, z- axis tension texture becomes more predominant due to compressive strains developing along the x- direction as the preform progressively comes into contact with the die. This is evidenced by the loss of intensity in the z- axis $< 110 >$ fibers seen on the x- and y- faces of the ODF in Fig. 6.16(d). The $< 110 >$ pole figures at 0.22 mm stroke and 0.44 mm stroke respectively, as shown in Fig. 6.16(c) and (e), show the progressive loss of intensities of the z- axis $< 110 >$ fibers due to the change in the predominant deformation mode from y-axis plane strain compression to z- axis tension.

Advantages are derived from the symmetry of Rodrigues' space relative to the sample axes. The effect of a permutation of the sample axes on texture results in a corresponding permutation of the axes of Rodrigues space without any alteration of the structure of the texture. For example, textures developed under compression along the y-axis as seen in Fig. 6.10d were associated with increase in intensities along y- axis $< 110 >$ fibers located on the z- and x- faces of the ODF. In the

case of z- axis tension texture in Fig. 6.16(d), decrease in intensities are found (by corresponding permutation of axis) along z- axis $< 110 >$ fibers located on the x- and y- faces of the ODF. In contrast, over the Euler angle space, permutations of sample axes modify the texture in complex ways.

The optimal solution for the design problem is attained in 4 iterations. The preform shape identified at various iterations of the design problem and the objective function over 4 iterations are shown in Fig.6.17. The optimal preform shape corresponds to Bezier coefficients $\boldsymbol{\alpha} = \{1.0681, 1.0825, 1.1141,$
$1.1845, 1.2374, 1.2403\}$. The magnetic hysteresis loss distribution on the curved surface at the end of forging at the first, second and final iteration are shown in Fig.6.18(a-c) respectively. In the first iteration, less material was used leading to large underfill. In the second iteration, the underfill reduces drastically, however, the magnetic hysteresis losses have not yet reached the optimal value. The final iteration gives the optimal decrease in magnetic hysteresis loss as well as allows complete filling of the die cavity as indicated in Fig.6.18(c).

6.9 Conclusions

With multi-length scale modeling advances in predicting behavior of materials, it is increasingly becoming possible to devise methodologies to control metallic polycrystalline microstructures and generate products with tailored property distributions. Using a multi-scale sensitivity analysis technique, control of properties during deformation processes has been demonstrated. In this approach, sensitivity of microstructure field variables such as slip resistances and crystal orientation changes due to perturbations in process parameters such as forging rates, die and

perform shapes are exactly defined by direct differentiation of governing equations. These sensitivities are used within a gradient optimization framework for computational design of forming processes. Effectiveness of the developed finite element analysis and design techniques has been demonstrated using a numerical examples involving control of Young's Modulus and Yield strength variability in finished products. The algorithm is computationally efficient and is found to converge to the desired response within a few iterations. The simulator can be easily extended towards computational design of other orientation-dependent properties such as thermal conductivity or the thermal expansion coefficient as well as in the design of devices with desired optical properties.

Chapter 7

Suggestions for future research

In spite of this increased use of computer and information technologies in the analysis of deformation processes, selection of actual process design variables to optimize property distribution in materials still requires a significant amount of expert knowledge. To overcome this dependency and to create products with optimal properties, optimization-based design techniques for deformation processing are integrated with microstructure analysis in this work. The methodology described here would enable expansion of the conventional design space (with macroscopic objectives such as product yield maximization) to include objectives such as to obtain desired microstructure-sensitive properties in the final product.

The coupled macro-micro framework for multi-scale design provides a virtual environment where the macro- process parameters and processing sequence in cold-working processes can be altered to tune microstructure-sensitive material properties. The design problem of interest, such as to optimize engineering properties such as stiffness and yield strength through control of process parameters like die shapes and forging velocities, has several industrially relevant applications. Our approach can also be extended towards the control of a variety of properties (e.g. control of magnetic properties or material anisotropy [60]) that are dependent on the microstructure.

There are various elements in the task of extending this work, and can be broadly categorized into three areas: improvement in modeling physics of microstructure, modelling properties that depend on higher order microstructural features and extension towards other processing techniques. These future research

directions are listed below.

7.1 Optimization of Titanium alloy microstructure

Titanium alloys provide elevated specific strength, corrosion resistance, creep resistance, high temperature strength and fatigue strength. These properties are useful in a spectrum of applications including high-performance engines, armor and structural materials. Recent developments in computerized metallography have allowed unbiased and repeatable characterization of microstructural features of HCP Titanium alloys [94, 17, 95, 96, 97, 98, 99]. Microstructural features are statistical in nature prompting new work in stochastic modelling of microstructural features [100]. Studies have found strong correlation of many of the microstructural features of Titanium with properties such as strength and creep performance [96, 101, 102, 103, 104, 105]. Titanium is characterized by highly anisotropic mechanical behavior due to texture and wide variety of deformation mechanisms [106, 107, 108, 109]. Recently, three distinct stages of strain hardening have been documented [110, 111] in $\alpha-$Titanium and correlated to twin activity involving mechanisms such as slip-twin and twin-twin interactions and twin saturation. Rigorous quantitative numerical models of Titanium behavior at the meso-scale have only recently been developed using experimental insights [111]. Incorporation of these models in the simulation tools presented in this thesis is expected to yield significant improvements in controlling properties of commercially important components such as turbine blades and protective armors. Apart from texture, properties of metallic materials are affected by several characteristics that are stereological (grain sizes, shapes, grain boundary networks) attributes. The extension towards computing the effect of higher order features on properties is

discussed next.

7.2 Higher order microstructural features

In metallic materials, correlations exist between the nature of grain boundary distribution and defect-sensitive properties such as inter-granular corrosion [21], grain boundary segregation [20], stress corrosion cracking [22], and creep [23]. Properties such as elastic stiffness, thermal conductivity, and initial yield-strength are also affected by higher-order correlations of crystal orientations [24]. Inelastic deformation also originates from intergranular deformation modes such as grain boundary sliding. Grain boundary sliding has been found to occur in Aluminum alloys at stress concentrations and crack tips causing stress relaxation. Grain boundary modeling techniques can be used to model brittle fracture behavior of aluminum alloys. In recent years, cohesive interface models have been widely used to numerically simulate fracture initiation and growth by the finite element method either as mixed boundary conditions [112, 113, 114, 115] or by embedding into cohesive finite elements [116, 117, 118, 119]. Grain boundary physics could be incorporated into the microstructure interrogation model using cohesive elements to model the grain boundary or using appropriately modified constitutive laws [120] that account for grain size effects. For inversion of relationship of higher-order features with computed properties, one could develop methods based on modern methods of statistical learning. These techniques are being successfully employed in other fields such as bio-informatics and macro-molecule and genome mapping [121]-[126] and are especially useful for addressing microstructure-property inversion problems. Another interesting problem that can be addressed is the development of methodologies to visualize high-dimensional microstructure-property-process maps

graphically in three dimensions using model reduction of higher order microstructural features.

7.3 Control of thermal processing stages

Thermal processing involves recrystallization of deformed grains with dislocation-free grains. A stored energy is introduced through an accumulation of dislocations during deformation in the homogenization model. This involves modeling for strain energy development and nucleation probabilities based on grain boundary (GB) energy [127, 128, 129, 130]. GB nucleation is modelled by considering all orientations in the deformation texture as nuclei and distributing them in the deformed matrix depending on the stored energy [131]. All kinds of deformation inhomogeneities are considered to be favoured sites for nucleation. The most prominent are grains with large in-grain misorientations and transition bands [132] within grains identified from the finite element model. Recovery kinetics of a deformed grain is determined by the number of different activated slip systems during deformation [133] with several different activated slip systems leading to faster recovery. For modeling recrystallization textures, boundary mobilities of nuclei are assumed to be given by a mean-field approximation where the rate of growth is proportional to the variation in strain energy from the mean field energy. The driving force for primary static recrystallization results from the difference between the stored energy densities of the deformed matrix and the nucleus obtained from finite element simulations. Monte-Carlo (MC) method [134, 135, 136, 137, 138] can be used to simulate aspects of grain growth kinetics. Information on residual stresses and plastic work in the microstructure are transferred from the finite element model to the Monte Carlo analysis. Although methods such as these are only approximate

due to randomness in the process and the level of assumptions involved (e.g. in nucleation locations), well-calibrated parameters [139] have indeed shown reasonable comparisons with experimental results, prompting their potential use for designing thermal stages during the manufacturing process.

BIBLIOGRAPHY

[1] M.F. Ashby, Materials Selection in Mechanical Design (Pergamon, Tarrytown, NY, 1992).

[2] G.B. Olson, Computational Design of Hierarchically Structured Materials, Science, 277(5330) (1997) 1237-1242.

[3] O. Sigmund, S. Torquato, Composites with extremal thermal expansion coefficients, Appl. Phys. Lett., 69 (1996) 3203–3205.

[4] R. Lakes, Deformations in Extreme Matter. Science, 288(5473) (2000) 1976-1977.

[5] A.D. Rollett, M.L. Storch, E.J. Hilsinki, S.R. Goodman, Approach to saturation in textured soft magnetic materials. Metallurgical and Materials Transactions A, 32 (2001) 2595–2603.

[6] W.F. Hosford, 1993. The mechanics of crystals and textured polycrystals. New York:Oxford University Press.

[7] J.S. Chung, S.M. Hwang, Application of a genetic algorithm to the optimal design of the die shape in extrusion, Journal of Materials Processing Technology, 72 (1997) 69–77.

[8] D. Ko, D. Kim, B. Kim, Application of artificial neural network and Taguchi method to preform design in metal forming considering workability, International Journal of Machine Tools and Manufacture, 39 (1999) 771–785.

[9] J. L. Chenot, E. Massoni, L. Fourment, Inverse problems in finite element simulation of metal forming processes, Engineering Computations, 13 (1996) 190– 225.

[10] L.C. Sousa, C.F. Castro, C.A.C. Antonio, A.D. Santos, Inverse methods in design of industrial forging processes, Journal of Materials Processing Technology, 128 (2002) 266-273.

[11] L. Fourment, J.L. Chenot, Inverse methods applied to metal forming processes, Computational Mechanics for the Twenty-First Century; Saxe-Coburg Publications, Edinburgh, UK, (2000) 127–144.

[12] A. Srikanth, N. Zabaras, Shape optimization and preform design in metal forming processes, Computer Methods in Applied Mechanics Engrg, 190 (2000) 1859–1901.

[13] A. Srikanth, N. Zabaras, An updated Lagrangian finite element sensitivity analysis of large deformations using quadrilateral elements, International Journal for Numerical Methods in Engineering, 52 (2001) 1131–1163.

[14] L. Fourment, T. Balan, J.L. Chenot, Optimal design for non-steady-state metal forming processes II. Application of shape optimization in forging, International Journal for Numerical Methods in Engineering, 39 (1996) 51–65.

[15] Z.Y. Gao, R.V. Grandhi, Sensitivity analysis and shape optimization for preform design in thermo-mechanical coupled analysis, International Journal for Numerical Methods in Engineering, 45 (1999) 1349 –1373.

[16] S. Acharjee, N. Zabaras, The continuum sensitivity method for the computational design of three-dimensional deformation processes, Computer Methods in Applied Mechanics and Engineering, 195 (2006) 6822–6842.

[17] V. Seetharaman, S.L. Semiatin, Microstructures and tensile properties of Ti–45.5Al–2Nb–2Cr rolled sheets, Materials Science and Engineering A, 299 (2001) 195–209.

[18] W.J. Evans, Optimising mechanical properties in alpha-beta titanium alloys, Materials Science and Engineering A, 243 (1998) 89–96.

[19] Y.V.R.K. Prasad, T. Seshacharyulu, Processing maps for hot working of titanium alloys, Materials Science and Engineering A, 243 (1998) 82–88.

[20] T. Watanabe, T. Murakami, S. Karashima, Misorientation dependence of grain boundary segregation. Scripta Metall., 12 (1978) 361-365.

[21] P. Lin, G. Palumbo, U. Erb, K.T. Aust,Influence of grain boundary character distribution on sensitization and intergranular corrosion of alloy 600. Scripta Metall. Mater., 33 (1995) 1387-1392.

[22] Y. Pan, B.L. Adams, T. Olson, N. Panayotou, Grain boundary structure effects on intergranular stress corrosion cracking of alloy X-750, Acta Mater., 44 (1996) 4685-4695.

[23] G.S. Was, V. Thaveeprungsriporn, D.C. Crawford, Grain boundary misorientation effects on creep and cracking in Ni-based alloys, J. Metals, 50 (1998) 44-49.

[24] M.J. Beran, T.A. Mason, B.L. Adams, T. Olson, Bounding elastic constants of an orthotropic polycrystal from measurements of the microstructure, J. Mech. Phys. Solids, 44 (1996) 1543–1563.

[25] H.J. Bunge, Texture Analysis in materials science, Butterworths, 1982.

[26] A. Heinz, P. Neumann, Representation of orientation and disorientation data for cubic, hexagonal, tetragonal and orthorhombic crystals, Acta Cryst., A47 (1991) 780–789.

[27] U.F. Kocks, C.N. Tomé, H.R. Wenk, Texture and anisotropy - Preferred orientations in polycrystals and their effect on materials properties. Cambridge: Cambridge University Press,2000.

[28] B.L. Adams, A. Henrie, B. Henrie, M. Lyon, S.R. Kalidindi, H. Garmestani, Microstructure-sensitive design of a compliant beam, J. Mech. and Physics of Solids, 49(8) (2001) 1639–1663.

[29] S.R. Kalidindi, J.R. Houskamp, M. Lyons, B.L. Adams, Microstructure sensitive design of an orthotropic plate subjected to tensile load, International Journal of Plasticity, 20(8-9) (2004) 1561-1575.

[30] A. Kumar, P.R. Dawson, Computational modeling of F.C.C. deformation textures over Rodrigues' space, Acta Materialia, 48 (2000) 2719-2736.

[31] A. Kumar, P.R. Dawson, Modeling crystallographic texture evolution with finite elements over neo-Eulerian orientation spaces, Computer Methods in Applied Mechanics and Engineering, 153(3-4) (1998) 259-302.

[32] S. Nemat-Nasser, M. Hori, 1993. Micromechanics: Overall Properties of Heterogeneous Solids. Elsevier, Amsterdam.

[33] R. Hill, The elastic behavior of a crystalline aggregate. Proc. Phys. Soc. London A, 65 (1952) 349–354.

[34] R. Hill, Continuum micro-mechanics of elastoplastic polycrystals. J. Mech. Phys. Solids, 13 (1965) 89–101.

[35] S. Nemat-Nasser, 1999. Averaging theorems in finite deformation plasticity. Mechanics of Materials, 31 (1999) 493–523.

[36] R. Hill, On constitutive macro-variables for heterogeneous solids at finite strain. Proc. Roy. Soc. London, 326A (1972) 131–147.

[37] R. Hill, On macroscopic effects of heterogeneity in elastoplastic media at finite strain, Math. Proc. Camb. Phil. Soc., 95 (1984) 481–494.

[38] K.S. Havner, Finite Plastic Deformation of Crystalline Solids, Cambridge Monographs on Mechanics and Applied Mathematics, Cambridge University Press, Cambridge (1992).

[39] P. Ponte Castañeda, Bounds and estimates for the properties of nonlinear heterogeneous systems, Philosophical Transactions of the Royal Society of London. Series A. Physical Sciences and Engineering, 340 (1992) 531–567.

[40] P. Ponte Castañeda, New variational principles in plasticity and their application to composite materials, Journal of the Mechanics and Physics of Solids, 40(8) (1992) 1757–1788.

[41] P. Ponte Castañeda, M. V. Nebozhyn, Variational estimates of the self-consistent type for the effective behaviour of some model nonlinear polycrystals, Proceedings of the Royal Society. London. Series A. Mathematical, Physical and Engineering Sciences, 453 (1997) 2715–2724.

[42] H. Garmestani, S. Lin, B. L. Adams, S. Ahzi, Statistical continuum theory for large plastic deformation of polycrystalline materials, Journal of the Mechanics and Physics of Solids, 49(3) (2001) 589–607.

[43] H. Garmestani, S. Lin, B. L. Adams, Statistical continuum theory for inelastic behavior of a two-phase medium, International Journal of Plasticity, 14(8) (1998) 719–731.

[44] S. Lin, H. Garmestani, Statistical continuum mechanics analysis of an elastic two-isotropic-phase composite material, Composites, Part B: Engineering 31(1) (2000) 39–46.

[45] S. Lin, H. Garmestani, B. Adams, The evolution of probability functions in an inelasticly deforming two-phase medium, International Journal of Solids and Structures, 37(3) (2000) 423–434.

[46] S.V. Harren, R.J. Asaro, Nonuniform deformations in polycrystals and aspects of the validity of the Taylor model, Journal of the Mechanics and Physics of Solids, 37 (1989) 191–232.

[47] C.A. Bronkhorst, S.R. Kalidindi, L. Anand, Polycrystalline plasticity and the evolution of crystallographic texture in fcc metals, Philosophical Transactions of the Royal Society of London, A341 (1992) 443–477.

[48] R. Becker, S. Panchanadeeswaran, Effects of grain interactions on deformation and local texture in polycrystals, Acta Metallurgica et Materialia, 43 (1995) 2701–2719.

[49] A.J. Beaudoin, H. Mecking, U.F. Kocks, Development of localized orientation gradients in fcc polycrystals, Philosophical Magazine A, 73 (1996) 1503–1518.

[50] D.P. Mika, P.R. Dawson, Polycrystal plasticity modeling of intracrystalline boundary textures, Acta Materialia, 47 (1999) 1355–1369.

[51] G.B. Sarma, B. Radhakrishnan, P.R. Dawson, Mesoscale modeling of microstructure and texture evolution during deformation processing of metals, Advances in Engineering Materials, 4 (2002) 509–514.

[52] K. Matous, A.M. Maniatty, Finite element formulation for modelling large deformations in elasto-viscoplastic polycrystals, International Journal For Numerical Methods In Engineering, 60 (2004) 2313–2333.

[53] C. Miehe, J. Schröder, J. Schotte, Computational homogenization analysis in finite plasticity Simulation of texture development in polycrystalline materials, Computer Methods in Applied Mechanics and Engineering, 171 (1999) 87–418.

[54] S. Balasubramanian, L. Anand, Elasto-viscoplastic constitutive equations for polycrystalline fcc materials at low homologous temperatures, Journal of the Mechanics and Physics of Solids, 50 (2002) 101–126.

[55] N. Zabaras, S. Ganapathysubramanian, Q. Li, A continuum sensitivity method for the design of multi-stage metal forming processes, International Journal of Mechanical Sciences, 45 (2003) 325–358.

[56] S. Ganapathysubramanian, N. Zabaras, Modeling the thermoelastic-viscoplastic response of polycrystals using a continuum representation over the orientation space, Int J Plasticity, Int J Plasticity, 21/1 (2005) 119–144.

[57] L. Anand, M. Kothari, A computational procedure for rate-independent crystal plasticity, Journal of the Mechanics and Physics of Solids, 44(4) (1996) 525–558.

[58] B.L. Adams, M. Lyon, B. Henrie, Microstructures by design: linear problems in elastic-plastic design, International Journal of Plasticity, 20 (8-9) (2004) 1577–1602.

[59] V. Sundararaghavan, N. Zabaras, Linear analysis of texture-property relationships using process-based representations of Rodrigues space, Acta Materialia, 55(5) (2007) 1573-1587.

[60] S. Acharjee, N. Zabaras, A proper orthogonal decomposition approach to microstructure model reduction in Rodrigues space with applications to the control of material properties, Acta Materialia, 51/18 (2003) 5627–5646.

[61] S. Ganapathysubramanian, N. Zabaras, Design across length scales: A reduced-order model of polycrystal plasticity for the control of microstructure-sensitive material properties, Computer Methods in Applied Mechanics and Engineering, 193 (45-47) (2004) 5017–5034.

[62] V. Sundararaghavan, N. Zabaras, On the synergy between classification of textures and deformation process sequence selection, Acta Materialia, 53/4 (2004) 1015–1027.

[63] S. Acharjee, N. Zabaras, The continuum sensitivity method for the computational design of three-dimensional deformation processes, Computer Methods in Applied Mechanics and Engineering, 195 (2006) 6822-6842,

[64] D.S. Li, H. Garmestani, S. Ahzi, Processing path optimization to achieve desired texture in polycrystalline materials, Acta Materialia, 55(2) (2007) 647-654.

[65] S.S. Ravindran, Control of flow separation over a forward-facing step by model reduction, Computer Methods in Applied Mechanics and Engineering, 191(41-42) (2002) 4599-4617

[66] N.R. Barton, D.E. Boyce, P.R. Dawson, Pole figure inversion using finite elements over Rodrigues space. Textures and Microstructures, 35(2) (2002) 113-144.

[67] S.S. Ravindran, Adaptive reduced order controllers for a thermal flow system

using proper orthogonal decomposition, SIAM J Sci Comput., 23(6) (2002) 1924–1942.

[68] Titanium Metals corporation (www.timet.com).

[69] H.R. Wenk, Preferred orientation in deformed metals and rocks: An introduction to modern texture analysis. London:Academic Press Inc. (1985).

[70] G. Proust, S.R. Kalidindi, Procedures for construction of anisotropic elastic plastic property closures for face-centered cubic polycrystals using first-order bounding relations, Journal of the Mechanics and Physics of Solids, 54(8) (2006) 1744–1762.

[71] D.G. Luenberger, Linear and Nonlinear Programming, Second Edition, Kluwer Academic Publishers, Norwell, Massachussetts, USA (2003).

[72] K. Ito, S.S. Ravindran, A Reduced-Order Method for Simulation and Control of Fluid Flows, Journal of Computational Physics, 143(2) (1998) 403-425.

[73] M.L. Joyner, A numerical study of the POD method in NDE Applied Mathematics and Computation, 174 (2006) 732-754

[74] M. Lyon, B.L. Adams, Gradient-based non-linear microstructure design, Journal of the Mechanics and Physics of Solids, 52(11) (2004) 2569-2586.

[75] B.L. Adams, X.C. Gao, S.R. Kalidindi, Finite approximations to the second-order properties closure in single phase polycrystals, Acta Materialia, 53(13) (2005) 3563-3577.

[76] V. Sundararaghavan, N. Zabaras, Design of microstructure-sensitive properties in elasto-viscoplastic polycrystals using multi-scale homogenization, International Journal of Plasticity, 22 (2006) 1799-1824.

[77] P.R. Dawson, E.B. Marin, Computational mechanics for metal deformation processes using polycrystal plasticity, Adv. Appl. Mech., 34 (1997) 77-169.

[78] V. Sundararaghavan, N. Zabaras, A dynamic material library for the representation of single phase polyhedral microstructures, Acta Materialia, 52/14 (2004) 4111-4119.

[79] D. Pelleg, A. Moore, X-means: Extending K-means with Efficient Estimation

of the Number of Clusters, Seventeenth International Conference on Machine Learning, Stanford University, 2000.

[80] A. Gurson, Continuum theory of ductile rupture by void nucleation and growth: Part I: Yield criteria and flow rules for porous ductile media, J. Engrg. Mater. Technol., 99 (1977) 2-15.

[81] M.E. Gurtin, An Introduction to Continuum Mechanics, Volume 158 of Mathematics in Science and Engineering, Academic Press (1981).

[82] M. Kothari, L. Anand, Elasto-viscoplastic constitutive equations for polycrystalline metals: application to tantalum, J. Mech. Phys. Solids, 46 (1998) 51–83.

[83] OOF-2, Object oriented finite element analysis of real material microstructures, NIST Public domain software available at http://www.ctcms.nist.gov/oof/oof2.html.

[84] O. van der Sluis, P.J.G. Schreurs, W.A.M. Brekelmans, H.E.H. Meijer, Overall behaviour of heterogeneous elasto-viscoplastic materials: effect of microstructural modeling, Mechanics of Materials, 32 (2000) 449–462.

[85] V. Kouznetsova, W.A.M. Brekelmans, F.P.T. Baaijens, An approach to micro-macro modeling of heterogeneous materials. Comput. Mech. 27 (2001) 37-48.

[86] S. Badrinarayanan, A. Constantinescou, N. Zabaras, Preform design in metal forming, In: S. F. Shen and P. R. Dawson, editors, Numerical Methods in Industrial Forming Processes, 533–538, Rotterdam (1995).

[87] S. Badrinarayanan, N. Zabaras, A sensitivity analysis for the optimal design of metal forming processes, Computer Methods in Applied Mechanics and Engineering, 129 (1996) 319–348.

[88] S. Ganapathysubramanian. Computational design of deformation processes for the control of microstructure-sensitive properties, Ph.D. Dissertation, Cornell University (2004).

[89] S. Ganapathysubramanian, N. Zabaras, A continuum sensitivity method for finite thermo-inelastic deformations with applications to the design of hot forming processes, International Journal for Numerical Methods in Engineering, 55 (2002) 1391–1437.

[90] V. Sundararaghavan, N. Zabaras, A multi-length scale continuum sensitivity analysis for the control of texture-dependent properties in deformation processing, International Journal of Plasticity, in preparation, (2007).

[91] A. Kumar, P.R. Dawson, The simulation of texture evolution with finite elements over orientation space I & II. Computer Methods in Applied Mechanics and Engineering, 130 (1996) 227–261.

[92] E.H. Lee, Elastic-plastic deformation at finite strains. Journal of Applied Mechanics, 26 (1969 1–6.

[93] R. Carreker, W. Hibbard, Tensile deformation of aluminum as a function of temperature, strain rate and grain size, Trans. AIME, 209 (1957) 1157–1163.

[94] F. Warchomicka, M. Stockinger, H.P. Degischer, Quantitative analysis of the microstructure of near beta titanium alloy during compression tests, Journal of Materials Processing Technology, 177 (2006) 473–477.

[95] T.H. Yu, C.H. Koo, Microstructural evolution of a hot-rolled Ti–40Al–10Nb alloy, Materials Science and Engineering A, 239-240 (1997) 694–701.

[96] J. Tiley, T. Searles, E. Lee, S. Kar, R. Banerjee, J.C. Russ, H.L. Fraser, Quantification of microstructural features in α/β titanium alloys, Materials Science and Engineering A, 372 (2004) 191–198.

[97] M.G. Glavicic, J.D. Miller, S.L. Semiatin, A method to measure the texture of secondary alpha in bimodal titanium-alloy microstructures, Scripta Materialia, 54 (2006) 281–286.

[98] J. Chraponski, W. Szkliniarz, Quantitative metallography of two-phase titanium alloys, Materials Characterization, 46 (2001) 149–154.

[99] D. Bhattacharyya, G.B. Viswanathan, Robb Denkenberger, D. Furrer, H. L. Fraser, The role of crystallographic and geometrical relationships between alpha and beta phases in an alpha beta titanium alloy, Acta Materialia, 51 (2003) 4679–4691.

[100] N. Zabaras, V. Sundararaghavan, S. Sankaran, An information theoretic approach for obtaining property PDFs from macro specifications of microstructural uncertainty, TMS letters, 3 (2006) 1–3.

[101] L. Miaoquan, X. Aiming, H. Weichao, W. Hairong, S. Shaobo, S. Lichuang,

Microstructural evolution and modelling of the hot compression of a TC6 titanium alloy, Materials Characterization, 49 (2002) 203–209.

[102] I. Weiss, S.L. Semiatin, Thermomechanical processing of alpha titanium alloys–an overview, Materials Science and Engineering, A263 (1999) 243–256.

[103] S. Malinov, W. Sha, Application of artificial neural networks for modelling correlations in titanium alloys, Materials Science and Engineering, A365 (2004) 202–211.

[104] S. Ankem, C.A. Greene, Recent developments in microstructure property relationships of beta titanium alloys, Materials Science and Engineering A, 263 (1999) 127–131.

[105] R. Filip, K. Kubiak, W. Ziaja, J. Sieniawski, The effect of microstructure on the mechanical properties of two-phase titanium alloys, Journal of Materials Processing Technology, 133 (2003) 84–89.

[106] J.W. Christian and S. Mahajan. Deformation twinning, Prog. Mater. Sci., 39 (1995) 1-20.

[107] E.O. Hall. Twinning, Butterworths, London (1954).

[108] N.V. Klasen-Neklyudova. Mechanical Twinning of Crystals, Plenum Press, New York (1964).

[109] R.E. Reed-Hill, J.P. Hirth and H.C. Rogers, Editors, Deformation Twinning, Gordon and Breach, New York (1964).

[110] A.A. Salem, S.R. Kalidindi, R.D. Doherty, Strain hardening regimes and microstructure evolution during large strain compression of high purity titanium, Scripta Materialia, 46 (2002) 419–423.

[111] A.A. Salem, S.R. Kalidindi, S.L. Semiatin, Strain hardening due to deformation twinning in a-titanium: Constitutive relations and crystal-plasticity modeling, Acta Materialia, 53 (2005) 3495–3502.

[112] A. Needleman, An analysis of tensile decohesion along an interface, Journal of the Mechanics and Physics of Solids, 38 (1990) 289–324.

[113] A. Needleman, Micromechanical modeling of interfacial decohesion, Ultramicroscopy, 40 (1992) 203–214.

[114] V. Tvergaard, J.W. Hutchinson, The influence of plasticity on mixed-mode interface toughness, Journal of the Mechanics and Physics of Solids, 41 (1993) 1119–1135.

[115] V. Tvergaard, J.W. Hutchinson, Effect of strain dependent cohesive zone model on predictions of crack growth resistance, International Journal of Solids and Structures, 33 (1996) 3297–3308.

[116] K. Willam, Simulation issues of distributed and localized failure computations, In: Mazars, J. and Bazant, Z.P. Editors, 1989. Cracking and Damage Elsevier, New York, (1989) 363–378.

[117] G.T.Camacho, M. Ortiz, Adaptive Lagrangian modelling of ballistic penetration of metallic targets, Computer Methods in Applied Mechanics and Engineering, 142 (1997) 269–301.

[118] X.P. Xu, A. Needleman, Numerical simulations of fast crack growth in brittle solids, Journal of the Mechanics and Physics of Solids, 42 (1994) 1397–1434.

[119] M. Ortiz, A. Pandolfi, A class of cohesive elements for the simulation of three-dimensional crack propagation, International Journal for Numerical Methods in Engineering, 44 (1999) 1267–1282.

[120] A. Acharya, A.J. Beaudoin, Grain-size effect in FCC viscoplastic polycrystals at moderate strains, Journal of the Mechanics and Physics of Solids, 48 (2000) 2213–2230.

[121] F.C. Bernstein, T.F. Koetzle, G.J.B. Williams, E.F. Meyer Jr, M.D. Brice, J.R. Rodgers, O. Kennard, T. Shimanouchi, M. Tasumi, The Protein Data Bank: A computer-based archival file for macromolecular structures, European Journal of Biochemistry, 80 (1977) 319–324.

[122] J. Mellor, I. Yanai, K.H. Clodfelter, J. Mintseris, C. DeLisi, Predictome: a database of putative functional links between proteins, Nucleic Acids Res, 30(1) (2002) 306–309.

[123] C. H. Wu, S. Zhao, H.L. Chen, A protein class database organized with prosite protein groups and PIR superfamilies, Journal of Computational Biology, 3 (1996) 547–561.

[124] L. F. Kolakowski, GCRDb: A G-protein-coupled receptor database, Receptors Channels, 2 (1994) 1–7.

[125] T. K. Attwood, M. E. Beck, A. J. Bleasy, D. J. Parry- Smith, PRINTS:A database of protein motif fingerprints, Nucleic Acids Research, 22 (17) (1994) 3590–3596.

[126] S. Curtarolo, D. Morgan, K. Persson, J. Rodgers, G. Ceder, Predicting crystal structures with data mining of quantum calculations, Physics Review Letters, 91 (13) (2003) 135503:1–4.

[127] H.R. Wenk, G. Canova, Y. Brechet, L. Flandin, A deformation based model for recrystallization of anisotropic materials, Acta Mater, 45(8) (1997) 3283–3296.

[128] A.J. Beaudoin, R. Srinivasan, S.L. Semiatin, Microstructure modeling and prediction during thermomechanical processing, JOM, 54 (2002) 25–29.

[129] A.D. Rollett, Overview of modeling and simulation of recrystallization, Prog. Mater. Sci., 42 (1997) 79–99.

[130] A. Hildenbrand, L.S. Toth, A. Molinari, J. Baczynski, J.J. Jonas, Self-consistent polycrystal modeling of dynamic recrystallization during shear deformation of Ti IF steel, Acta Mater., 47 (1999) 447–460.

[131] I.L. Dillamore, H. Katoh, Mechanisms of recrystallization in cubic metals with particular reference to their orientation dependence, Metal Sci., 8 (1974) 73–83.

[132] O. Engler, Recrystallisation textures in copper-manganese alloys, Acta Mater., 49 (2001) 1237-1247.

[133] M. Seefeldt, L. Delannay, B. Peeters, E. Aernoudt, P. Van Houtte, Modelling the initial stage of grain subdivision with the help of a coupled substructure and texture evolution algorithm, Acta Mater., 49 (2001) 2129-2143.

[134] V. Sundararaghavan, N. Zabaras, Classification of three-dimensional microstructures using support vector machines, Computational Materials Science, 32 (2005) 223–239.

[135] A. D. Rollett, D. J. Srolovitz, M. P. Anderson, Simulation and theory of

abnormal grain growth - anisotropic grain boundary energies and mobilities, Acta Metall., 37(4) (1989) 1227–1240.

[136] D. J. Srolovitz, G. S. Crest, M. P. Anderson, Computer simulation of recrystallization-I. Homogeneous nucleation and growth, Acta Metall., 34 (1986) 1833–1845.

[137] B. Radhakrishnan, G. B. Sarma, T. Zacharia, Modeling the kinetics and microstructural evolution during static recrystallization - Monte carlo simulation of recrystallization, Comp. Mater. Sc., 46 (1998) 4415–4433.

[138] A. D. Rollett, M. J. Lutton, D. J. Srolovitz, Microstructural simulation of dynamic recrystallization, Acta Metall., 40 (1992) 43–55.

[139] M. Crumbach, M. Goerdeler, G. Gottstein, L. Neumann, H. Aretz, R. Kopp, Through-process texture modelling of aluminium alloys, Modelling Simul. Mater. Sci. Eng., 12 (2004) S1-S18.